

Fabrication of Robust Superhydrophobic Aluminium Alloys and Their Application in Corrosion Protection

by

Ahmad Esmaeilirad

B.SC., Sharif University of Technology, 2008

M.SC., Sharif University of Technology, 2011

A Dissertation Submitted in Partial Fulfillment of the
Requirements for the Degree of

DOCTOR OF PHILOSOPHY

in the Department of Mechanical Engineering

© Ahmad Esmaeilirad, 2017
University of Victoria

All rights reserved. This dissertation may not be reproduced in whole or in part, by photocopying or other means, without the permission of the author.

Supervisory Committee

Fabrication of Robust Superhydrophobic Aluminium Alloys and Their Application in Corrosion Protection

by

Ahmad Esmaeilirad

B.SC., Sharif University of Technology, 2008

M.SC., Sharif University of Technology, 2011

Supervisory Committee

Dr. Martin B.G. Jun, Co-Supervisor
(Department of Mechanical Engineering)

Dr. ir. Frank C.J.M. van Veggel, Co-Supervisor
(Department of Chemistry)

Dr. R.B. Bhiladvala, Departmental Member
(Department of Mechanical Engineering)

Dr. Harry H. L. Kwok, Outside Member
(Department of Electrical and Computer Engineering)

Abstract

Supervisory Committee

Dr. Martin B.G. Jun, Co-Supervisor
(Department of Mechanical Engineering)

Dr. ir. Frank C.J.M. van Veggel, Co-Supervisor
(Department of Chemistry)

Dr. R.B. Bhiladvala, Departmental Member
(Department of Mechanical Engineering)

Dr. Harry H. L. Kwok, Outside Member
(Department of Electrical and Computer Engineering)

Superhydrophobic coatings attract significant attention regarding a variety of applications, such as in friction drag reduction, anti-contamination surfaces, and recently metals corrosion protection. Superhydrophobic surfaces are known to protect metals and their alloys from natural degradation by limiting water access and its surface interaction. Non-wetting properties of superhydrophobic surfaces are attributed to their low-surface energy, in combination with their surface microtexture. Several approaches based on tailoring a microtextured surface followed by surface modification with a low-surface-energy material have been employed for developing non-wetting metallic surfaces. However, developing a durable superhydrophobic coating, in terms of mechanical abrasion, thermal and chemical stability, which could serve in harsh environments, is still an outstanding challenge.

In this research work two different approaches have been employed to create durable superhydrophobic aluminium alloy surfaces. In the first approach a practical and cost-effective method, which is based on direct surface acid/base etching is used to promote desired rough microstructure on aluminium alloy. Then, a facile surface modification with chlorosilanes as a low-surface-energy compound is utilized to generate surface superhydrophobicity. The superhydrophobic aluminium alloy has a water contact angle of about $165 \pm 2^\circ$ and rolling angle of less than $3 \pm 0.2^\circ$. The developed superhydrophobic aluminium alloy surfaces shows remarkable thermal stability up to 375°C for 20 min.

In the second approach, a controlled hydrothermal deposition process is utilized to develop cerium oxide based coatings with well-defined microtextured surface on aluminium alloy substrates. The superhydrophobicity of the cerium oxide coatings is acquired by further treatment with trichloro(octyl)silane surface. The impacts of various hydrothermal processing conditions on surface microstructure of coatings, wettability, and ultimate corrosion protection have been also investigated. The fabricated cerium oxide based coating exhibit high level of water repellency with a water contact angle of about $170 \pm 2^\circ$ and rolling angle of about $2.4 \pm 0.2^\circ$. The superhydrophobic coatings show outstanding wear-resistance by maintaining their non-wetting properties after abrasion by #800 abrasive paper for 1.0 m under applied pressures up to 4 kPa pressure. The coatings also show remarkable chemical stability under acidic and alkaline condition and during immersion in corrosive 3.5 wt % NaCl solution for more than 2 days. They also provide excellent corrosion protection for T6-6061 aluminium alloy substrate by decreasing its corrosion rate for about three orders of magnitude.

Table of Contents

Supervisory Committee	ii
Abstract	iii
Table of Contents	v
List of Tables	vii
List of Figures	viii
List of Abbreviations and Symbols.....	xi
Acknowledgments.....	xii
Dedication	xiii
Chapter 1 Introduction	1
1.1 Research Motivation	1
1.2 Dissertation Outline	3
1.3 Research Contributions	4
Chapter 2 Literature review	6
2.1 Non-wetting surfaces, from nature to artificial.....	6
2.1.1 Introduction.....	6
2.1.2 Wettability (Theoretical Background)	7
2.1.3 Developing Artificial Superhydrophobic surfaces.....	10
2.2 Cerium Oxide.....	12
2.2.1 Introduction.....	12
2.2.2 CeO ₂ Applications	13
2.2.3 CeO ₂ synthesizing and Coating methods	14
2.2.4 CeO ₂ Wettability	16
2.3 Corrosion and Corrosion measurement	17
2.3.1 Introduction.....	17
2.3.2 Basics of metal corrosion electrochemistry	18
2.3.3 Corrosion rate measurement through Tafel extrapolation	21
Chapter 3 A Cost-effective Method to Create Physically and Thermally Stable and Storable Super-hydrophobic Aluminium Alloy Surfaces	24
3.1 Abstract	24
3.2 Introduction.....	25
3.3 Experimental Section	27
3.3.1 Materials	27
3.3.2 Aluminium Surfaces Roughening and Surface Modification Procedure.....	28
3.3.3 Characterization	30
3.4 Results and Discussion	31
3.4.1 Roughening Procedure of Aluminium Alloy Surfaces	31
3.4.2 Super-hydrophobic characterization	36
3.4.3 The physical and thermal stability and storability of Super-hydrophobic aluminium surfaces	40
3.5 Conclusions.....	45
3.6 Supporting Information.....	46
3.7 Acknowledgement	49

3.8	Graphical abstract	49
Chapter 4 Hydrothermal Deposition of Robust Cerium Oxide Based Superhydrophobic and Corrosion Resistive Coatings on Aluminium Alloy Substrates		
4.1	Abstract	50
4.2	Introduction	51
4.3	Experimental Section	55
4.3.1	Materials and method	55
4.3.2	Characterization	57
4.4	Results and Discussion	59
4.4.1	Chemical composition and surface chemistry	60
4.4.2	Wettability and surface morphology control of CeO ₂ coatings	67
4.4.3	Effect of substrate positioning	68
4.4.4	Effects of solution amount (hydrothermal processing pressure)	73
4.4.5	Effect of reaction temperature	77
4.4.6	Effect of hydrothermal heating rate	81
4.4.7	Mechanical durability and chemical stability of superhydrophobic coating	83
4.4.8	Corrosion protection	87
4.5	Conclusions	91
4.6	Supporting Information	92
4.6.1	Ag/AgCl reference electrode preparation	92
4.6.2	Crystallographic characterization	94
4.7	Author contributions	100
4.8	Acknowledgment	100
4.9	Graphical abstract	101
Chapter 5 Conclusions and Future Work		
5.1	Conclusions	102
5.2	Future Work	105
Chapter 6 Bibliography		
		106

List of Tables

Table 3.1. The roughening process, surface modifier, amount of modifier, roughness, WCA, and CAH of the specimens.	29
Table 3.2. The average WCA of (a) S71, (b) S73, and (c) S74 specimens after 1, 10, 20, 30, and 180 days of storing at ambient air.	44
Table 4.1. Hydrothermal processing conditions utilized for S1 to S10 coating deposition.	57
Table 4.2. The surface roughness (S_a), static water contact angle, and rolling angle of bare T6-6061 AA, TCOS modified T6-6061 AA, and S1 to S4 coatings grown on the bottom face of horizontally placed T6-6061 AA.	75
Table 4.3. The surface roughness (S_a), static water contact angle, and rolling angle of S2, S5, S6, S7, S8, and S9 coatings grown on the bottom face of horizontally placed T6-6061 AA.	79
Table 4.4. The surface roughness (S_a), static water contact angle, and rolling angle of S2, S9 and S10 coatings grown on the bottom face of horizontally placed T6-6061 AA.	82
Table 4.5. Corrosion potential (E_{corr}), corrosion current density (j_{corr}), and penetration (corrosion) rate of the T6-6061 AA substrate before and after various surface coating and treatment.	90

List of Figures

Figure 2.1. Schematic of a droplet (a) on hydrophobic surface (contact angle $\theta > 90^\circ$), (b) on hydrophilic surface (contact angle $\theta < 90^\circ$), and (c) advancing (α) and residing contact angle (r) on tilting surface.....	7
Figure 2.2. Schematic of interaction between a droplet and (a) a smooth substrate (Young's model), (b) a rough substrate regarding Wenzel model, and (c) a rough substrate regarding Cassie & Baxter model.....	10
Figure 2.3. (a) A schematic of metal corrosion in acidic solution. (b) A schematic of a system, which the potential difference between a metal and a reference electrode is measured.	20
Figure 2.4. A schematic of a three-electrode potentiodynamic electrochemical corrosion testing system.....	22
Figure 2.5. Schematic of a typical Tafel plot in which E_{corr} and I_{corr} correspond to corrosion potential and corrosion current, respectively.	23
Figure 3.1. SEM images of the aluminium alloy surfaces etched for (a) 5 min and (b) 7 min in acid solution with volume ratio of $V_{H2O} : V_{HCl} : V_{CH3COOH} = 20 : 8 : 1$. The insets show a closer look of the etched aluminium alloy surfaces.	33
Figure 3.2. 3D image of the 7 min acid solution etched aluminium surface and (b) its cross section surface morphology.....	35
Figure 3.3. The EDX spectrum of (a) 7 min acid solution etched and (b) 7 min acid solution etched and chlorosilane modified specimens (S71).....	37
Figure 3.4. Dynamic droplet/surface interaction on the surface of S71 specimen. Time between frames is about 25 milliseconds.....	39
Figure 3.5. The rolling droplet on the surface of S71 specimen which is tilted 2.65° . Each consecutive image (a–f) was taken at 50 milliseconds interval.....	40
Figure 3.6. The WCA of 8 μL droplet on the surface of the S71, S73, and S74 after 5, 10, 20, and 25 minutes. The size of the water droplets reduced successively due to evaporation.....	42
Figure 3.7. The WCA of S71 specimen putted in ultrasonic water bath for 5 to 70 minutes.....	43
Figure 3.8. The WCA of S71 specimen held at different temperatures. The insets show the water droplets on the surfaces after heating at different temperatures for 20 minutes.	45
Figure 3.9. Graphical abstract of the article paper entitled “A Cost-effective Method to Create Physically and Thermally Stable and Storable Super-hydrophobic Aluminium Alloy Surfaces”.....	49
Figure 4.1. XRD patterns of (a) bare T6-6061 AA, (b) cerium hydroxycarbonate coating synthesized through hydrothermal process (Sample S2), (c) cerium oxide coating formed through heat-treatment at 250°C . (d) The non-ambient XRD characteristic peaks of as deposited hydrothermal coating took at different temperatures in rang of 100°C to 400°C	62
Figure 4.2. ATR-FTIR spectra of the CeO_2 surface (a) before and (b) after TCOS surface treatment.	63

Figure 4.3. (a) and (b) display the surface XPS survey spectra of the cerium oxide coatings before and after surface modification with TCOS, respectively; and high-resolution surface XPS spectra of Ce 3d of (c) bare CeO ₂ and (d) modified CeO ₂ surface.	65
Figure 4.4. XPS spectra of (a) O 1s, (b) C 1s, and (c) Si 2p of the CeO ₂ surface. XPS spectra of (d) O 1s, (e) C 1s, and (f) Si 2p CeO ₂ surface after TCOS modification. (g) Schematic illustration of surface chemistry of modified cerium oxide coating.	67
Figure 4.5. (a) and (b) the schematics of horizontal and vertical sample positioning inside autoclave, respectively. The SEM images of (c) as-washed T6-6061 AA, (d) top surface with horizontal positioning, and (e) bottom surface of horizontal sample, respectively. (f) and (g) shows the SEM images of various places over vertically positioned surface.	70
Figure 4.6. (a), (b), and (C) are the optical images of a water droplet on the bare T6-6061 AA surface, as-prepared CeO ₂ coating, and TCOS modified CeO ₂ Coating (Sample 2), respectively. (d) Comparisons of the contact angle of water droplet on various surfaces after TCOS modification.....	73
Figure 4.7. (a–d) Low magnification SEM images, (e–h) High magnification SEM images, and (i–l) 3D surface profile of the S1 to S4 coatings grown on the bottom face of horizontally placed T6-6061 AA, respectively.	77
Figure 4.8. (a–d) Low magnification SEM images, (e–h) High magnification SEM images, and (i–l) 3D surface profile of the S5 to S8 coatings grown on the bottom face of horizontally placed T6-6061 AA, respectively.	80
Figure 4.9. (a) and (b) Low magnification SEM images, (c) and (d) High magnification SEM images, and (e) and (f) 3D surface profile of the S9 to S10 coatings grown on the bottom face of horizontally placed T6-6061 AA, respectively.....	83
Figure 4.10. (a) water droplet rolling down the superhydrophobic S2 coating. (b) High-speed photography images of a water droplet bouncing of the S2 coating (impact velocity $\sim 0.9 \text{ ms}^{-1}$). (c) Self-cleaning behavior of the superhydrophobic S2 coating. Scale bar $\sim 4.0 \text{ mm}$	84
Figure 4.11. Development of water contact angle and Rolling angle of the superhydrophobic S2 coating upon (a) dragging for 1.0 m length under varying applied pressure, (b) storing under ambient condition, (c) different pH values between 2 to 12, and (d) immersion time in 3.5 wt % NaCl aqueous solution.	86
Figure 4.12. The potentiodynamic polarization curves (Tafel plots) of the (a) bare and cerium oxide coated (S2 hydrothermal condition) T6-6061 AA, before and after surface modification; (b) bare and the superhydrophobic S1 to S4 coated T6-6061 AA.	88
Figure 4.13. Graphical abstract of the article paper entitled “Hydrothermal Deposition of Robust Cerium Oxide Based Superhydrophobic and Corrosion Resistive Coatings on Aluminium Alloy Substrates”.....	101
Figure S3.1. SEM image of 1 M NaOH treated aluminium alloy surface for 10 minutes that creates cone-like structure over the aluminium surface. The inset shows a closer look of a typically treated aluminium alloy surface.....	46
Figure S3.2. SEM images of the aluminium alloy surfaces etched for (a) 3 min and (b) 9 min in acid solution with volume ratio of $V_{H_2O} : V_{HCl} : V_{CH_3COOH} = 20 : 8 : 1$	47
Figure S3.3. The WCA and CAH of (a) S71, (b) S73, and (c) S74 specimens.	48
Figure S3.4. The WCA and CAH of (a) S76, (b) S77, and (c) S78 specimens.	48

Figure S3.5. The WCA of (a) S71, (b) S73, and (c) S74 specimens after immersing in water for 2 hours.	48
Figure S3.6. Retention of air bubbles on the Super-hydrophobic aluminium alloy surface after immersion in D.I. water for (a) 5 minutes, (b) 24 hours, and (c) 48 hours.	48
Figure S4.1. Schematic of the corrosion cell, (a) front view and (b) isometric view.	92
Figure S4.2. Schematic of Ag/AgCl reference electrode.	94
Figure S4.3. XRD patterns of S1 to S10 coatings (a) as-hydrothermally deposited and (b) after heat treatment at 250 °C.	95
Figure S4.4. Non-ambient XRD heating profile.	96
Figure S4.5. The non-ambient XRD characteristic peaks of as-deposited particles associated to experiment #2 processing condition at different temperatures in range of 100 °C to 400 °C.	96
Figure S4.6. Digital photographs of (a) and (b) deposited CeOHCO_3 on top face of horizontally placed sample. (c) Bare T6-6061 AA, (d) Ce(OH)CO_3 , and (e) CeO_2 coatings.	97
Figure S4.7. (a) and (b) The SEM image of the coating formed on top face of horizontally placed sample at different magnifications. (c) and (d) EDS Ce mapping of a place on top face of horizontally placed sample, which not covered with microstructural cerium oxide.	97
Figure S4.8. The SEM images of crack formation on S2 sample through heat treatment at (a) 250 °C and (b) 450 °C. The insets show a closer look of the cracks.	98
Figure S4.9. (a) Low magnification SEM image, (b) high magnification SEM image, and (c) surface 3D profile of as received T6-6061 AA.	98
Figure S4.10. (a–c) SEM images of coatings formed at 170 °C on the bottom face of horizontally placed samples using 50, 100 and 125 mL of solution, respectively. (d–f) High magnification SEM images of (a–c), respectively. The inset shows the closer look of pointed area.	99
Figure S4.11. The SEM images of the S2 coating after dragging for 1.0 m over abrasive paper under (a) 3.92 KPa and (b) 4.90 KPa applied pressures. (c) and (d) the high magnification images of the (a) and (b), respectively.	99
Figure S4.12. The Potentiodynamic polarization curves (Tafel plots) of (a) cerium hydroxylcarbonate and Cerium oxide coated T6-6061 AA; (b) bare and S5 to S8 coated T6-6061 AA; (c) bare, S2, S9 and S10 coated T6-6061 AA.	100

List of Abbreviations and Symbols

Abbreviation or Symbol	Definition
AA	Aluminum alloy
REO	Rare earth oxide
PTFE	Polytetrafluoroethylene
FAS	fluoroalkylsilane
TCODS	Trichloro(octadecyl)silane
TCDS	Trichlorododecylsilane
TCOS	Trichloro(octyl)silane
TMCS	Trimethylchlorosilane
WCA	Water contact angle
CAH	Contact angle hysteresis
RA	Rolling angle
SAM	Self-assembled monolayer
TMAH	Tetramethylammonium hydroxide
TTTS	(tridecafluoro1,1,2,2,tetrahydrooctyl)trichlorosilane
TTST	Tetrakis(trimethylsiloxy) titanium
ETS	Ethyltrichlorosilane
WE	Working electrode
CE	Counter electrode
RE	Reference electrode
SHE	Standard hydrogen electrode
E_{corr}	Corrosion potential
E_{pit}	Pitting potential
I_{corr}	Corrosion current density
R_{RMS}, S_a	Surface micro roughness
FCC	Face centered cubic

Acknowledgments

I would like to thanks my supervisors Dr. Martin Jun and Dr. Frank van Veggel for their helps, support, suggestions and insightful comments throughout my PhD studies. They have taught me how to work in a professional manner. I also wish to extend my thanks to the member of my committee Dr. Rustom Bhiladvala and Dr. Harry Kwok.

I would also thank Dr. Alexandre Brolo and Mahdih Atighi for the use of Brolo's Lab for electrochemical corrosion measurements, and Dr. Elaine Humphery for her support with SEM.

My special thanks go to my beloved parents Rezaali and Porandokht, my brother Hamed, and my sister Rahil for their lifetime support and love. They are always there for me.

And last but not least, I would like to thanks my beloved wife Haniye for her endless support, encouragement and patience. It would not be possible without your love.

Dedication

To the loving memory of my father

Chapter 1 Introduction

1.1 Research Motivation

Industrial applications of materials such as ceramics, metals, and polymers highly depend on their long-term properties. Among different materials, metals and metal alloys are the most applied materials in a variety of industrial and manufacturing applications due to their numerous properties, including excellent electrical and thermal conductivity, high strength, machinability, unique mechanical properties, and accessibility. However, physical and mechanical properties of metals can easily be deteriorated in contact with their surrounding environment, due to their high surface reactivity and feeble surface characteristics.¹⁻²

Metals can be destroyed by abrasion and/or wear, which cause loss of material from the surface by mechanical mechanisms.³ Besides, chemical interactions between metal and their environment may accelerate the damage and gradually decay the metal, which is known as corrosion.³ Metals corrosion usually happens in the presence of moisture and anions.² Therefore, limiting the surface reactivity and corrosion of the metals is of great importance for metals and their alloys' industrial applications. The need for corrosion protection is crucial, not only due to safety issues, but also from an economical point of view.^{1,3}

Cathodic protection,⁴ anodizing⁵ and developing protective coatings⁶⁻⁹ are some of the techniques, which have been studied to improve metals and metal alloys corrosion resistivity. Recently, developing corrosion protective coatings with special surface wettability attract tremendous attention for metals' surface protection.⁹⁻¹⁰ Wettability of a

surface is attributed to the ability of a surface to get, or not to get wet upon interaction with water.¹¹ Non-wetting property of the surfaces is attributed to their low-surface-energy and highly depends on their surface microtexture and morphology.¹²⁻¹³ Considering that metal surfaces are very susceptible to corrosion in the presence of water, developing non-wetting (superhydrophobic) coatings protects the metals surface by limiting the water and metal surface interaction.^{2, 14} Meanwhile, various surface properties, such as self-cleaning, anti-contaminaton, and drop-wise condensation, are ascribed to superhydrophobic surface characteristics.¹⁵

Chromate-based coatings had been conventionally utilized for more than decades for metals corrosion protection.¹⁶⁻¹⁷ However, high level of chromium components toxicity restricts the chromate-based coatings application in the corrosion industry.¹⁸⁻¹⁹ Among different chromate-free anti-corrosion coatings, cerium based oxides have been recently shown a promising improvement in metals and metal alloys corrosion protection (e.g. aluminium, magnesium, and stainless steel).²⁰⁻²⁴ The corrosion protection acquired by cerium based oxides can be further enhanced by introducing the superhydrophobicity to the coatings.²⁵ This can be obtained by utilizing appropriate techniques to create microtextured cerium based coating, following with a surface modification with low-surface-energy components.²⁶

The structures and features of the cerium oxide coatings' surface layer, which is inevitable for developing superhydrophobic surfaces, is hardly controllable by conventional coating methods,²⁷ such as sputtering, dip coating, sol-gel, chemical vapor deposition, and electrochemical deposition.^{8, 28-31} Among different cerium oxide synthesising methods hydrothermal possessing is known as an effective template-free

technique for synthesizing cerium oxide nanoparticles.³²⁻³³ However, just a few studies have been reported on developing a microstructural cerium oxide coating layer, using hydrothermal process.³⁴⁻³⁵

In this research work, a controlled hydrothermal deposition technique is employed to develop cerium oxide coatings with various surface microtextures. The superhydrophobicity of the coatings were rendered by further modifying the microtextured surface with trichloro(octyl)silane. Besides, a facile, practical, and cost-effective method was developed to generate physically and thermally stable superhydrophobic aluminium surfaces. Microstructural surface features over aluminium substrates were developed by a simple chemical etching approach, followed by a surface modification with various chlorosilanes, which are far cheaper than typical perfluorinated modifiers. In addition, chlorosilanes are readily available and their surface chemistry with OH groups is well documented.

1.2 Dissertation Outline

This dissertation includes the current introductory Chapter that provides the context and framework to link following Chapters in accordance to research and background information. A brief summary of literature review is presented in Chapter 2 in terms of wettability, cerium oxide and metals corrosion measurement. Chapters 3 and 4 are presented two papers, which have been accepted/submitted in peer-reviewed scientific journals. Each paper comprises its own abstract, introduction, materials and methods, results and discussion and conclusions. Finally, Chapter 5 summarizes the key developments and results, and suggests possible future considerations for this Ph.D research. The Chapters 3 and 4 are outlined as follows:

Chapter 3 presents a peer-reviewed published journal paper²⁶ and describes a facile and cost-effective method to create thermally and physically stable and storable superhydrophobic aluminium alloy surfaces. Development of a microtextured surface with a simple acid/base chemical etching is explained. The effect of chlorosilanes with various carbon chain lengths on resultant hydrophobicity has also been investigated.

Chapter 4 presents a peer-reviewed, submitted journal paper on the hydrothermal deposition of cerium based oxide coating layer with various surface microtextures. The impacts of different hydrothermal processing conditions on coating formation, morphology, and consequently wettability and corrosion resistivity are investigated. The mechanical abrasion resistance and chemical durability of the superhydrophobic coating are also evaluated.

Finally, Chapter 5 summarizes the main contributions and also suggests possible future research.

1.3 Research Contributions

The main objective of this research is, first of all, developing a facile and cost-effective method to generate superhydrophobic aluminium alloy surfaces with thermal and physical stability. Then, a controlled hydrothermal process is utilized to develop a physically and chemically stable, and durable superhydrophobic cerium oxide coatings on multi-purpose 6061 aluminium alloy substrates for improving their corrosion protection. The 6061 aluminium alloy has been used for several applications such as aircraft structures, yacht constructions, automotive parts, aluminium cans, etc.³⁶⁻³⁷ The novel contributions of the current dissertation are summarized as follows:

1. **Generating surface microstructures on aluminium alloys using a direct surface etching:** Direct utilizing hydrochloric and acetic acids as a facile and cheap technique to generate the desirable rough surface morphology on aluminium alloy substrates for developing superhydrophobic surfaces.
2. **Impact of different chlorosilanes on surface wettability:** The impact of chlorosilanes as a low-surface-energy surface modifier, in terms of concentration and hydrocarbon chain length, and on resultant surface wettability of the aluminium surfaces is investigated. The thermal and physical stability of the superhydrophobic surfaces are evaluated.
3. **Controlled hydrothermal deposition of microtextured cerium oxide coatings:** Cerium oxide coating with well-defined surface microtexture is developed on aluminium alloy substrates through a controlled hydrothermal deposition process. The impacts of various hydrothermal processing conditions, such as sample positioning, processing temperature, processing pressure and heating rate on resultant coating formation and morphology are investigated.
4. **The impacts of surface microtextures on surface wettability and corrosion protection:** The effects of various cerium oxide coatings with different surface microtextures on acquired wettability and consequently corrosion protection of aluminium alloy substrates are investigated.
5. **Durability of the non-wetting coatings evaluation:** The durability of the cerium oxide based superhydrophobic surfaces, in terms of mechanical wear-resistance and chemical stability, is thoroughly evaluated.

Chapter 2 Literature review

2.1 Non-wetting surfaces, from nature to artificial

2.1.1 Introduction

Biomimetic surfaces, which are based on mimicking biological surfaces, have led to great developments in manufacturing artificial surfaces with special properties. Some of the natural surfaces such as water strider leg, shark skin, mosquito eye, and lotus leaf show unique and unusual interaction with their surrounding fluids, and particularly water.³⁸⁻⁴¹ Among these special surfaces, Lotus leaf, *Nelumbo nucifera*, has been attracting tremendous attention due to its unique non-wetting and self-cleaning properties, which were described by Barthlott *et al.* in 1997.⁴ They revealed the interdependence of surface roughness, water repellency, and self-cleaning properties by characterizing the microscopic structure of Lotus leaf surface.¹³ A thin layer of waxy material with low-surface-energy/polarity, combined with geometrical microstructure of Lotus leaf, results in entrapment of air pockets on the surface, which is known as crucial reason for Lotus leaf extraordinary water repellency and self-cleaning.^{4, 15}

Recently, due to a variety of applications (e.g. corrosion inhibition improvement,⁴² friction drag reduction,⁴³ heat-transfer enhancement,⁴⁴ anti-icing⁴⁵ and self-cleaning⁴⁶⁻⁴⁷), superhydrophobic surfaces have gained tremendous attention. In the following sections, first, liquid/solid interaction theoretical models are presented, then the fundamentals and recent improvements in creating artificially designed superhydrophobic surfaces are briefly discussed.

2.1.2 Wettability (Theoretical Background)

Wettability refers to the tendency of a fluid to adhere or spread over a surface, which is defined by liquid with solid surface contact angle. For a static liquid droplet, the angle between the tangent line of a liquid-vapor interface interacts with a solid surface is called the contact angle (θ) and used as a scale to quantify the wettability of a solid surface related to the liquid phase (Figure 2.1 (a) and (b)).⁴⁸⁻⁴⁹ On the other hand, any contact angle which is measured on a droplet with movement on the solid surface is considered as the dynamic contact angle. Different methods have been reported to study dynamic interaction of a liquid and solid surface such as rolling angle and contact angle hysteresis. For a droplet moving on a tilted surface, a metastable droplet is formed; the droplet advances on the downhill and recedes on the uphill side (Figure 2.1 (c)). The difference between advancing and receding contact angle is known as contact angle hysteresis (CAH), which is attributed to surface chemistry and topography characteristics. The lowest tilting angle in which a droplet can roll over the substrates, rolling angle (RA), is considered as a scale to measure liquid repellency of the surface. Small substrate tilting angle is sufficient for water droplet to roll over a surface with low CAH and/or RA.⁵⁰⁻⁵¹

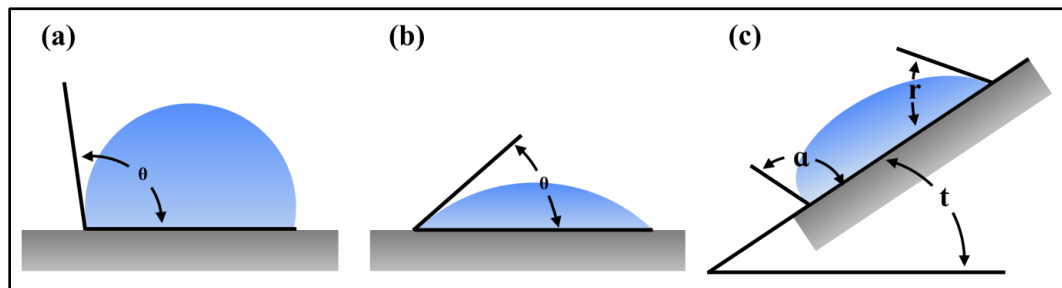


Figure 2.1. Schematic of a droplet (a) on hydrophobic surface (contact angle $\theta > 90^\circ$), (b) on hydrophilic surface (contact angle $\theta < 90^\circ$), and (c) advancing (α) and residing contact angle (r) on tilting surface.

In general, if $\theta \geq 90^\circ$, the solid surface is said to “not-like” the fluid droplet. On the other hand, if $\theta < 90^\circ$, the solid surface is said to “like” the fluid droplet. In case of using

water as liquid phase, the surfaces with water contact angle (WCA) less than 90° and 10° are called hydrophilic and super-hydrophilic, respectively. On the other hand, the term “hydrophobic surface” is used for water contact angle more than 90° . The surfaces with the $WCA \geq 150^\circ$ and $CAH < 10^\circ$ are called superhydrophobic, on which a water droplet forms an approximately perfect sphere on the surface and simply rolls off the surface.^{11, 15, 52-54}

The contact angle of a liquid on an atomically smooth solid surface is calculated by the Young’s equation (Figure 2.2(a)):

$$\cos \theta = \frac{(\gamma_{sv} - \gamma_{sl})}{\gamma_{lv}} \quad (\text{Eq. 2.1})$$

Where, γ_{sv} , γ_{sl} , γ_{lv} are interfacial tensions of the solid-vapor, solid-liquid, and liquid-vapor interfaces, respectively. However, Young’s equation cannot be applied for surfaces which are rough and chemically heterogeneous. The interaction of the liquids with solid surfaces is different in case of smooth and rough surfaces. Liquid/solid interaction, in case of rough surfaces, is described by the Wenzel and Cassie & Baxter models.^{12, 55}

Wenzel’s model is based on the assumption that the liquid penetrates into the rough grooves and the contact angle is calculated by the following equation (Figure 2.2(b)):

$$\cos \theta_w = \frac{r(\gamma_{sv} - \gamma_{sl})}{\gamma_{lv}} = r \cos \theta \quad (\text{Eq. 2.2})$$

Where, θ_w is the contact angle on the rough surface, θ is the Young’s contact angle on the atomically smooth surface which is made by same material, and r is the surface roughness factor which is equal to 1 for perfectly smooth surfaces and bigger than 1 for rough surfaces. The term “ r ” is defined as the ratio of the true area and geometric area.⁵⁶ According to Wenzel’s equation, the contact angle of the surfaces with $\theta > 90^\circ$ increases

by increasing the surface roughness. On the other hand, for the surfaces with $\theta < 90^\circ$, the contact angle decreases by increasing the roughness.⁴⁷

Surface roughness is a component of surface texture, which is quantified by the deviation of a real surface from its ideally flat form. Among various roughness parameters, R_a is the most common parameter that have been used to quantify surface roughness. R_a is the arithmetic average of the absolute values of the height deviates from the mean value of a line. S_a is the extension of R_a to a surface.⁵⁷

In contrary to Wenzel's model, the Cassie & Baxter's model is based on the assumption that the liquid does not go into the rough surface cavities and the cavities are filled with vapor instead of liquid. Per the Cassie & Baxter model the apparent contact angle (θ_c) is measured by following equation (Figure 2.2(c)):

$$\cos \theta_c = f_1 \cos \theta_1 + f_2 \cos \theta_2 \quad (\text{Eq. 2.3})$$

Where, f_1 and f_2 are the surface fraction of Phase 1 and 2, respectively; θ_1 and θ_2 are the Young's contact angle of phase 1 and 2, respectively. This equation is the general form of the Cassie & Baxter model which can be simplified for air as a vapor phase to the following equation:

$$\cos \theta_c = f \cos \theta + f - 1 \quad (\text{Eq. 2.4})$$

where, f is solid fraction which is defined as the fraction of the solid surface that is wetted by the liquid.¹² In the Cassie & Baxter state the small contact area between liquid droplet and rough surface results in easy droplet roll off on the surface. The solid/liquid interaction changes between the Wenzel and Cassie & Baxter states under different conditions such as droplet impact and press. Moreover, it has been reported that these two states coexist on nanopillared surfaces.^{13, 58-59}

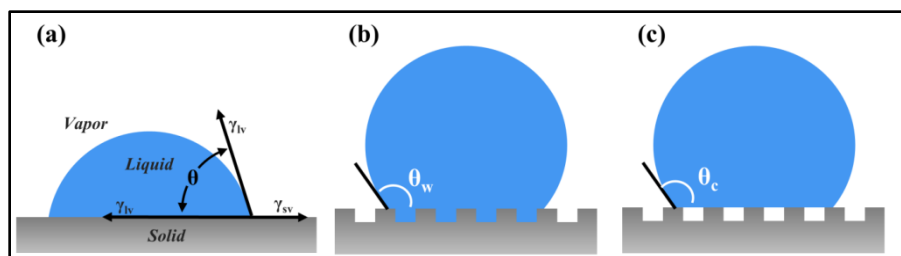


Figure 2.2. Schematic of interaction between a droplet and (a) a smooth substrate (Young's model), (b) a rough substrate regarding Wenzel model, and (c) a rough substrate regarding Cassie & Baxter model.

2.1.3 Developing Artificial Superhydrophobic surfaces

A surface, which exhibits a static water contact angle (WCA) $\geq 150^\circ$ and a water contact angle hysteresis (CAH) less than 10° is called superhydrophobic surface.⁶⁰ Biomimetic, Lotus leaf inspired, designed surfaces have been employed for creating artificial superhydrophobic surfaces; which are achieved by creating air entrapping zones on surface microstructures.⁵⁸ Surface energy and surface roughness are two key parameters that must be considered for creating superhydrophobic surfaces. For an atomically flat polytetrafluoroethylene (PTFE) surface, which is well-known for its low-surface-energy, the WCA cannot exceed 120° .⁶¹ Combined effects of low-surface-energy materials, surface morphology, and surface roughness yield to surfaces that exhibit WCA more than 160° and CAH less than 5° .

Generating durable metallic superhydrophobic surfaces is of great industrial and academical interest due to wide variety of applications in off-shore structures, marine applications, corrosion enhancement, etc.^{10, 14, 53, 62} Several strategies have been utilized to promote artificially superhydrophobic metallic surfaces, which are mostly based on two steps; first, tailoring surface roughness and topography, using direct surface treatment and/or applying rough coatings; followed by, surface modification by a low-surface-energy material such as fluorinated compounds.^{15, 47, 63}

Surface plasma treatment,⁶⁴⁻⁶⁵ laser ablation,⁶⁶ anodizing,⁶⁷ and chemical etching⁶⁸⁻⁶⁹ are some of the methods that have been used to manufacture directly the desired rough topography on flat surfaces. Additionally, several coating methods, e.g. electrochemical deposition,⁷⁰ chemical vapor deposition,⁷¹ sputtering,⁷² layer-by-layer deposition,⁷³ sol-gel processing,⁷⁴⁻⁷⁵ and recently hydrothermal processing³⁴ have been studied for developing an appropriate rough and microstructure designed base coating to enhance superhydrophobicity.

Coating or surface modification of roughened and microfeatured surfaces with low-surface-energy material is necessary to obtain superhydrophobic surfaces.^{40, 76} Organosilanes, such as fluoroalkylsilane (FAS)⁷⁷ and trimethylchlorosilane (TMCS),⁷⁸ and fatty acids including myristic acid,⁹ and stearic acid⁶⁰ are the most utilized low-surface-energy materials for surface modification. Silanes usually possess two major parts; an aliphatic carbon chain and a hydrolysable group for chemical anchoring to the surface. During the modification process the hydrolysable groups are hydrolyzed and condensed to oligomers. Subsequently, hydrogen bond form between OH groups on the substrate and oligomers. Eventually, covalent bonds are formed during a curing or drying process.⁷⁹⁻⁸⁰

During the last decade several researches have been dedicated to develop superhydrophobic surface. Followings are some brief examples from literature: Aytug *et al.* magnetron-sputtered optically transparent silica thin film on the glass substrate and chemically etched the surface to develop appropriate surface roughness; finally, micro-nano featured silica thin film, which was mechanically robust and hydrophilic, was modified by 1H,1H,2H,2H-perfluorooctyltrichlorosilane.⁸¹ Kang *et al.* electrodeposited

cluster-like cobalt layer on magnesium substrates, and consequently modified the rough surface by stearic acid for creating superhydrophobic and anti-corrosion coating layer.¹⁴

Li *et al.* fabricated a biomimetic-structural lanthanum oxide/hydroxide on aluminium substrates by hydrothermal method and reduced the surface energy by odecfluoroheptyl-propyl-trimethoxysilane modification.³⁵ Finally, Ishizaki *et al.* used an immersion method to coat a rough cerium oxide layer on magnesium substrates. They modified the rough ceria coating by FAS and tetrakis(trimethylsiloxy) titanium (TTST) to develop superhydrophobic and anti-corrosion layer which showed good adhesion to the magnesium substrate.⁸²

However, fabricating a superhydrophobic surface which is robust to harsh environments, in terms of mechanical wear-resistance and chemical stability, is still an outstanding challenge.^{81, 83} Abrasion is another important parameter affects the artificially microstructured superhydrophobic surfaces.⁸⁴ It is important to note that, these properties are main aspect of great importance to determine the industrial applications of superhydrophobic surfaces.⁸⁴

2.2 Cerium Oxide

2.2.1 Introduction

Cerium(IV) oxide, also known as ceria and cerium dioxide, is the most common compound of cerium. Cerium with atomic number of 58 and electron configuration of $[\text{Xe}] 4f^1 5d^1 6s^2$ is the most abundant rare earth element (0.0046 wt % of earth crust). Cerium(IV) oxide is a ceramic with a fluorite structure. Cerium(IV) oxide's band gap and refractive index are 3.23 ± 0.05 eV and 2.33 ± 0.08 eV, respectively. Ceria is a pale-

yellow ceramic with a melting point close to 2400 °C. Cerium(III) oxide with a hexagonal structure is another cerium compound that can occur in bulk cerium oxide at grain boundaries, oxygen vacancies, or produced by reduction of cerium(IV) oxide.⁸⁵⁻⁹⁰

2.2.2 CeO₂ Applications

Cerium-based oxides have been widely investigated for a variety of applications in UV absorbers,⁹¹ thermal barriers,⁹² drop-wise condensation for heat transfer improvements,⁹³ glass abrasive,⁹⁴ photocatalysis,⁹⁵ catalysis,⁹⁶ and corrosion prevention coatings.⁹⁷ Cerium oxide applications are mostly related to its oxygen storage capability, unique electronic structure, and crystal lattice structure.⁹⁸⁻¹⁰⁰

Recently, cerium oxide coatings have shown great promise in anti-corrosion properties of metallic surfaces.^{21-22, 28} Chemical conversion coatings, which are attributed to chemical or electrochemical processing of metal's surface to form a layer that contains the metal compounds, have been conventionally used for a long time to improve metallic surface characteristics, such as corrosion and wear resistance.¹⁰¹ Among different chemical conversion coatings, chromate conversion coatings have been broadly studied, due to its excellent corrosion protection of metallic substrates. However, during the last two decades, the use of chromium compounds in anti-corrosion coatings is being restricted due to their high toxicity.¹⁸ Consequently, different chromate-free conversion coatings have been studied as an alternative to chromate conversion coatings.¹⁰²

Breslin *et al.* used cerium conversion coating for improving magnesium and magnesium alloys corrosion resistance. Their results revealed that using cerium treatment led to a significant increase in corrosion resistance of magnesium in a buffer at pH 8.5.²³ Zuo *et al.* promoted a corrosion resistant cerium oxide based coating on aluminum alloy

by brush plating. Their results reveal that severe pitting happened on the bare aluminium alloy surface after 24 h of salt spray testing; however, only a few pits were observed on cerium oxide coated surfaces after 500 h of salt spray testing.⁷ Seal *et al.* investigated the high temperature oxidation resistance of stainless steel coated by nanocrystalline ceria. They observed that the coated substrates showed 90 % improvement in oxidation resistance at 970 °C in dry air, compare to uncoated stainless steel.¹⁰³

2.2.3 CeO₂ synthesizing and Coating methods

Different coating methods have been employed for creating cerium oxide coatings which can broadly be divided to vapor phase deposition and liquid phase methods.²⁷ Magnetron sputtering,¹⁰⁴ atomic layer deposition¹⁰⁵ and electron beam evaporation¹⁰⁶ are most studied vapor phase deposition methods. On the other hand, chemical conversion coating is the mostly used liquid phase method to create cerium-based coatings.⁹⁷ Sol-gel,²⁸ and electro-deposition²⁹ are some of other cerium-oxide liquid phase coating methods. The crystal growth and shape of the CeO₂ particles are not easily controllable by mentioned coating methods.²⁷

Geometrical designing and morphology control of nanostructures has been of great interest for bottom-up fabrication.¹⁰⁷⁻¹⁰⁸ Various aqueous-based techniques including sol-gel template process,¹⁰⁹ precipitation,¹¹⁰ and surfactant-assisted/free hydrothermal/solvothermal^{32, 107, 111} process have been reported for preparing control design of ceria nanoparticles. Hydrothermal synthesis, which is based on material's crystallization from high temperature aqueous solution at high vapor pressures, is known as one of the versatile methods for developing shape controlled nanoparticles.¹⁰⁷ Different types of cerium salts have been reported as CeO₂ precursors in hydrothermal

process including cerium(III) nitrate, cerium(III) chloride, and cerium(IV) sulfate. The size and morphology of the resultant ceria particles is directly influenced by the type and concentration of cerium salt precursor. Using Ce^{3+} salts in an alkaline solution leads to formation of $\text{Ce}(\text{OH})_3$ rod-like nuclei and after drying and heat treatment cerium(III) hydroxide converts to CeO_2 without any shape and morphology changes.^{33, 112-113} An oxidation step for transferring Ce^{3+} and Ce^{4+} is needed in case of cerium(III) salts precursor; while, shape and structure of synthesized ceria particles are more controllable using Ce^{3+} precursors.¹⁰⁷

Controlled hydrothermal synthesis of CeO_2 nanostructures is drastically influenced by anions and the pH. CeO_2 nanorods are only formed in acidic conditions, while presence of anions such as Cl^- , Br^- , I^- , and PO_4^{3-} are reported to promote ceria nanorods formation.¹¹¹ In contrast, alkaline conditions and NO_3^- results in gradually conversion of ceria nanorods to nanocubes.¹¹¹ For ceria hydrothermal coating over metallic substrates such as aluminium and steel, the substrates should be located inside aqueous solution consisting cerium precursor and mineralizer. Considering the fact that metallic substrates are deteriorated in presence of aggressive anions (i.e. Cl^- ions) and in highly acidic environments, which can be intensified in high temperature processing conditions; choosing appropriate precursor, mineralizer, and processing temperature is in great importance. For instance, using cerium nitrate as cerium source and Na_3PO_4 as mineralizer in deionized water leads to form uniform ceria nanorods;³² however, a low pH value of the solution results in the metal surface deterioration.

2.2.4 CeO₂ Wettability

Metal oxides such as aluminium oxide are hydrophilic due to their metal cation unfilled outer shell electronic structure.¹⁰⁰ During the last decade, different methods have been used for creating a superhydrophobic and anti-corrosion cerium-based coating on metallic surfaces. The utilized methods mostly consisted of creating a cerium-based coating followed by a surface modification process with low-surface-energy compound. Su *et al.* electro-deposited flower-like ceria on brass plates, followed by further surface modification with myristic acid as low-surface-energy component.¹¹⁴ Utilizing conversion coating method for coating aluminium substrate follow by stearic acid modification was reported by Jin Liang *et al.*¹¹⁵ Ishizaki *et al.* employed immersion in cerium nitrate method for coating magnesium substrates and used FAS (CF₃(CF₂)₇CH₂CH₂Si(OCH₃)₃).⁸²

In 2013, Varanasi *et al.* hypothesized that a series of rare-earth oxide ceramics, consist of CeO₂, Pr₆O₁₁, Nd₂O₃, Sm₂O₃, Eu₂O₃, Gd₂O₃, Tb₇O₁₂, Dy₂O₃, Ho₂O₃, Er₂O₃, Tm₂O₃, Yb₂O₃, and Lu₂O₃, are intrinsically hydrophobic.¹⁰⁰ They attributed the hydrophobicity of rare-earth oxides (REOs) to their unique electronic structure. A rare-earth element atom, in this case cerium(IV), has an unfilled 4f orbital which is restricted to interaction with outer environment by the full octant of electrons in its 5s²p⁶ shell.^{52, 100} As a result, rare-earth atoms do not have a tendency to interact with water and form hydrogen bonds. Consequently, hydrogen bonding just occurs at oxygen sites on the cerium oxide surface.^{52, 100}

However, not only is the underlying mechanism of REOs hydrophobicity still under debate, but also the reported water contact angles for the REOs, and particularly ceria, are

not consistent.^{93, 116} This can be attributed to delicate relation between the CeO₂ surface layer chemistry and its interaction with water molecules. It has been reported that various parameters, such as surface hydrocarbons adsorption and oxygen to metal ratio, which can alter the cerium oxide surface chemistry results in its hydrophobicity degradation.^{93, 104} In other words, the cerium oxide coatings' surface characteristics, and consequently their surface wettability, can easily be altered by exposure to various environments. Therefore, cerium oxide surface assembly with a low-surface-energy material is an inevitable step for developing durable non-wetting surfaces to serve in harsh environment.

2.3 Corrosion and Corrosion measurement

2.3.1 Introduction

Corrosion is defined as chemical degradation of materials such as metals, polymers, and ceramics in contact with their environment.¹ Among these, metals, as the most utilized materials in industry, are drastically vulnerable to naturally oxidise to their more stable components such as oxides and/or hydroxides.² Consequently, utilized metal in different industrial applications, including off-shore and marine, are severely affected by their feeble corrosion behavior in wet environments. The cost of corrosion and corrosion protection is estimated to be more than several billion Euros for even a small country such as Switzerland.² For instance, it has been reported that corrosion destroys approximately one quarter of the world's steel production. Therefore, promoting corrosion resistance of the metals by different methods such as fabrication anti-corrosion coatings have been in great importance for their industrial applications.¹⁻²

Most metals are not thermodynamically stable under moist conditions and gradually corrode in contact to their surrounding environments containing water, or even moisture. Special conditions, such as high oxygen concentration or presence of some species such as chlorides, can intensify the deterioration of the metals.² Corrosion gradually weakens and eventually destroys the metals and metal alloys structures.² It occurs on exposed metallic surfaces; therefore, different techniques have been used to reduce the activity of the exposed surface such as developing a coating layer to protect the exposed surface.¹¹⁷

2.3.2 Basics of metal corrosion electrochemistry

Corrosion of metals can be described via irreversible oxidation-reduction (redox) electrochemical reactions at interfaces of metal and electrolyte solution. Therefore, electrochemical methods have been used to study and measure metal corrosion for many years. Electrochemical reactions occur at metal-solution interfaces, while a metal surface is immersed in a given solution. The electrochemical metal's corrosion measurement methods are based on two hypotheses: i) electrochemical reaction can be divided into two or more partial oxidation and reduction reactions in which the metals are oxidized at anodic site and release metal ions into solution (metal corrosion). ii) There is no net electric charge during an electrochemical reaction, which is a restatement of conservation of charge law.⁵

For better understanding of electrochemical corrosion reactions, a simple system in which a metal (M) corrodes in an acidic solution in the absence of oxygen is described, and is schematically presented in Figure 2.3(a). Oxidation reaction occurs at an anodic site, where a metal surface (M) is oxidized into its ionic species (M^{n+}) and released into solution; meanwhile, n electrons (oxidized state of metal) release in the metal bulk for

each atom of M (Figure 2.3(a), eq. I). Besides, at a cathodic site, in order to maintain electron neutrality in acidic solutions, hydrogen ions obtain electron, which are released from metal atoms to form gaseous hydrogen (H_2) (Figure 2.3(a), eq. II).^{2, 5, 118}

The redox reactions on a specific metal surface promote an electrochemical potential (E_{MS}) at metal/solution interface, which is attributed to specific electrochemical metal and its surface properties. The metal corrosion potential is usually measured with respect to a reference electrode, since all voltage measuring apparatuses measure a potential difference. The electrochemical potential difference between a metal and reference electrode (E_{ref}) is known as corrosion potential (E_{corr}). E_{corr} is the potential at which the rate of oxidation at anode is equal to the rate of hydrogen reduction at cathode (Figure 2.3(b)). Standard hydrogen electrode (SHE), Silver Chloride, and Saturated Calomel Electrode (SCE) are some of commonly used reference electrode in potential measurement.² The results acquired using each reference electrode can easily be converted to the other ones (Figure 2.3(b)).^{2, 5, 118}

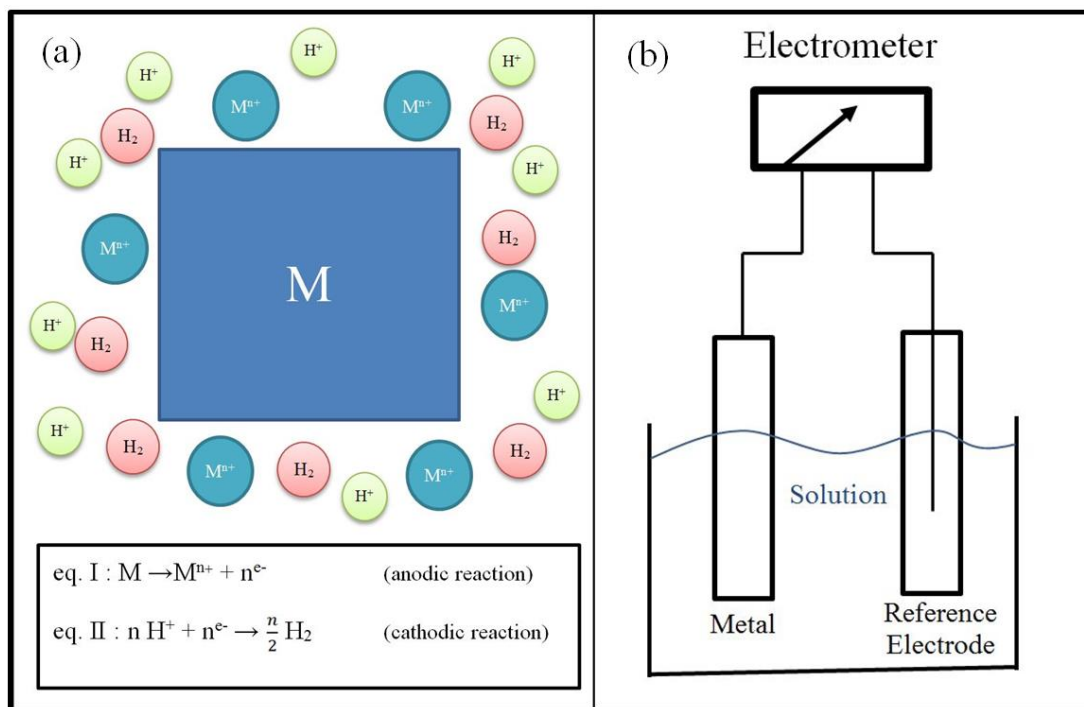


Figure 2.3. (a) A schematic of metal corrosion in acidic solution. (b) A schematic of a system, which the potential difference between a metal and a reference electrode is measured.

The corrosion potential (E_{corr}) is the result of a natural reaction between the metal and the solution. However, the potential can be imposed from an external device, which disturbs the electron balance that normally happens at E_{corr} . An electrode is known to be polarized, when imposing to a potential other than corrosion potential. Anodic and cathodic potentials (with respect to metal's E_{corr}) will speed up the oxidation and reduction reactions, respectively. Applying anodic potentials increases the oxidation reaction, which leads to an increase in anodic current (i_a). On the other hand, applying cathodic potentials accelerate the reduction reaction, which results in an increase in cathodic current (i_c). Anodic and cathodic currents are equal but flow in opposite directions at metal's E_{corr} .

The value of current flow at corrosion potential, which is measured by electrochemical instrument, is zero; since i_{total} is equal to summation of i_c and i_a at E_{corr} .^{2, 5, 118} Therefore, the corrosion current cannot be measured directly due to instrumental limitation. However, the values of i_c or i_a , known as corrosion current (i_{corr}), can be determined by controlled polarizing and measuring the resulting current of metallic species.^{2, 5, 118}

2.3.3 Corrosion rate measurement through Tafel extrapolation

Figure 2.4 represents a schematic of a typical electrochemical cell which is used for corrosion measurements. External potential applies between the reference electrode and metal specimen (also known as working electrode); while, the counter electrode is utilized to measure the current flowing at metal specimen during the test. It is important to stress that the current flow, which is measured at counter electrode, is the total current (i_{total}).¹¹⁸⁻¹¹⁹

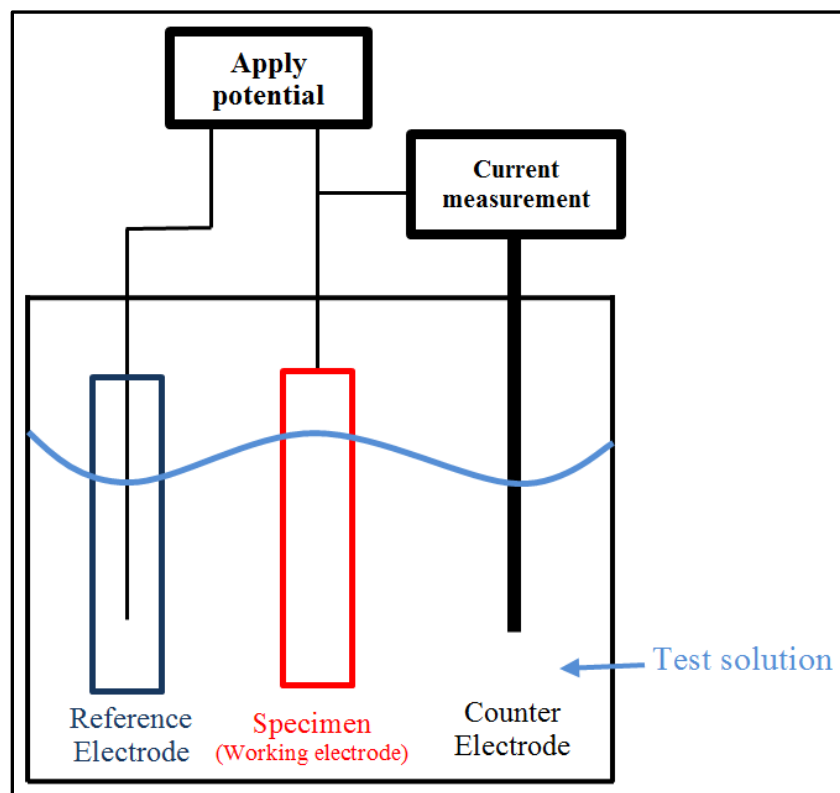


Figure 2.4. A schematic of a three-electrode potentiodynamic electrochemical corrosion testing system.

Corrosion rate can directly be calculated by following equation:¹¹⁹

$$\text{Corrosion rate (MPY)} = \frac{0.13 i_{corr} (E.W.)}{A d} \quad (\text{Eq. 2.5})$$

Where,

MPY = milli-inches per year

$$E.W. (\text{Electrochemical equivalent weight (gr)}) = \frac{\text{Atomic weight}}{\text{Number of electrons interacting}}$$

A = area of exposed surface (cm²)

d = density of substrate material (g/cm³)

Solution of this equation depends on finding the corrosion current value. Potentiodynamic electrochemical methods, and particularly Tafel extrapolation, which have been evaluated both theoretically and empirically, have been widely used for corrosion current measurement.¹¹⁹ A typical Tafel plot is comprised of cathodic and anodic Tafel plots, which are generated by scanning to -250 mV vs. E_{corr} (cathodic Tafel plot) and +250 mV vs. E_{corr} (anodic Tafel plot). The anodic and cathodic Tafel plot can be determined by anodic (Eq. 2.6) and cathodic (Eq. 2.7) Tafel equation as follow:

$$\eta_a = \beta_a \log i_a + C \quad (\text{Eq. 2.6})$$

$$\eta_c = \beta_c \log i_c + C \quad (\text{Eq. 2.7})$$

Where, η_a , β_a , and i_a are attributed to anodic over potential, Tafel slope, and current, respectively; η_c , β_c , and i_c are ascribed to cathodic over potential, Tafel slope, and current, respectively; and C is a constant.

Tafel corrosion measurement technique consists of applying potentials and scanning resulting currents. Figure 2.5 shows a schematic of a typical Tafel plot. In the corrosion measurement systems, which are based on Tafel extrapolation, the applied potential is plotted vs. logarithm of current. According to the Tafel equation the logarithm of the current varies linearly with the potentials in ranges between -50 mV and -250 mV vs. E_{corr} for cathodic and +50 mV and +250 mV vs. E_{corr} for anodic Tafel plot, respectively.¹ Corrosion current can be calculated directly from Tafel plot by finding the intersection of anodic and cathodic Tafel current extrapolation. The two fitted lines intersect at E_{corr} , and consequently the corrosion current can be calculated.^{2, 118-119}

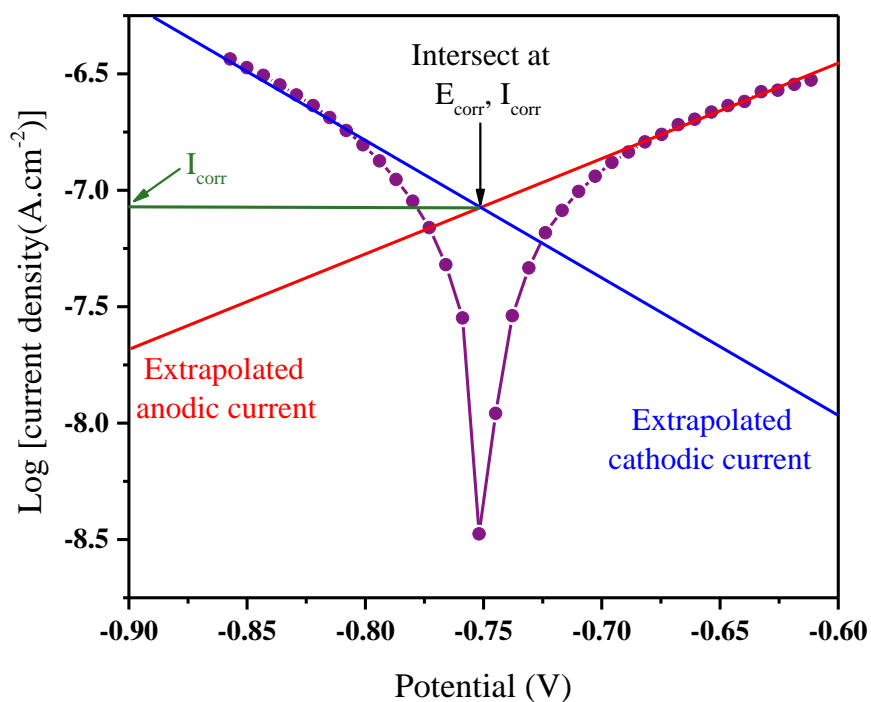


Figure 2.5. Schematic of a typical Tafel plot in which E_{corr} and I_{corr} correspond to corrosion potential and corrosion current, respectively.

Chapter 3 A Cost-effective Method to Create Physically and Thermally Stable and Storable Super- hydrophobic Aluminium Alloy Surfaces

This paper was published in Journal of Surface and Coating Technology.²⁶

Ahmad Esmaeilirad, Maxym V. Rukosuyev, Martin B.G. Jun, and Frank C. J. M. van Veggel. “A Cost-effective Method to Create Physically and Thermally Stable and Storable Super-hydrophobic Aluminium Alloy Surfaces.” Journal of Surface and Coating Technology 285 (2016): 227-234. [<https://doi.org/10.1016/j.surfcoat.2015.11.023>]. The paper is presented with some minor editorial revisions.

3.1 Abstract

Physical and thermal stability of super-hydrophobic surfaces are some of the most significant issues for applying them in industry. A facile and cost-effective method has been developed to create thermally and physically stable and storable super-hydrophobic aluminium alloy surfaces. Chemical etching by sodium hydroxide and a solution of acetic acid and hydrochloric acid were used to create micro-nano structures over the surface and subsequently trichloro(octadecyl)silane (TCODS), trichlorododecylsilane (TCDS), and trichloro(octyl)silane (TCOS) were used to modify these roughened surfaces. The effects of different etching processes, different type of chlorosilanes, and the amount of modifiers on the resultant aluminium alloy surfaces hydrophobicity were also investigated. The resulting surface morphologies, compositions, roughness, and water contact angle were investigated by scanning electron microscopy, energy dispersive X-

ray spectroscopy (EDX), 3D surface profilometer, and water contact angle (WCA) meter, respectively. Photron APX-RS high speed camera was used for imaging contact angle hysteresis (CAH) and dynamic droplet/surface interaction. The WCA and water contact angle hysteresis (CAH) of the aluminium alloy surfaces modified by TCODS reached to $165 \pm 2^\circ$ and less than 3° , respectively; and it remained super-hydrophobic after 100 hours immersing in water, 30 min ultra-sonication, stored for more than 30 days under ambient condition, and heated to 375°C for 20 min.

3.2 Introduction

The concept of super-hydrophobicity is borrowed from the reputed Lotus leaf effect described by Barthlott *et al.* in 1997.¹²⁰ In order to achieve super-hydrophobic surfaces which exhibit high water contact angle (WCA) with values over 150° and a small hysteresis contact angle (HCA) of less than 10° , a low-surface energy coating over a micro-nano structured surface is required. For atomically flat surfaces, materials with low-surface-energy exhibit WCA of around 120° at best. For roughened surfaces, however, WCA can exceed 160° due to a combined effect of low-surface-energy, air entrapment, and other contributing factors such as surface morphology.^{46, 121-124} During the last decade, super-hydrophobic surfaces have attracted enormous attention in fundamental research as well as industrial aspects due to a variety of applications in anti-corrosion, self-cleaning, biomedical applications, anti-icing, friction drag reduction, anti-bio fouling paints, etc.^{43, 45, 53-54, 69, 125-129} Considering the fact that aluminium alloys are the most widely used non-ferrous materials in industry, producing super-hydrophobic surfaces based on aluminium alloys has attracted a lot of attention during recent years.^{9, 60}

Superb heat and electrical conductivity, low weight, and high strength are some of aluminium alloys' properties which have caused wide usage of them in marine structures, building construction, airplanes, etc.¹³⁰⁻¹³¹ Many methods have been used for generating super-hydrophobic aluminium surfaces which are mostly a combination of roughening and treating the surface with low-surface-energy materials. Layer by layer deposition,⁷³ chemical deposition,^{70, 131-132} plasma surface treatment,⁶⁴ anodizing,^{9, 130, 133} electrospinning,⁷² sputtering,⁶⁷ and etching aluminium surfaces following by surface modification with low surface-energy materials,^{60, 68, 134} are some of the approaches for creating a super-hydrophobic aluminium surfaces.¹⁵

Organosilanes such as methylsilanes, linear alkyl-silanes, aromatic-silanes, perfluorinated alkyl-silane are the most widely used materials for super-hydrophobic surface modification. Most of the silanes possess three major parts; an organo-functional group, a linker, and hydrolysable groups for chemical anchoring to the surface. During the modification process the hydrolysable groups are hydrolyzed and condensed to oligomers. Subsequently, hydrogen bond form between OH groups on the substrate and oligomers. Eventually, covalent bonds are formed during a curing or drying process.¹³⁵ The presence of aliphatic hydrocarbon substituent or fluorinated hydrocarbon substituent enables a surface to show hydrophobic properties. The linker length possesses an important role in the hydrophobicity of a surface by affecting reactivity restrictions and physical properties. Use of long chain silanes often leads to Self-Assembled Monolayers (SAMs).^{15, 68-69, 79, 136-137}

The stability, durability, and storing properties of the super-hydrophobic surfaces are three main aspects of great importance that determine their possible applications in

industry. There are several articles about these properties of super-hydrophobic surfaces in literature,^{14, 78, 81, 83, 100, 138-139} but just a few studies focus on super-hydrophobic aluminium surfaces stability properties.^{25, 84, 140-141}

In this paper, we described a facile, practical, and cost-effective method for creating physically and thermally stable and storable super-hydrophobic aluminium surface which is favorable for many industrial applications. Comparing to most commonly used anodizing process, our direct use of hydrochloric and acetic acids is more facile and much cheaper for creating the desirable rough surface morphology. Additionally, chlorosilane modifying agents that were used in this work to create super-hydrophobic surfaces are far cheaper than perfluoropolymers and other typical modifiers. By using the above simple and cost-effective method super-hydrophobic aluminium surfaces with water contact angle of $165 \pm 2^\circ$ and contact angle hysteresis less than 3° were obtained which were as good as most other super-hydrophobic aluminium surfaces described in literature that mostly used more expensive methods and modifiers. The resultant super-hydrophobic aluminium surfaces showed short-term stability under water and storability for more than six months without remarkable changes which show their potential long-term stability, and storability. The super-hydrophobic aluminium surfaces were also thermally stable until 375°C .

3.3 Experimental Section

3.3.1 Materials

Sheet of cast aluminium alloy (AA 6061) was the main material for making Aluminium alloy substrates. Hexane (ACS reagent $\geq 99\%$), trichloro(octadecyl)silane (TCODS) (\geq

90 %) , trichlorododecylsilane (TCDS) (≥ 95.0 %), and trichloro(octyl)silane (TCOS) (≥ 97 %) were purchased from Sigma Aldrich, Sodium Hydroxide, and Hydrochloric Acid ACS reagent (37 %) from Anachemia, and Acetic Acid ACS grade(≥ 99 %) from VWR. The deionized water (D. I. water) used was of purity of > 18 M Ω .

3.3.2 Aluminium Surfaces Roughening and Surface Modification Procedure

The aluminium alloy substrates ($1 \times 1 \times 0.06$ in³) were mechanically roughened by abrasive papers #600 and #1500, respectively until a homogeneous surface with surface micro roughness (R_{RMS}) equal to 0.5 ± 0.1 μ m was obtained. The roughened aluminium alloy surfaces were ultra-sonically cleaned by acetone and D.I. water and dried for 10 min in 110 °C. The clean aluminium alloy sheets were then treated by 1 M NaOH for 10 min and ultra-sonically cleaned by D.I. water and dried for 10 min in 110 °C. Subsequently, they were immersed in a mixture of D.I. water, hydrochloric acid, and acetic acids at volume ratio of $V_{H_2O} : V_{HCl} : V_{CH_3COOH} = 20 : 8 : 1$ for different times at room temperature and rapidly washed and ultra-sonically cleaned by D.I. water and dried at 110 °C for 10 min.

The roughened and chemically etched aluminium alloy substrates were modified by 2 mL to 6 mL of TCODS, TCDS, and TCOS as shown in Table 3.1. Surface modification was carried out by simply immersing aluminium surfaces in the solution of chlorosilane and 50 mL hexane for 2 hours and rinsing by hexane. The resultant samples then heat treated at 200 °C for 60 min for increasing their stability.

For testing the storability of the hydrophobic properties of the modified aluminium alloy surfaces, WCA was measured after 10, 20, 30, and 180 days storing the modified aluminium alloy surfaces at room temperature.

Table 3.1. The roughening process, surface modifier, amount of modifier, roughness, WCA, and CAH of the specimens.

specimen	Roughening	NaOH ^a	Acid ^b (min)	Surface Modifier	Modifier amount (mL)	Roughness (μm)	WCA ^c ($^{\circ}$)	CAH ^d ($^{\circ}$)
S00	N/A	N/A	N/A	N/A	N/A	0.5 ± 0.1	60 ± 1	> 10
S01	×	×	N/A	TCODS	3	0.9 ± 0.1	133 ± 2	> 10
S02	×	×	N/A	TCODS	6	0.9 ± 0.1	138 ± 3	> 10
S03	×	×	N/A	TCDS	3	0.9 ± 0.1	130 ± 2	> 10
S04	×	×	N/A	TCOS	3	0.9 ± 0.1	125 ± 2	> 10
S51	N/A	×	5	TCODS	3	3.3 ± 0.1	154 ± 2	< 6
S52	×	×	5	TCODS	3	3.5 ± 0.1	158 ± 2	< 5
S53	×	×	5	TCODS	6	3.6 ± 0.1	161 ± 2	< 4
S71	×	×	7	TCODS	3	5.4 ± 0.1	165 ± 2	< 3
S72	×	N/A	7	TCDS	3	3.1 ± 0.1	160 ± 3	< 5
S73	×	×	7	TCDS	3	4.9 ± 0.1	163 ± 3	< 4
S74	×	×	7	TCOS	3	4.6 ± 0.1	159 ± 2	< 5
S75	×	×	7	TCODS	2	5.3 ± 0.1	151 ± 5	< 6
S75	×	×	7	TCODS	4	5.3 ± 0.1	165 ± 2	< 3
S76	×	×	7	TCODS	5	5.4 ± 0.1	166 ± 2	< 3
S77	×	×	7	TCODS	6	5.1 ± 0.1	166 ± 2	< 3

a) NaOH: 1 M NaOH treatment for 10 min

b) Acid: acid solution volume ration is equal to ($V_{\text{H}_2\text{O}}: V_{\text{HCl}}: V_{\text{CH}_3\text{COOH}} = 20 : 8 : 1$)

c) WCA: Water Contact Angle

d) CAH: Contact Angle Hysteresis

Three different methods had been used to investigate the stability of the aluminium super-hydrophobic surfaces under water. First the WCA changes of an 8 μL water droplet were measured as a function of time that water droplet connecting to the surface continuously for 25 min. In the second method the S71 specimen was immersed in the D. I. water at depth of 10 cm up to 100 hours and the WCA was measured after drying the specimen for 2 hours in room temperature. In the third method the S71 specimen was putted in ultrasonic water bath for 5 to 70 min.

For testing the thermal stability of the super-hydrophobic surfaces, WCA of the surfaces was measured after heating them to 100, 200, 300, 350, 400, 425 °C for 20 min. The samples were cooled down and rested in laboratory air for 2 hours before WCA measurements.

3.3.3 Characterization

Scanning electron microscopic (SEM) and Energy-dispersive X-ray spectroscopy (EDX) images and spectrums were taken on a Hitachi S-4800 field emission scanning electron microscope. The SEM acceleration voltage was set to 1.0 kV at working distance from 4.00 mm to 8.7 mm. In order to avoid surface charge during SEM, the surfaces were carbon coated for 6 times (~ 9 nm) before SEM imaging at a vacuum of 10^{-4} mbar, using 208 CRESSINGTON carbon coater. Zeta 3D profilometer as used for measuring surfaces micro-roughness and taking surface 3D images. A Holmarc contact angle meter model HO-IAD-CAM-01B was used in order to evaluate water contact angle (WCA) and water contact angle hysteresis (CAH). Deionized 4 μ L volume water droplet was deposited on three different places over aluminium alloy substrates and the mean value of the measured water contact angles of the both side of the droplet with deviations were reported. The contact angle hysteresis (CAH) was measured by tilting the specimen stage and dropping a deionized 8 μ L water droplet on the surfaces. The images of CAH and dynamic droplet/surface interaction were taken by Photron APX-RS high speed camera at rate of 1000 frames per second. Ultrasonic water bath (Branson 1510R-DTH) with frequency of 40 kHz and maximum draw power of 143 Watts was used to investigate the physical stability of the super-hydrophobic surfaces.

3.4 Results and Discussion

3.4.1 Roughening Procedure of Aluminium Alloy Surfaces

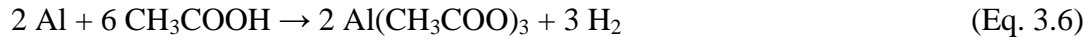
The roughness, micro-structure, and typical topography wavelength of the surfaces play a significant role in developing small air trapping zones and eventually creating super-hydrophobic surfaces. The rough aluminium alloy surfaces with micro-roughness around $5.0 \pm 0.5 \mu\text{m}$ and micro-size cavities were produced by 1 M NaOH treatment for 10 min followed by 7 min acid solution etching (Table 3.1).

The surface micro roughness (R_{RMS}) of the aluminium alloy surface that was roughened by abrasive paper ($0.5 \pm 0.1 \mu\text{m}$) was increased to $0.9 \pm 0.1 \mu\text{m}$ by the 1 M NaOH treatment for 10 min (Figure S3.1). Sodium hydroxide reacts and dissolves the passive impermeable aluminium hydroxide and aluminium oxide layer over the aluminium substrates by producing $[\text{Al}(\text{OH})_4]^-$ and aluminium hydroxide $\text{Al}(\text{OH})_3$ which go into solution and this creates cone-like micro-features over the surface of the aluminium.¹⁴²



A micro-feature rough structure with micrometer size cavities were developed over the 1 M NaOH treated aluminium alloy surfaces (Figure 3.1) by 5 min acid solution etching ($V_{\text{H}_2\text{O}} : V_{\text{HCl}} : V_{\text{CH}_3\text{COOH}} = 20 : 8 : 1$). Although acetic acid is aggressive to bare aluminium surfaces, it cannot dissolve aluminium oxide layer.¹⁴² Therefore, a solution of acetic acid and hydrochloric acid was used for etching aluminium and producing a uniformly rough surface which was essential for making a surface super-hydrophobic. Different concentrations and etching times of acetic acid and hydrochloric acid were used to

prepare the appropriate surface morphology and roughness. Eventually, the volume ratio of $V_{\text{H}_2\text{O}}:V_{\text{HCl}}:V_{\text{CH}_3\text{COOH}}= 20 : 8 : 1$ showed the best results for etching aluminium substrates.



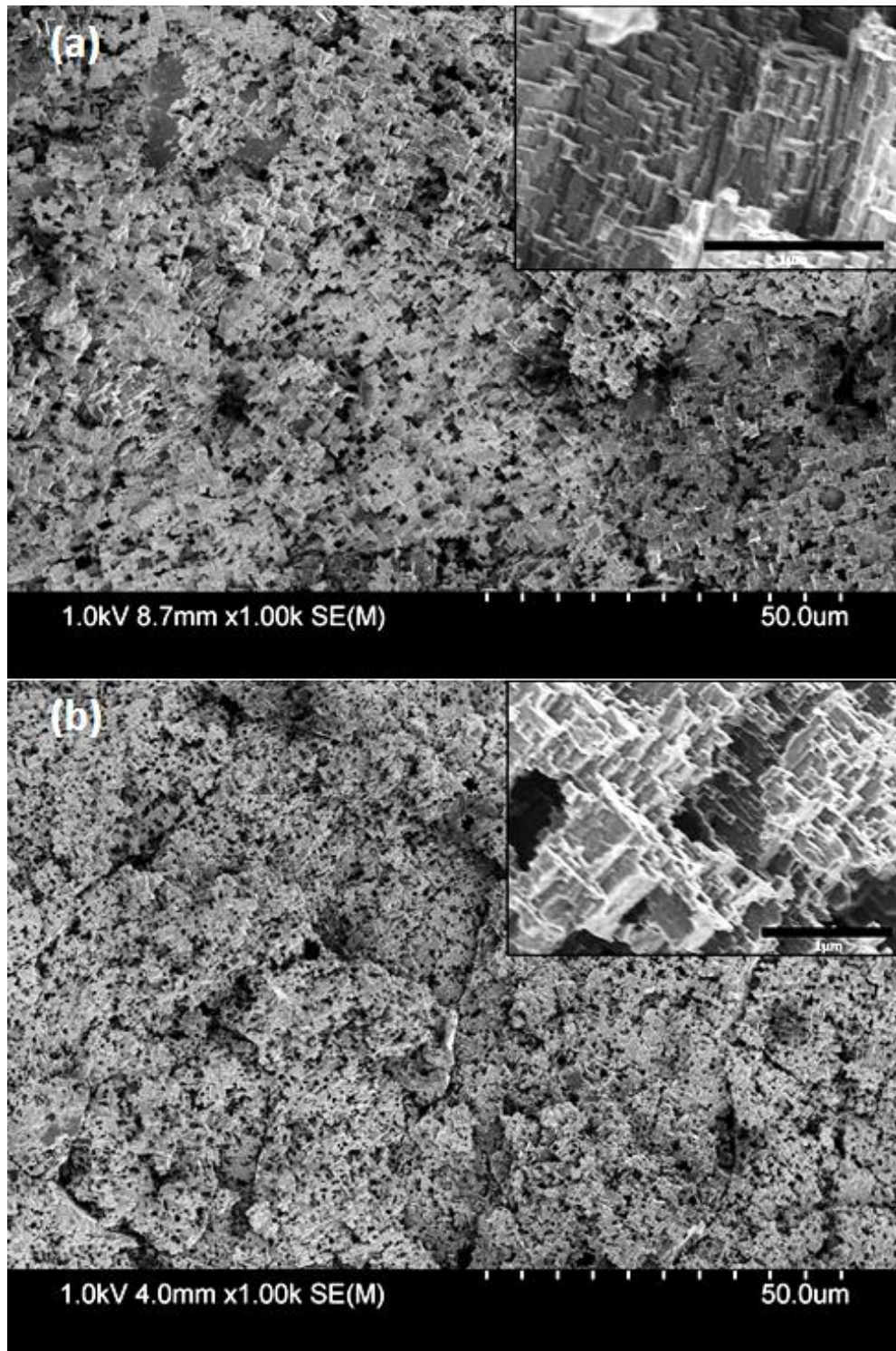


Figure 3.1. SEM images of the aluminium alloy surfaces etched for (a) 5 min and (b) 7 min in acid solution with volume ratio of $V_{H_2O} : V_{HCl} : V_{CH_3COOH} = 20 : 8 : 1$. The insets show a closer look of the etched aluminium alloy surfaces.

Subsequently, the surface roughness of the NaOH treated and 5 min acid solution etched surfaces was increased by extending the acid etching time for 2 more min. The SEM images of the 5 min and 7 min acid solution etched specimens are shown in Figure 3.1(a) and (b), respectively. It can be observed from Figure 3.1(a) that a micro-porous surface with regular bulged structures that have appropriate zones for trapping the air had been created by 5 min acid solution etching. The micro-porous structures were regular and coherent over the surface. The 3D image of the 7 min acid etched aluminium surface and its cross section surface morphology are shown in Figure 3.2(a) and (b), respectively. It can be seen from Figure 3.2 that the acid solution etching had created lots of air trapping desirable micro-size holes and cavities with average width of $12 \pm 5 \mu\text{m}$. The surface morphology is fairly consistent all over the surface. Wettability of the superhydrophobic aluminum alloy surface was fairly constant all over the surface, which is attributed to uniformity of surface microtexture and roughness. It can be seen from Figure 3.1(b) that the micro-porous structure became finer by increasing acid solution etching time which provided better sites for trapping air. By increasing the etching time to more than 7 minutes the surface micro and brick-like structure were destroyed and numerous big holes of more than $5 \mu\text{m}$ in diameter were developed over surface that were not appropriate for trapping air (Figure S3.2(b)). In contrast, for acid etching time less than 5 min the surface structure was not uniform and appropriate for desirable surface structure (Figure S3.2(a)).

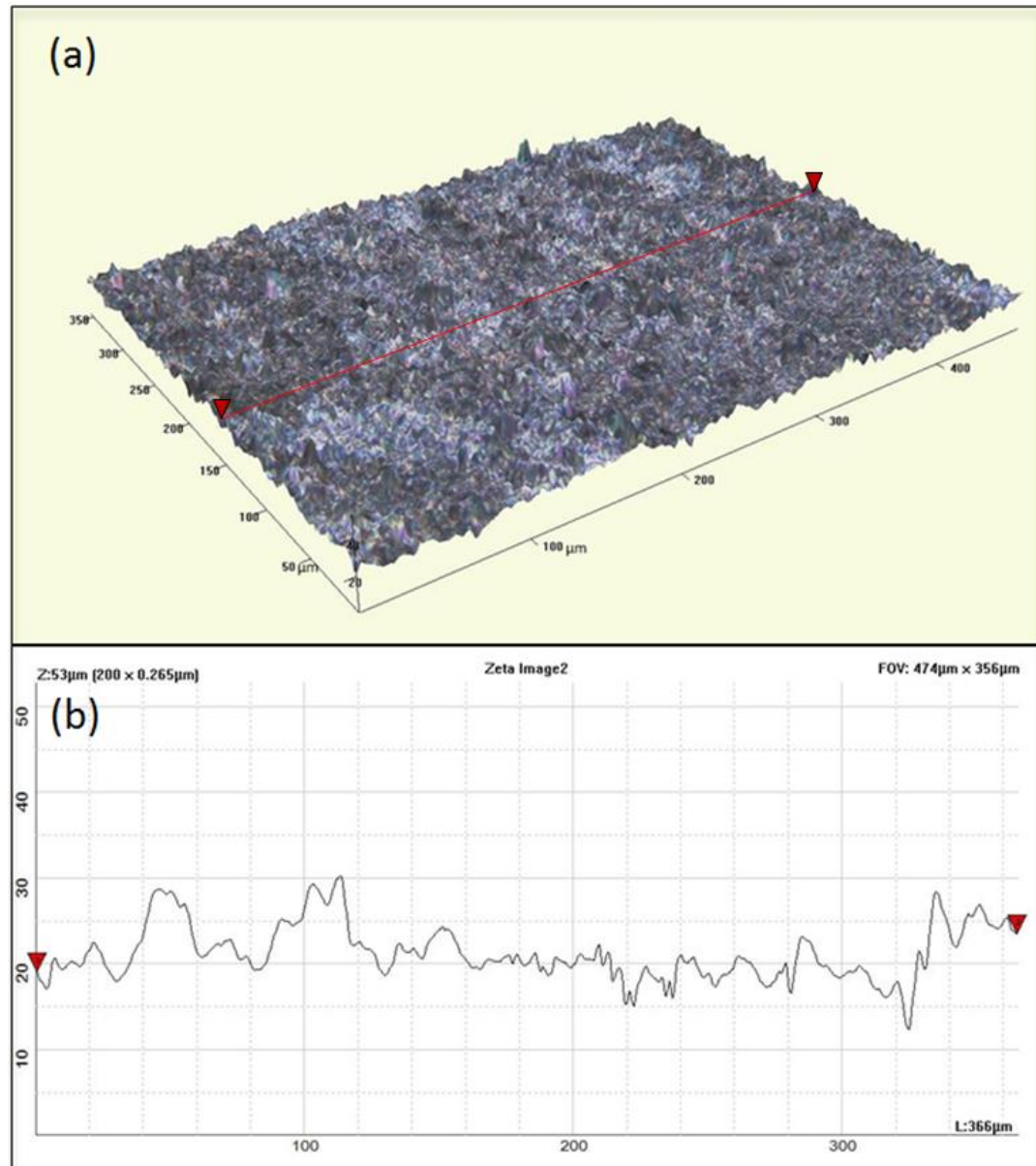


Figure 3.2. 3D image of the 7 min acid solution etched aluminium surface and (b) its cross section surface morphology.

Based on the results are shown in Table 3.1, the roughening by abrasive paper effects on the roughness and subsequently WCA were investigated by comparing S51 and S52 specimens. The comparison shows that roughening by abrasive paper enhanced the surface roughness about 0.2 μm , the WCA by 4°, and reduced the CAH by about 1°

which clearly shows that roughening the surface improves the hydrophobic properties of the final aluminium alloy surfaces. The effect of 1 M NaOH treatment on the ultimate roughness of the aluminium alloy surfaces was also investigated by comparing S72 and S73 specimens. It can be seen that a 10 min 1 M NaOH treatment increased the surface micro-roughness significantly from 3.1 ± 0.1 to 4.9 ± 0.1 μm and subsequently the WCA by 3° , and reduced the CAH by 1° .

3.4.2 Super-hydrophobic characterization

The effects of surface roughness, micro-structure, amount, and type of chlorosilane modifiers were investigated. The S71 specimen exhibited the best hydrophobicity properties with surface roughness of 5.4 μm , WCA of $165 \pm 2^\circ$, and CAH less than 3° . Table 3.1 shows that the super-hydrophobic properties of the aluminium alloy surfaces were increased by using higher linker length chlorosilane modifier, increasing the amount of chlorosilane modifier, and the surface roughness.

Figure 3.3(a) shows the EDX spectrum of the 7 min acid solution etched specimen and Figure 3.3(b) shows the EDX spectrum of S71 specimen which was etched for 7 min in acid solution and modified with chlorosilane. The peaks at 0.50 and 1.25 keV belong to chromium and magnesium, respectively, and are due to the fact that the AA 6061 aluminium alloys contain chromium and magnesium. The silanization of the modified specimen was confirmed by appearance of silicon peak in the EDX spectrum.

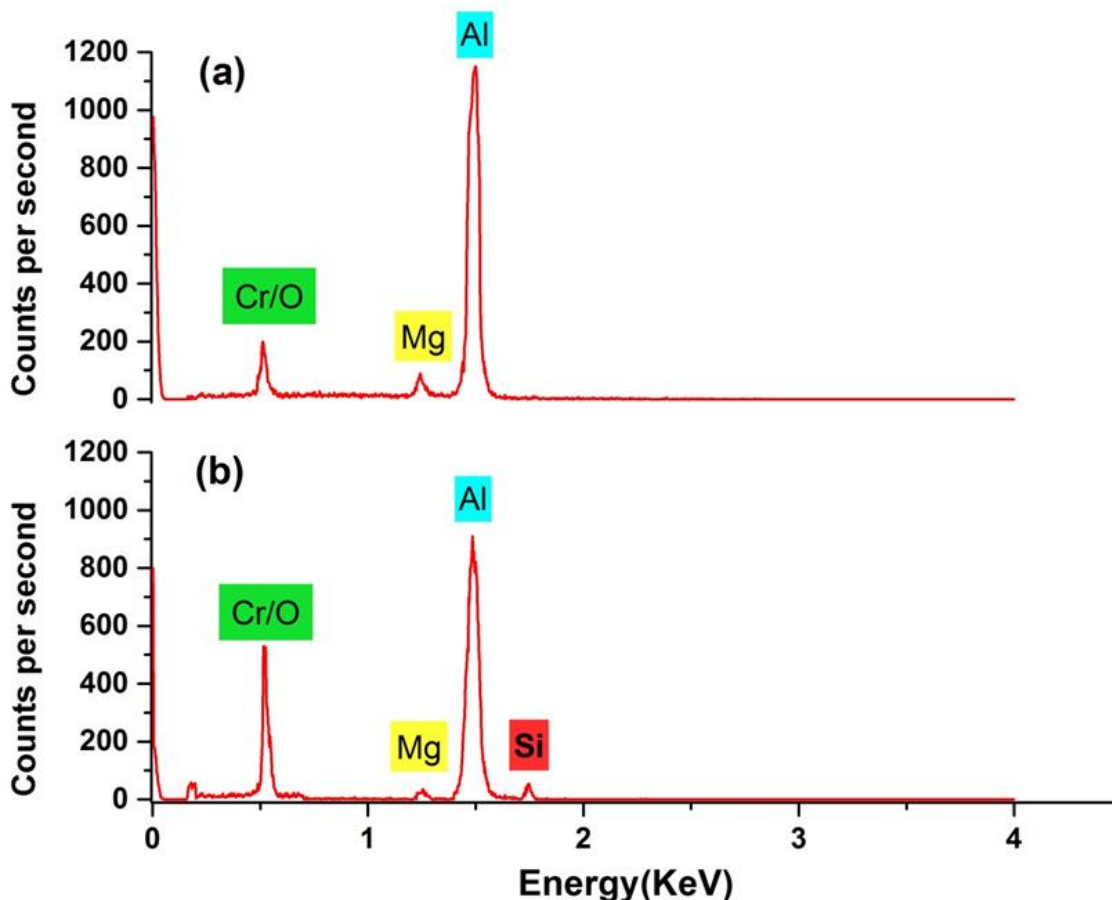


Figure 3.3. The EDX spectrum of (a) 7 min acid solution etched and (b) 7 min acid solution etched and chlorosilane modified specimens (S71).

In order to study the effect of different chlorosilane modifiers, the substrates with almost same surface roughness about $0.9 \pm 0.1 \mu\text{m}$ were modified by different chlorosilanes. As shown in Table 3.1, the S01 specimen which was modified with TCODS ($\text{CH}_3(\text{CH}_2)_{17}\text{SiCl}_3$ with linker length equal to 18) showed WCA equal to $133 \pm 2^\circ$, the S03 specimen which was modified with TCDS ($\text{CH}_3(\text{CH}_2)_{11}\text{SiCl}_3$ with linker length equal to 12) showed WCA equal to $130 \pm 2^\circ$, and the S04 specimen which was modified with TCOS ($\text{CH}_3(\text{CH}_2)_7\text{SiCl}_3$ with linker length equal to 8) showed WCA equal to $125 \pm 2^\circ$. As far as all the S01, S03, and S04 specimens' surface morphologies and

roughness were close together, the differences in their WCA gives us a reliable criterion for comparison of different chlorosilanes. Although it can be concluded that the specimens which were modified with the chlorosilanes that had higher linker length showed better hydrophobicity, none of the above specimens became super-hydrophobic; which shows that the aluminium alloy surfaces were not sufficiently roughened. The results confirm that the chlorosilane that has higher linker length produce better hydrophobic surfaces. The S71 specimen which is modified by TCODS that had linker length equal to 18 depicted the best super-hydrophobicity properties with WCA equal to $165 \pm 2^\circ$ and CAH less than 3° (Figure S3.3).

Generally, the S7x specimens which were acid solution etched for 7 min exhibited higher WCA and lower CAH than S5x specimens which were acid solution etched for 5 min. The effects of increasing in surface roughness by acid solution etching time in super-hydrophobicity properties was investigated by comparing S52 and S71 specimens. The only difference between preparing procedure of S52 and S71 specimens was the acid etching time, which increased the surface roughness of the specimen from $3.5 \pm 0.1 \mu\text{m}$ (S52 specimen) to $5.4 \pm 0.1 \mu\text{m}$ (S71 specimen) and the WCA from $158 \pm 2^\circ$ to $165 \pm 2^\circ$, respectively.

The roughening effect on the roughness and the WCA was investigated by comparing S51 and S52 specimens. Comparing S51 and S52 specimens shows that roughening by abrasive paper enhanced the WCA from $154 \pm 2^\circ$ to $158 \pm 2^\circ$ and also reduced the CAH by about 1° . The results make clear that roughening the surface improve the hydrophobic properties of the final aluminium surfaces. The 1 M NaOH treatment effects on the roughness and subsequently WCA were also investigated by comparing S72 and S73

specimens. Comparing S72 and S73 specimens showed that 1 M NaOH treating enhanced the surface roughness for about $1.8\ \mu\text{m}$ and the mean value of WCA for approximately 3° and reduced the CAH for about 1° , which represent an improvement in super-hydrophobic properties. Therefore, roughening, NaOH treatment, and acid etching not only increased the surface roughness, but also improved the final hydrophobicity properties on the resulting aluminium surfaces.

In order to investigate the effect of modifier amount on final super-hydrophobicity properties of aluminium surfaces, different volume of TCODS was added to Hexane. Specimens S75, S71, S76, S77, and S78 were modified by adding 2, 3, 4, 5, and 6 mL TCODS to 50 mL hexane, respectively. It can be concluded from Table 3.1 that increasing the modifier amount would leads to increase in final hydrophobicity properties, but if the amount of modifier increases more than 3 mL the improvement in hydrophobicity is not noticeable (Figure S3.4).

Figure 3.4 and Figure 3.5 show the dynamic droplet/surface interaction and the rolling droplet on the surface of S71 specimen which is tilted about 2.65° (CAH = 2.65°) on the surface of S71 specimen. In Figure 3.5 each consecutive image (a–f) was taken at 50 milliseconds interval.

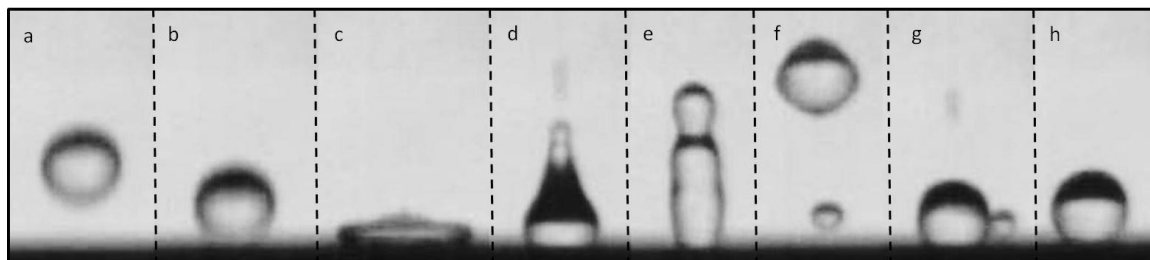


Figure 3.4. Dynamic droplet/surface interaction on the surface of S71 specimen. Time between frames is about 25 milliseconds.

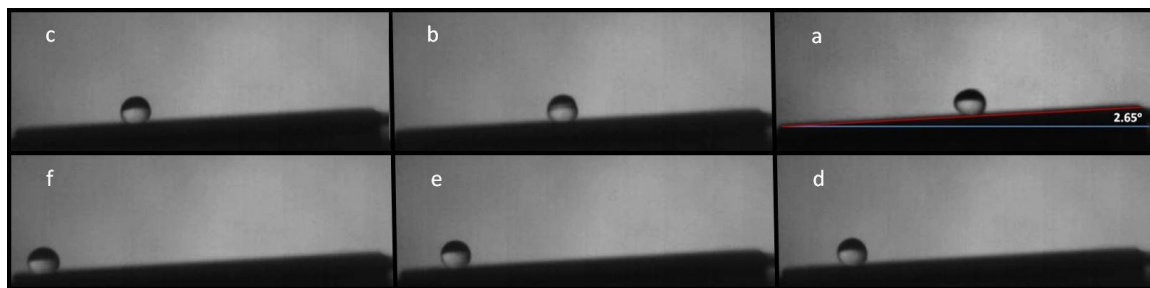


Figure 3.5. The rolling droplet on the surface of S71 specimen which is tilted 2.65° . Each consecutive image (a–f) was taken at 50 milliseconds interval.

3.4.3 The physical and thermal stability and storability of Super-hydrophobic aluminium surfaces

The physical and thermal stability and storability are some of the most important factors in testing and applying the super-hydrophobic substrates in industry. It was observed that some super-hydrophobic surfaces lost their properties completely or showed great difference in their surface WCA by immersing in water. Furthermore, in some cases that super-hydrophobic properties applied on a surface by coating, the coating became loose and could be rubbed off easily. Moreover, hydrophobic surface with a long persistence is another important issue for making the super-hydrophobic surfaces storable. In this work instead of using a super-hydrophobic coating, the aluminium alloy surfaces were modified directly after acid etching, so a strong Al-O-Si bond formed between aluminium surface and silane which produced durable and long lasting super-hydrophobic surfaces.

One of the drawbacks for industrializing super-hydrophobic surfaces is their lack of physical stability. Conventional super-hydrophobic coatings lose their properties by immersing them in water for a short time due to their weak adhesion to surfaces. Furthermore, the water molecules penetrate into the surface cavities during the immersion

time and it might weaken or even ruined the hydrophobic properties of the surfaces. Therefore, stability of the super-hydrophobic surfaces not only attribute to the period that they do not get fully wetted, but also to the ability of the surfaces to refined their super-hydrophobic properties after immersion in water. The stability of S71, S73, and S74 specimens were tested by immersing them in water for 2 hours and also the long term stability of the S71 specimen was investigated after immersing in water for 100 hours. Despite the fact that all specimens showed a decrease of about 4° in WCA when they were immersed in water for 2 hours, comparing to the none-immersed specimens, all of them remained super-hydrophobic (Figure S3.5). The WCA were similar and almost constant at several points across the surface of all the specimens. Moreover, the S71 specimen was immersed in the water after 100 hours. The WCA of S71 specimen that was immersed in water for 25, 50, 75, and 100 hours, were $158 \pm 2^\circ$, $155 \pm 2^\circ$, $152 \pm 3^\circ$, and $150 \pm 4^\circ$, respectively. The WCAs were measured after letting the surfaces dry at ambient air for 30 min. A large number of small and some bigger air bubbles formed over the S71 specimen's surface when it initially immersed in water. It was observed that the smaller air bubbles left the surface during the first 24 hours of the surface immersion. However, a little number of the bigger air bubbles stuck to the surface even after 24 hours (Figure S3.6). It was observed that heat treatment after surface modification increases the hydrophobicity stability of the specimens. The specimens that were not heat treated lost their hydrophobicity after 2 hours of immersion in water.

As far as super-hydrophobicity associates with surface roughness, water molecules penetrate through the cavities and could ruin the surface hydrophobicity by eliminating air trapping zones. In this case, an 8 μ L droplet was used to see the change in WCA on

the surface of the S71, S73, and S74. The 8 μL droplet was placed on the mentioned specimens and the WCA was measured after 5, 10, 20, and 25 min. The droplet volume was decrease due to evaporation. Evaporation occurred faster at the air/water interface, therefore the contact angle get smaller with passing of time. The results are shown Figure 3.6.

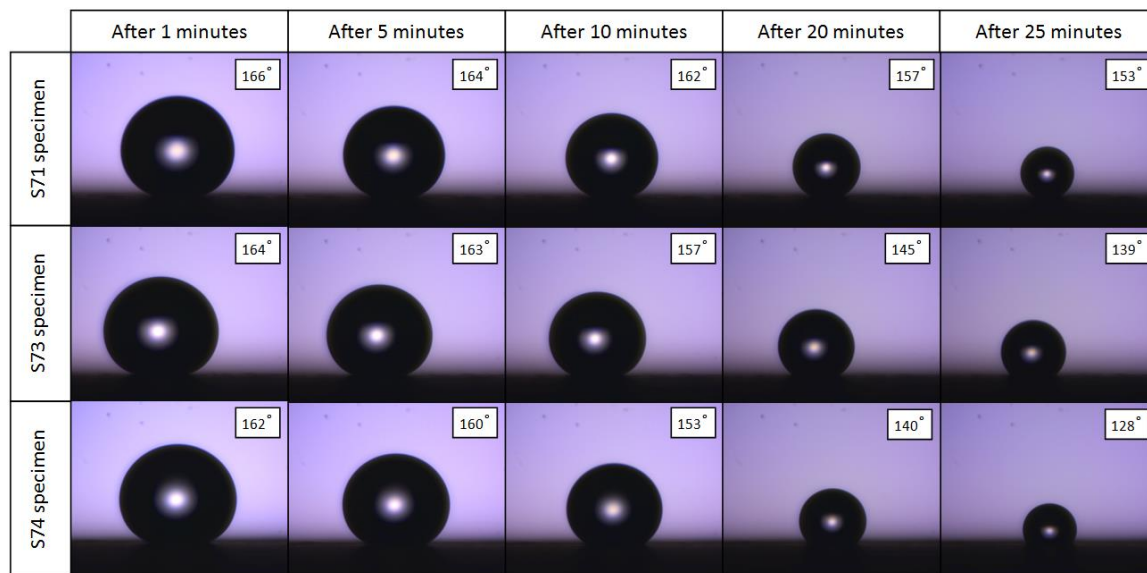


Figure 3.6. The WCA of 8 μL droplet on the surface of the S71, S73, and S74 after 5, 10, 20, and 25 minutes. The size of the water droplets reduced successively due to evaporation.

Besides, for investigating the quality of physical connection between the silane group and the aluminium substrate, The S71 specimen was placed in an ultrasonic water bath for 70 min. The S71 specimen remained super-hydrophobic after 30 min staying in ultrasonic water bath that shows its superb physical stability. The results are shown in Figure 3.7.

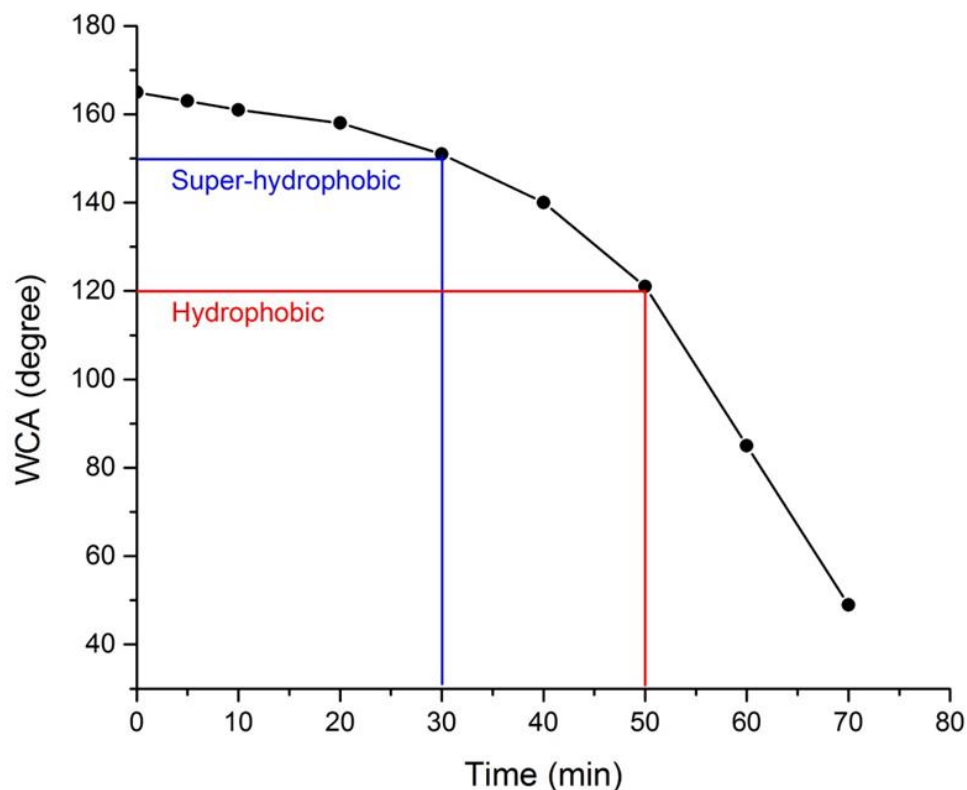


Figure 3.7. The WCA of S71 specimen putted in ultrasonic water bath for 5 to 70 minutes.

Storability is another important issue for industrializing the super-hydrophobic surfaces. The surfaces should maintain their properties while they were stored for a long time. In order to investigate the storability of the super-hydrophobic surfaces, the WCA of the S71, S73, and S74 specimens were measured after 10, 20, and 30 days of storing in ambient air. The results are presented in Table 3.2. All of the specimens showed good stability during one month study as indicated by the fact that the WCA did not significantly change. Moreover, S71 specimen remained super-hydrophobic with WCA equal to $162 \pm 2^\circ$ even after 180 days. It can thus be concluded that the modified substrates with chlorosilanes exhibited remarkable under water durability, they remained

super-hydrophobic, and their WCA were also quite uniform with nearly the same WCAs across the entire specimens' surface.

Table 3.2. The average WCA of (a) S71, (b) S73, and (c) S74 specimens after 1, 10, 20, 30, and 180 days of storing at ambient air.

Specimen	WCA on 1 st day (°)	WCA after 10 days (°)	WCA after 20 days (°)	WCA after 30 days (°)	WCA after 180 days (°)
S71	165 ± 2	164 ± 2	164 ± 2	163 ± 2	162 ± 2
S73	163 ± 2	163 ± 2	162 ± 2	161 ± 2	–
S74	159 ± 2	160 ± 2	158 ± 2	157 ± 2	–

The last but not the least, thermal stability of the super-hydrophobic surfaces is another important issue in high temperature industries. To evaluate thermal stability of our super-hydrophobic surfaces WCA of S71 specimen was investigated after its exposure to high temperature condition. The WCA of S71 specimen held at elevated temperatures under ambient condition is shown in Figure 3.8. The S71 specimen showed good thermal stability with WCA of > 150° up to 380 °C and WCA of > 120° up to 425 °C. The WCA began to decrease rapidly from 400 °C, which we attribute to the thermal decomposition of the modifiers (chlorosilane).

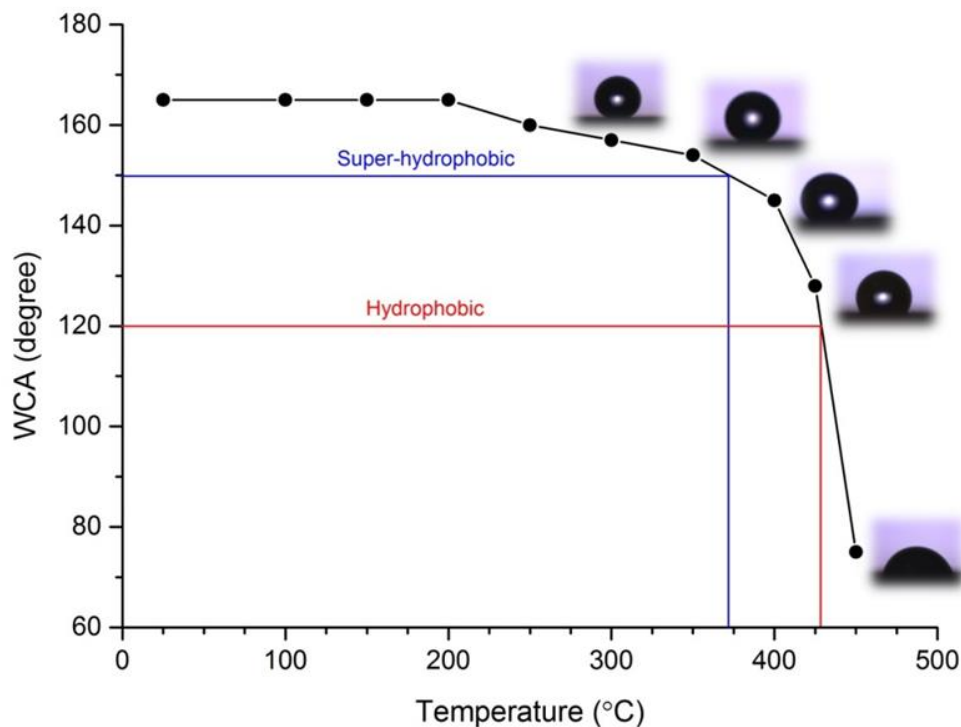


Figure 3.8. The WCA of S71 specimen held at different temperatures. The insets show the water droplets on the surfaces after heating at different temperatures for 20 minutes.

3.5 Conclusions

We have successfully created long-lasting, thermally stable and storable super-hydrophobic aluminium alloy surfaces by a practical, easy, and inexpensive approach which was a combination of chemical etching followed by surface silanization. The final aluminium alloy surfaces showed outstanding super-hydrophobicity with a water contact angle of around $165 \pm 2^\circ$ and a contact angle hysteresis of less than 3° . The aluminium alloy surfaces preserved their super-hydrophobicity when heated up to 375°C , putted in ultrasonic water bath for 30 min, after immersing in water for 100 hours, and storing for 180 days.

3.6 Supporting Information

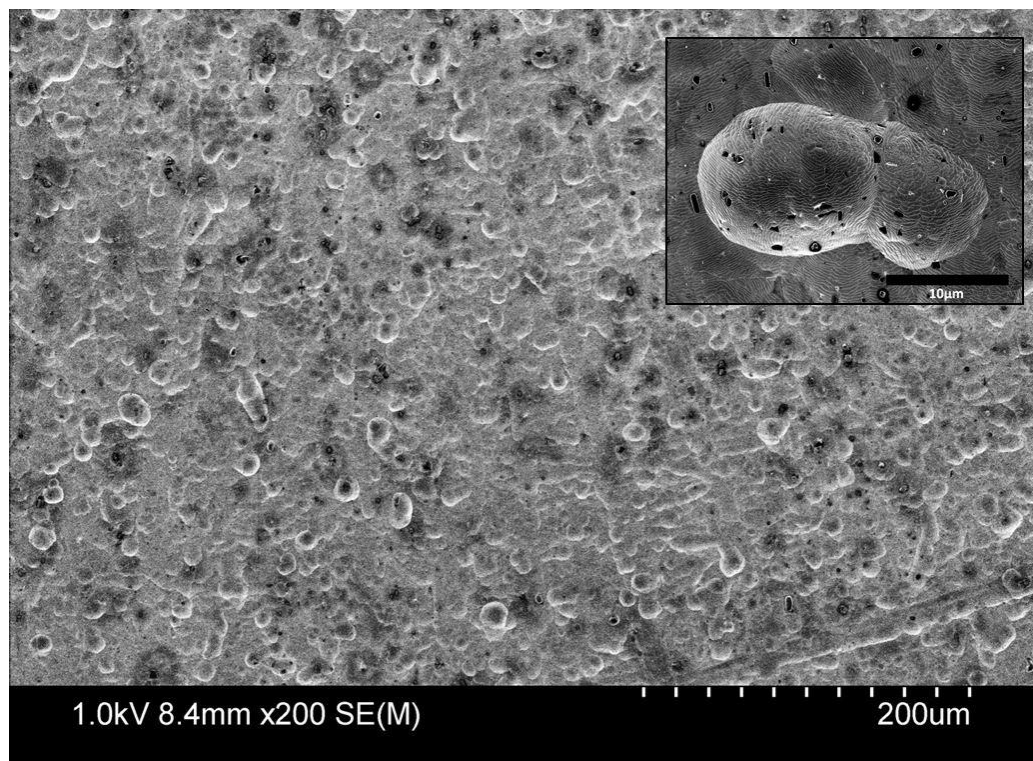


Figure S3.1. SEM image of 1 M NaOH treated aluminium alloy surface for 10 minutes that creates cone-like structure over the aluminium surface. The inset shows a closer look of a typically treated aluminium alloy surface.

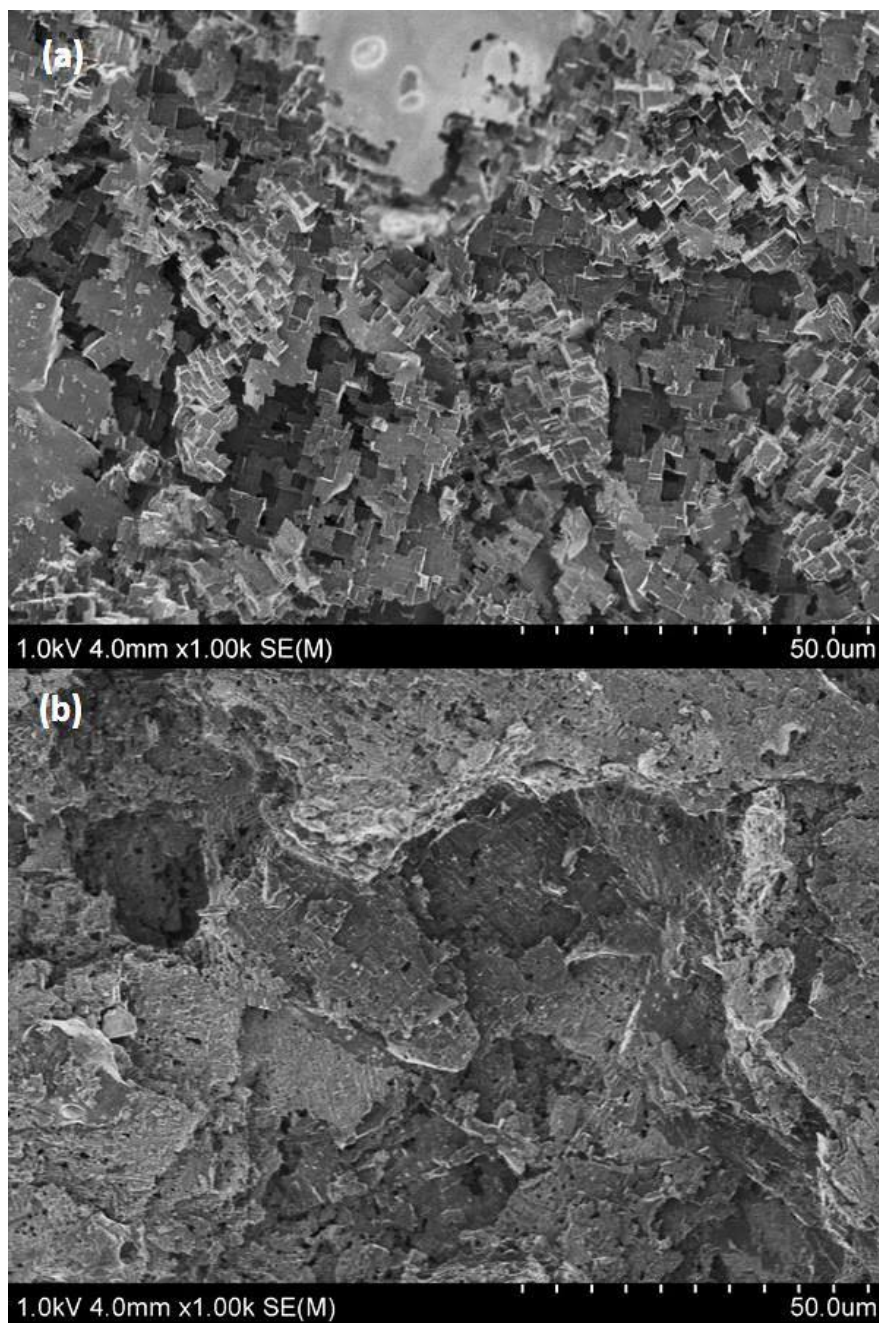


Figure S3.2. SEM images of the aluminium alloy surfaces etched for (a) 3 min and (b) 9 min in acid solution with volume ratio of $V_{\text{H}_2\text{O}} : V_{\text{HCl}} : V_{\text{CH}_3\text{COOH}} = 20 : 8 : 1$.

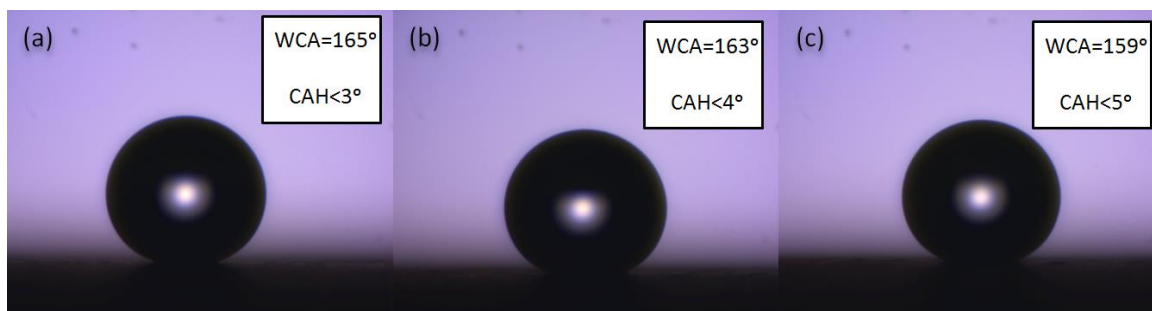


Figure S3.3. The WCA and CAH of (a) S71, (b) S73, and (c) S74 specimens.

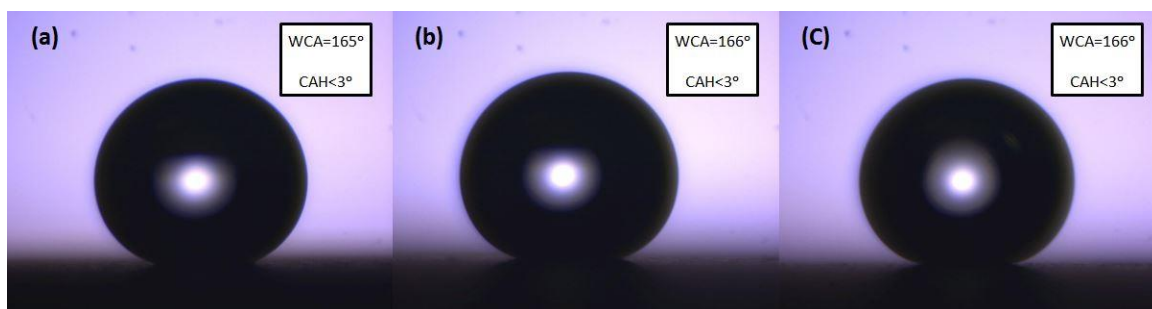


Figure S3.4. The WCA and CAH of (a) S76, (b) S77, and (c) S78 specimens.

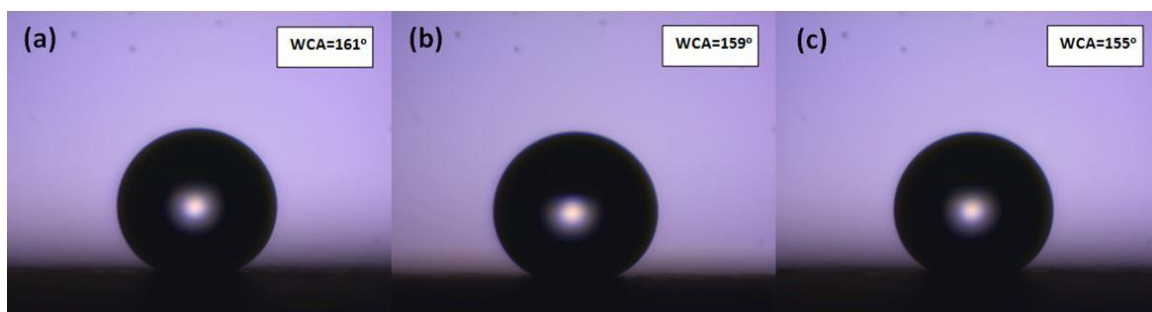


Figure S3.5. The WCA of (a) S71, (b) S73, and (c) S74 specimens after immersing in water for 2 hours.

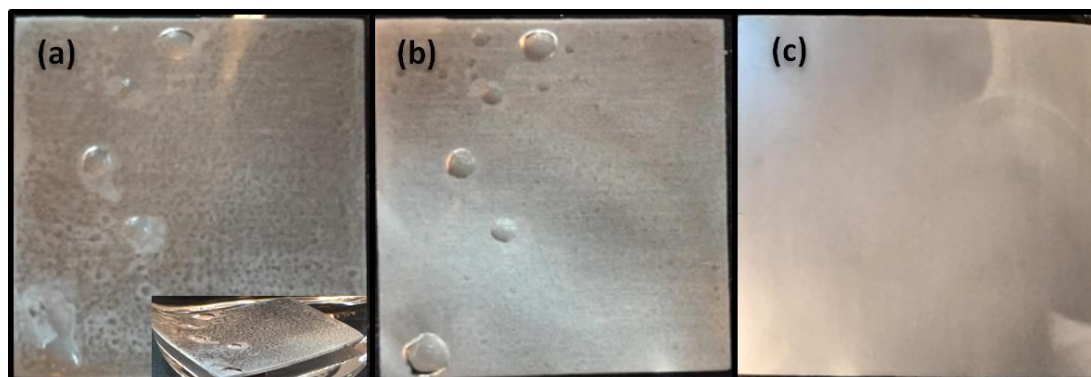


Figure S3.6. Retention of air bubbles on the Super-hydrophobic aluminium alloy surface after immersion in D.I. water for (a) 5 minutes, (b) 24 hours, and (c) 48 hours.

3.7 Acknowledgement

The authors acknowledge financial support of Natural Sciences and Engineering Research Council (NSERC) of Canada and Korea Institute of Machinery and Materials (KIMM) for the work of this paper. The authors would also like to acknowledge the help and support of the staffs of the advanced microscopy facility at University of Victoria.

3.8 Graphical abstract

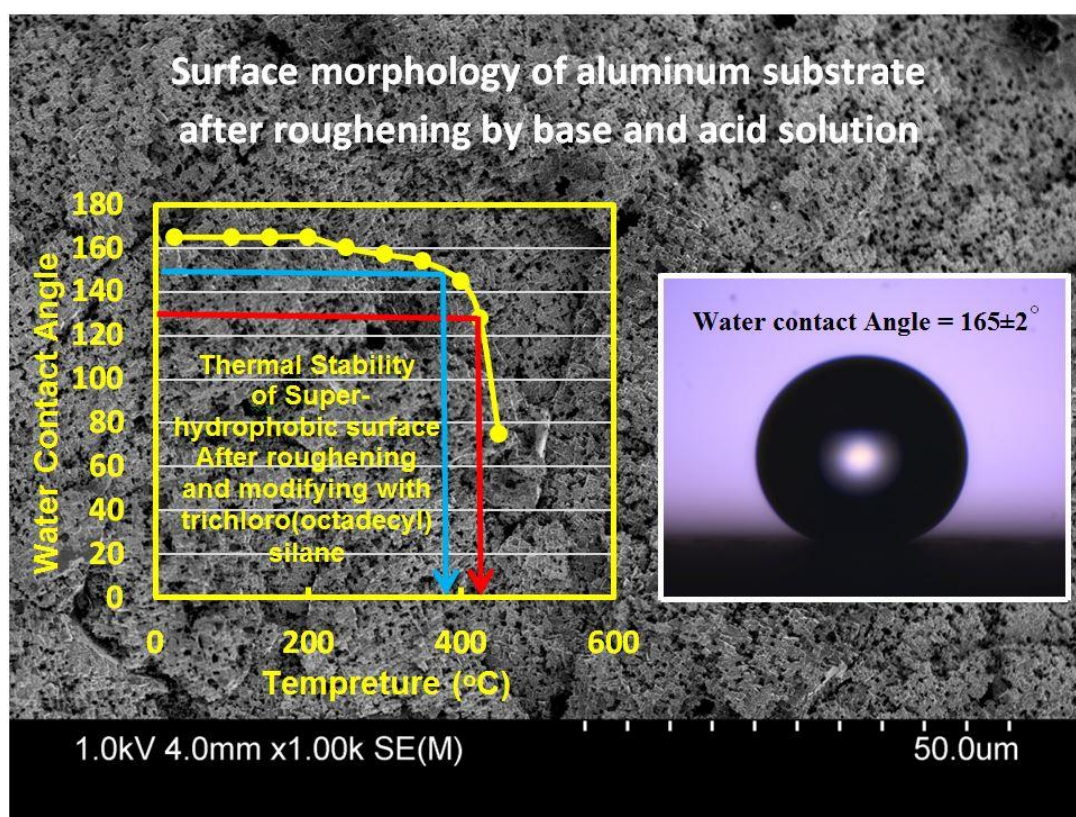


Figure 3.9. Graphical abstract of the article paper entitled “A Cost-effective Method to Create Physically and Thermally Stable and Storable Super-hydrophobic Aluminium Alloy Surfaces”.

Chapter 4 Hydrothermal Deposition of Robust Cerium Oxide Based Superhydrophobic and Corrosion Resistive Coatings on Aluminium Alloy Substrates

This paper has been submitted to the Journal of ACS Applied Materials and Interfaces.

Ahmad Esmaeilirad, Mahdieh Atighilorestani, Vahid Ahsani[†], Martin B.G. Jun, Frank C. J. M van Veggel. “Hydrothermal Deposition of Robust Cerium Oxide Based Superhydrophobic and Corrosion Resistive Coatings on Aluminium Alloy Substrates.” Submitted to Journal of ACS Applied Materials and Interfaces (2017).

4.1 Abstract

Developing durable superhydrophobic coating with corrosion protection capability for aluminium alloys has been gaining more and more attention due to their various applications. A facile and highly controllable fabrication method, consisting of a hydrothermal deposition and further surface assembly of low-surface-energy compound, was employed to fabricate corrosion resistance superhydrophobic coatings. The water repellency of the coatings is obtained by cerium oxide hierarchically microtextured surface features accompanied by further surface treatment with trichloro(octyl)silane as a low-surface-energy compound. Both sample positioning and hydrothermal processing conditions were shown to play critical roles in resultant coating surface microstructural texture, hydrophobicity, and consequently corrosion protection performance. By controlling the hydrothermal coating processing conditions, a uniform microtextured coating was grown over T6-6061 aluminium alloy, which showed a water contact angle

of ca. $170 \pm 2^\circ$ and a rolling angle of ca. $2.4 \pm 0.2^\circ$ after surface modification. The fabricated superhydrophobic coating exhibited excellent wear resistance by maintaining its superhydrophobicity after abrasion against #800 SiC abrasive paper under pressures up to 3.92 kPa. The coatings also showed considerable chemical stability by preserving its superhydrophobicity in acidic and alkaline conditions over pH range of 2–13, as well as, 50 h immersion in corrosive 3.5 wt % NaCl aqueous solution. The corrosion resistance served by synergetic effects of protective cerium oxide layer and its superhydrophobicity on aluminium alloy was estimated by potentiodynamic polarization measurements. The results revealed that the superhydrophobic coating has excellent corrosion resistance by decreasing the corrosion rate of approximately three-orders of magnitude. It is believed that this method can be utilized to develop robust superhydrophobic corrosion protective coatings on various metallic substrates.

4.2 Introduction

Metals and their alloys, as the most applied materials in a variety of engineering and manufacturing applications, are not thermodynamically stable in presence of oxygen and under moist conditions, and gradually corrode to their more stable components, such as oxides and/or hydroxides. Therefore, developing a suitable corrosion protection strategy is an inevitable step for extending metal and metal alloys' life-time and practical applications.¹ The cost of corrosion and corrosion protection is estimated to be more than several billion dollars even for small countries; hence, promoting a durable, low cost, and effective corrosion protective surface treatment is of great importance.²

Several strategies, including cathodic protection,¹⁴³ anodizing,¹⁴⁴ and coating with anti-corrosion⁸ and non-wetting materials,⁸² individually or in combination, have been

employed to preserve metal surfaces from natural degradation. Chemical conversion coatings, which were usually based on chromate ions, had been used for decades to improve corrosion resistivity of metal surfaces.¹⁷ However, using chromium compounds as corrosion inhibitors are being prohibited due to their high toxicity and carcinogenic nature.¹⁴⁵ Among various ceramic and metal coatings, which have been employed to produce chromate free corrosion protection, rare earth based oxides and hydroxides have shown a promising improvement in controlling the metals and metals' alloys corrosion by acting as cathodic inhibitors.²³ With the exception of Ce and La, the other rare earth elements are not considered as commercial corrosion inhibitors due to their high cost.⁹⁷ Cerium and cerium based oxides are known to perform the best corrosion protection among rare earth elements (e.g. Sm, Nd, Pr, Y, and La) and show superior adhesion to metal surfaces.^{97, 146}

Cerium is the most abundant rare earth element (0.0046 wt % of earth crust) and cerium(IV) oxide, also known as ceria, is the most common compound of cerium.¹⁴⁷⁻¹⁴⁸ Cerium and cerium based oxides have shown promising improvements in metals corrosion inhibition, including aluminium,³⁵ stainless steel,²² magnesium,⁸² and copper.¹⁴⁹ In addition to cerium oxide corrosion inhibition, it is recently reported that some of the rare earth oxides (REOs), including cerium oxide, are intrinsically hydrophobic, which can potentially improve corrosion protection acquired by them.^{52, 100} The hydrophobicity of REOs is imputed to their unique electronic structure, which restrains hydrogen bonding with water molecules.^{100, 150} However, the reported CeO₂ water contact angles are not consistent,^{93, 116} which is attributed to delicate relation between the CeO₂ surface layer chemistry and its interaction with water molecules.¹⁵¹⁻¹⁵²

Cerium oxide becomes hydrophilic by any deviation in its interfacial atomic and electronic structure, such as presence of oxygen vacancies and surface hydration.^{104, 116,}

¹⁵³ Hence, cerium oxide surface assembly with a low-surface-energy material is ineluctable for developing durable non-wetting surfaces to perform in harsh environment.

Non-wetting surfaces with a static water contact angle greater than 150° and sliding angle less than 10° are called superhydrophobic.⁴ The concept of superhydrophobicity is embraced from natural non-wetting surfaces such as the Lotus leaf, *Nelumbo nucifera*, and is attributed to the hierarchically microtextured non-polar surfaces.^{11, 61} The surface microtexture is crucial for creating superhydrophobic surfaces by developing air trapping zone between its interfacial texture (Cassie-Baxter mode), resulting into a composite solid-air interface, and consequently enhancing hydrophobic properties of surfaces.^{59, 70} Improving facial water repellency restrains water molecules interfacial interaction, and consequently improves metals corrosion resistivity.^{42, 154} Besides, superhydrophobic metal surfaces are attracted significant attention for a broad range of applications due to their remarkable friction drag reduction,⁴³ anti-contamination,⁴ self-cleaning,²⁵ and anti-icing properties.⁴⁵ However, the wettability of the superhydrophobic surfaces is susceptible to degradation in harsh environments.^{84, 155} Despite all progresses in fabricating durable superhydrophobic coatings, developing water-repellant surfaces, which are robust to mechanical wear and surface chemical degradation, is still the main concern for their practical applications.^{26, 156}

Various aqueous-based techniques, including sol-gel template processes,¹⁰⁹ precipitation,¹¹⁰ microemulsion,¹⁵⁷ and surfactant-assisted/free hydrothermal process^{32, 111} have been reported for ceria nanoparticles synthesis in different shapes. Geometrical

designing and morphology control of nanostructures have been of great interest for bottom-up fabrication.¹⁰⁷⁻¹⁰⁸ Among different cerium oxide synthesis processes, hydrothermal method is known as an effective template-free technique for shape-controlled synthesis of cerium oxide nanoparticles.^{35, 107} Therefore, the hydrothermal coating process would be an appropriate method to construct microstructural surfaces, which is of significant importance for developing non-wetting metal surfaces.⁵⁸ However, just a few studies have been conducted to grow well-defined textural coatings on metal substrates based on hydrothermal deposition.^{34-35, 82}

Hydrothermal process is based on materials crystallization from high temperature aqueous solution at high vapor pressures and is known as one of the versatile methods for fabricating shape controlled nanoparticles.^{154, 158} Different types of Ce^{3+} and Ce^{4+} salts have been utilized as CeO_2 sources in hydrothermal process including cerium(III) nitrate, cerium(III) chloride, and cerium(IV) sulfate.¹⁰⁷ The size and morphology of the resultant ceria particles are directly related to the type and concentration of cerium salt. It has been shown that shape and structure of ceria particles are more controllable using Ce^{3+} salts.^{33, 112} Moreover, the presence of anions such as Cl^- , Br^- , and I^- in acidic condition leads to rod-like CeO_2 formation. In contrast, alkaline solutions and oxidizing anions, such as NO_3^- , result in gradually conversion of ceria nanorods to nanocubes.^{111, 159} In case of cerium(III) precursor, intermediate phases such as cerium hydroxide or cerium hydroxycarbonate are formed during the hydrothermal process. Therefore, an oxidation step is required to convert the Ce^{3+} intermediate phases to CeO_2 , which does not result in any change in shape of the particles.^{107, 160} The substrates should be placed inside an aqueous solution consisting of cerium salts and mineralizer for hydrothermal deposition

of ceria. However, metallic substrates deteriorate in the presence of aggressive anions (e.g. Cl^- ions) and in highly acidic environments, which delirious effect can be intensified by the high temperature hydrothermal processing conditions.³

In the present work, a robust microtextured superhydrophobic cerium oxide coating is grown on T6-6061 multipurpose Aluminium Alloy (T6-6061 AA). A controlled hydrothermal process of highly concentrated $\text{Ce}(\text{NO}_3)_3$ and urea aqueous solution was employed for cerium hydroxycarbonate deposition, which was transformed to CeO_2 by heat treatment, followed by modification with a self-assembled layer of trichloro(octyl)silane (TCOS) to generate superhydrophobic properties. To the best of our knowledge, it is the first systematically investigation on the hydrothermal processing conditions, such as sample locating, heating rate, and pressure effects on cerium oxide coatings surface microtexture, chemistry, and wettability on aluminium alloy surfaces. The formation mechanism of cerium hydroxycarbonate and its conversion to cerium oxide are also discussed. Moreover, the stability and durability of the superhydrophobic surfaces were investigated by exposure to various harsh environments such as abrasion and NaCl corrosive media. The corrosion protection performance of the samples was also approximated by potentiodynamic polarization measurement.

4.3 Experimental Section

4.3.1 Materials and method

The structural cerium based oxide coatings were grown on 0.062 inch thick, 1 inch by 1 inch aluminium alloy (AA) substrates (mirror-like T6-6061 aluminium alloy, McMaster Carr), which were cut from larger sheets. The AA substrates were first ultrasonically degreased in anhydrous ethanol for 10 min and then in acetone for extra 10 min; and

finally rinsed with deionized water for several times (purity of $> 18.2 \text{ M}\Omega$). An ultrasonic water bath (Branson 3510R-MTH) with a frequency of 42 kHz and maximum draw power of 100 W was used for cleaning the T6-6061 AA substrates. The cleaned AA surfaces were dried in air at 100°C for 15 min prior to hydrothermal deposition process.

Microstructural cerium hydroxycarbonate coatings were hydrothermally deposited on 6061 AA surface (Table 4.1). In general, 50 mL to 125 mL of a solution of 1 M cerium nitrate hexahydrate ($\text{Ce}(\text{NO}_3)_3 \cdot 6\text{H}_2\text{O}$ 99 %, Sigma Aldrich) and 3 M Urea ($\text{CO}(\text{NH}_2)_2$ 98 %, Sigma Aldrich) in deionized water, which were stirred for 30 min, were introduced to a 175 mL Teflon-lined stainless steel autoclave. The autoclave is equipped with a pressure gage and a K-type thermocouple measuring the autoclave pressure and the solution temperature, respectively. The cleaned aluminium alloy surfaces were horizontally placed at 2 cm from the bottom of the autoclave. As it is shown in Table 4.1, hydrothermal deposition process was carried out between 130°C and 170°C at 10°C intervals by heating rate of 0.5, 1 and $2^\circ\text{C}/\text{min}$, using a heating mantle (OF-36227-14 Col-Parmer). The autoclave was immediately cooled down in a water bath, once the deposition was completed. The coated T6-6061 AA surfaces were thoroughly washed by deionized water and dried for 30 min at 100°C .

Table 4.1. Hydrothermal processing conditions utilized for S1 to S10 coating deposition.

Hydrothermal condition	Sample Name	Solution Amount (mL)	Processing Temperature(°C)	Heating rate (°C/min)	Final Processing Pressure (psi)
# 1	S1	50	150	1	~60
# 2	S2	75	150	1	~90
# 3	S3	100	150	1	~150
# 4	S4	125	150	1	~200
# 5	S5	75	130	1	~20
# 6	S6	75	140	1	~60
# 7	S7	75	160	1	~140
# 8	S8	75	170	1	~200
# 9	S9	75	150	2	~90
# 10	S10	75	150	0.5	~90

Cerium hydroxycarbonate phase transformation to cerium oxide was carried out by heating up the coatings to 250 °C with heating rate of 1 °C/min under air flow and curing for 2 h using a programmable Lingburg Blue tube furnace. Subsequently, the heat-treated aluminium surfaces were immersed in a mixture of 18 mL hexane (C₆H₁₄ ACS reagent, ≥ 98.5 %, Sigma Aldrich) and 2 mL trichloro(octyl)silane (TCOS) (CH₃(CH₂)₇SiCl₃ 97 %, Sigma Aldrich) for 2 min and thoroughly washed with hexane to remove non-bonded silanes from the surface. Finally, the coated and modified T6-6061 AA substrates were cured at 100 °C for 2 h in air.

4.3.2 Characterization

The surface morphology of the substrates was studied using a field emission scanning electron microscope (FE-SEM Hitachi S-4800). The surface 3D profile and roughness of

the coatings were characterized with a 3D non-contact optical profiler (Zeta Instruments, USA). The crystal phase analysis of the coatings was performed using a PANalytical Empyrean X-ray diffractometer with CuK α X-ray source (see Supporting Information). The X-ray diffractometer was equipped with a HTK 1200N oven, which was utilized for non-ambient crystal phase analysis in different temperatures. The surface chemical composition and chemistry of the samples were investigated using Omicron & Leybold MAX200 X-ray photo-electron spectrometer (XPS) and PerkinElmer attenuated total reflectance fourier transform infrared spectrometer (ATR-FTIR). The wettability of the surfaces was evaluated by water contact angle and rolling angle measurements (HO-IAD-CAM-01B Holmarc, Germany) with an approximately 5 μ L droplet under ambient temperature and pressure. The measurements repeated on at least five different places on the sample surface and the average with standard deviation is reported. The high speed videos and images of rolling angle and dynamic droplet/surface interaction were recorded by a Photron APX-RS FASTCAM at a rate of 1000 frames per second.

The abrasion resistance of the superhydrophobic coatings was evaluated by a scratch test, in which the coated surface were faced to a #800 grit SiC abrasive paper and moved for varying distances under 0.98 kPa to 4.90 kPa applied pressure. The wettability of the coatings was evaluated as a function of droplet pH value ranging between 2 to 13 under ambient condition. The salt water stability of the non-wetting surfaces was studied upon immersing the samples into 3.5 % NaCl aqueous solution for 50 h. The stability of the superhydrophobic surfaces was rated by storing the substrates under ambient condition for more than three months and measuring their water contact angle (WCA) at 10 days intervals.

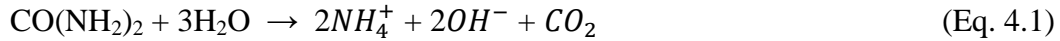
The electrochemical corrosion measurements were carried out in a custom-made three electrode cell, including a working electrode (WE), a counter electrode (CE), and a reference electrode (RE) at room temperature. 1 cm² of the as-prepared samples as WE and 3 cm² of a Graphite sheet as CE were exposed to 3.5 % NaCl solution as corrosive media. The distance between WE and CE was set to 10 cm (Figure S4.1). A homemade Ag/AgCl reference electrode was placed at 0.3 cm from the WE (Figure S4.2). The constant potential of the reference electrode was confirmed by comparing it with a standard hydrogen electrode prior to electrochemical measurements. All samples were exposed to the corrosive media for 1 h before potentiodynamic polarization. The potentials were scanned at rate of 0.3 mV·s⁻¹ from -250 mV to 250 mV, with respect to open circuit potential of the samples, while the according currents were recorded. The corrosion current, corrosion potential, and corrosion rate (CR) were extracted from Tafel plot extrapolation.

4.4 Results and Discussion

Cerium hydroxycarbonate coating with orthorhombic crystal structure and well-defined microfeatured surface layer were grown on T6-6061 AA substrate through a hydrothermal process. Cubic cerium oxide was attained by a phase transformation from cerium hydroxycarbonate during the heat-treatment. Corrosion resistivity of the cerium based coatings was remarkably enhanced upon introducing the non-wetting properties of the coatings, which were rendered by TCOS surface treatment over artificial microfeatured cerium oxide coatings.

4.4.1 Chemical composition and surface chemistry

In hydrothermal synthesis process, formation of CeOHCO_3 nuclei starts from reaction between Ce^{3+} ions and the products of urea hydrolysis. Urea hydrolyses to NH_4^+ , OH^- , and CO_2 at temperatures above 60 °C as follows:¹⁶¹



And consequently, the formation of cerium hydroxycarbonate can be summarized as follows:¹⁶²

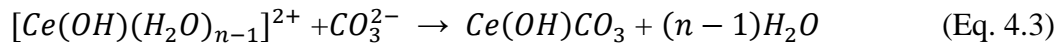
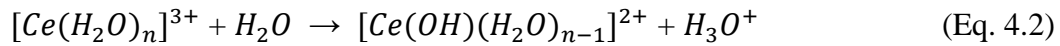
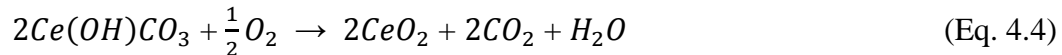


Figure 4.1a and Figure 4.1b show the surface XRD patterns of the bare T6-AA6061 and a hydrothermally coated substrate (Sample S2). The sharp characteristic peaks shown in the spectrum reveal that the hydrothermally deposited coating consists of highly crystalline orthorhombic CeOHCO_3 single phase. Presence of substrate Al characteristic peaks in XRD pattern can be attributed to high depth of X-ray penetration; while, there is no trace of Al on surface layer of the coating, which will be discussed later. Figure S4.3a shows that the XRD peaks of all the samples, which are in accordance with orthorhombic cerium hydroxycarbonate (JCPDS file No. 41-13).¹⁶³ Figure 4.1c shows the resultant cerium oxide coating formed through CeOHCO_3 heat-treatment at 250 °C under air flow, which can be summarized as follows:¹⁶⁴



All the diffraction peaks present at Figure 4.1c and Figure S4.3b, excluding substrate Al peaks, are well assigned to cubic CeO_2 with fluorite structure reported in JSPDS file No. 34-0394.⁹⁶ Figure 4.1d shows the non-ambient XRD patterns of as grown cerium

hydroxycarbonate coatings through heating up to 400 °C (see Supporting Information Figure S4.4 for non-ambient XRD heating profile). The formation of CeO₂ phase in coating initially appeared at around 180 °C and coexistence of CeO₂ and CeOHCO₃ phases continued up to 200 °C. The fluorite cerium oxide was found as the only phase presents in the coating which heat treated up to 225 °C. No phase change was observed upon further increase in heating temperatures up to 400 °C. However, the characteristic peaks' width contraction was observed by elevating processing temperature, which is attributed to increase in average crystallite size of the cerium oxide layer.

Figure S4.5 shows the non-ambient X-ray diffraction pattern of the deposited powder associated with experiment #2. The result shows that like the deposited coating, the powder was composed of CeOHCO₃ single phase, which is transformed to fluorite CeO₂ upon heat treatment. However, the phase transformation of the powder occurs at lower temperatures and single phase of CeO₂ powder forms at 200 °C.

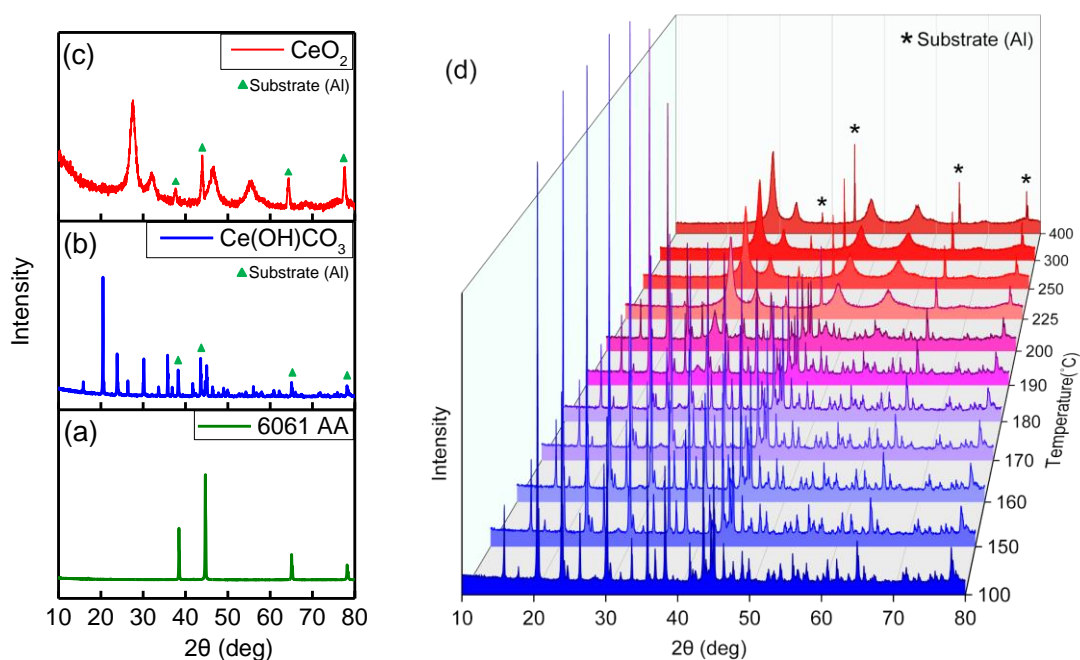


Figure 4.1. XRD patterns of (a) bare T6-6061 AA, (b) cerium hydroxycarbonate coating synthesized through hydrothermal process (Sample S2), (c) cerium oxide coating formed through heat-treatment at 250 °C. (d) The non-ambient XRD characteristic peaks of as deposited hydrothermal coating took at different temperatures in rang of 100 °C to 400 °C.

The surface chemistry of the coatings before and after modification with TCOS were investigated using attenuated total reflectance-Fourier transform infrared (ATR-FTIR) and X-ray photoelectron (XPS) spectroscopy. Infrared transmission spectrum of the as-prepared CeO_2 coating is shown in Figure 4.2a. The penetration depth of ATR-FTIR is typically between 0.5 μm to 2.0 μm .¹⁶⁵ The broad peak at 3275 cm^{-1} is attributed to the O–H stretching vibrations.¹⁶⁶ The peaks at 520 cm^{-1} and 841 cm^{-1} are produced by Ce–O stretching vibration.¹⁶⁶ The weak peaks at 2652, 2850 and 2922 cm^{-1} correspond to C–H stretching vibrations,¹⁶⁷ which are assigned to the absorbed atmospheric hydrocarbons. The peaks at 1060, 1330, 1450 and 1630 cm^{-1} are assigned to overlapped C–H and O–H

bending vibrations and C–O stretching vibrations,¹⁶⁸ which is attributed to surface adsorbed water molecules and carbonate. Figure 4.2b exhibits the FTIR spectrum of the (Figure 4.2) modified cerium oxide surface by TCOS. A broad band at 1000–1150 cm^{-1} appears in the modified surface spectrum, is ascribed to the Si–O–Si stretching vibrations.¹⁴⁹ Besides, the peaks at 2652, 2850 and 2922 cm^{-1} that are assigned to the C–H stretching vibration of the $-\text{CH}_2$ and $-\text{CH}_3$ groups¹⁶⁷ are remarkably more intense after surface modification due to TCOS aliphatic hydrocarbon chain. The results show that TCOS molecules have been successfully assembled on the cerium oxide coatings.

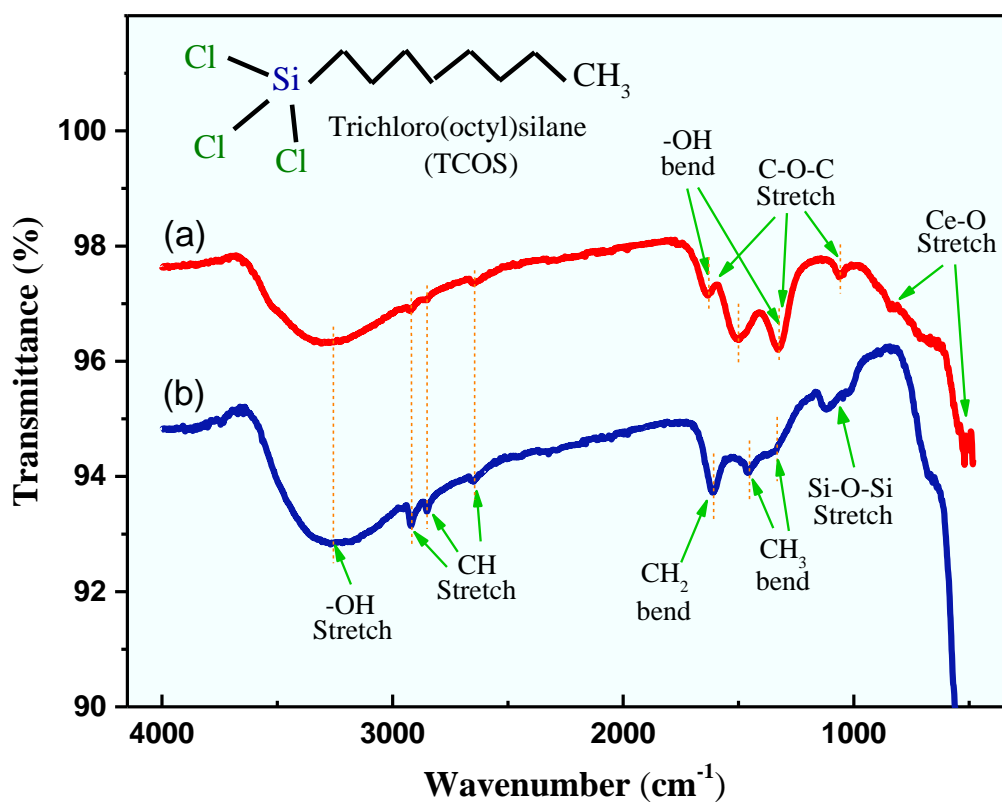


Figure 4.2. ATR-FTIR spectra of the CeO₂ surface (a) before and (b) after TCOS surface treatment.

To further investigate the surface chemistry of the coatings, Figure 4.3 and Figure 4.4 display the X-Ray Photoelectron (XPS) Spectra of the cerium oxide coatings before and after modification with TCOS. Figure 4.3(a) and Figure 4.3(b) show the survey spectra of the cerium oxide and modified cerium oxide coatings, respectively. Non-appearance of Al and its components in survey scans reveals the full coverage of the AA substrate by the coatings. From the survey spectra, the oxygen and carbon elements that are detected on as-prepared CeO₂ coating (Figure 4.3(a)), are ascribed to the surface oxide film and atmospheric contaminations. The peaks of Si 2s, Si 2p, and Cl 2p are observed in the survey spectrum of TCOS modified surface, which is shown in Figure 4.3. The very tiny peak of chlorine can be attributed to the contaminated chlorides, while the initiate of Si element confirms the presence of TCOS molecules on the surface. Figure 4.3(c) and Figure 4.3(d) exhibit the high-resolution XPS spectra for cerium oxide coatings (Ce 3d) obtained before and after TCOS modification, respectively. The Ce 3d spectra were deconvoluted into the composed peaks and fitted for further investigations as its well discussed by Burroughs *et al.*¹⁶⁹ and E. Paparazzo.¹⁷⁰ The results deduced that the cerium based surface compounds of the coatings were consist of Ce⁴⁺, as dominant and Ce³⁺, as auxiliary surface phases. The X₁, X₂ and X₃ peaks are attributed to the 3d_{5/2} compounds of Ce⁴⁺ states, and X₄, X₅ and X₆ peaks are attributed to the 3d_{3/2} Ce⁴⁺ states, respectively; while, Y₁ and Y₂ peaks associated with 3d_{5/2} and 3d_{3/2} Ce³⁺, respectively. Due to different oxidation states of transition metals, they results in formation of shake-up lines in higher binding energies, which can be minimized by considering both 3d_{5/2} and 3d_{3/2} in cerium quantitative analysis.¹⁷¹ It can be seen that the relative intensity of the surface Ce⁴⁺ to Ce³⁺ characteristic peaks were increased through surface modification. The

corresponding concentration of Ce^{3+} and Ce^{4+} were calculated using peak areas and the correlated intensities, through following equations:

$$A(Ce^{4+}) = A(X_1) + A(X_2) + A(X_3) + A(X_4) + A(X_5) + A(X_6) \quad (\text{Eq. 4.5})$$

$$A(Ce^{3+}) = A(Y_1) + A(Y_2) \quad (\text{Eq. 4.6})$$

$$\% Ce^{4+} = \frac{A(Ce^{4+})}{A(Ce^{4+}) + A(Ce^{3+})} \quad (\text{Eq. 4.7})$$

$$\% Ce^{3+} = \frac{A(Ce^{3+})}{A(Ce^{4+}) + A(Ce^{3+})} \quad (\text{Eq. 4.8})$$

$A(\chi)$ is attributed to the peak area in accordance with its corresponding intensity, which is extracted from XPS spectra. The results show that the surface cerium compounds are consist of approximately 13 % Ce^{3+} and 87 % Ce^{4+} for bare cerium oxide coating, which are only slightly changed to 9 % Ce^{3+} and 91 % Ce^{4+} after TCOS surface treatment.

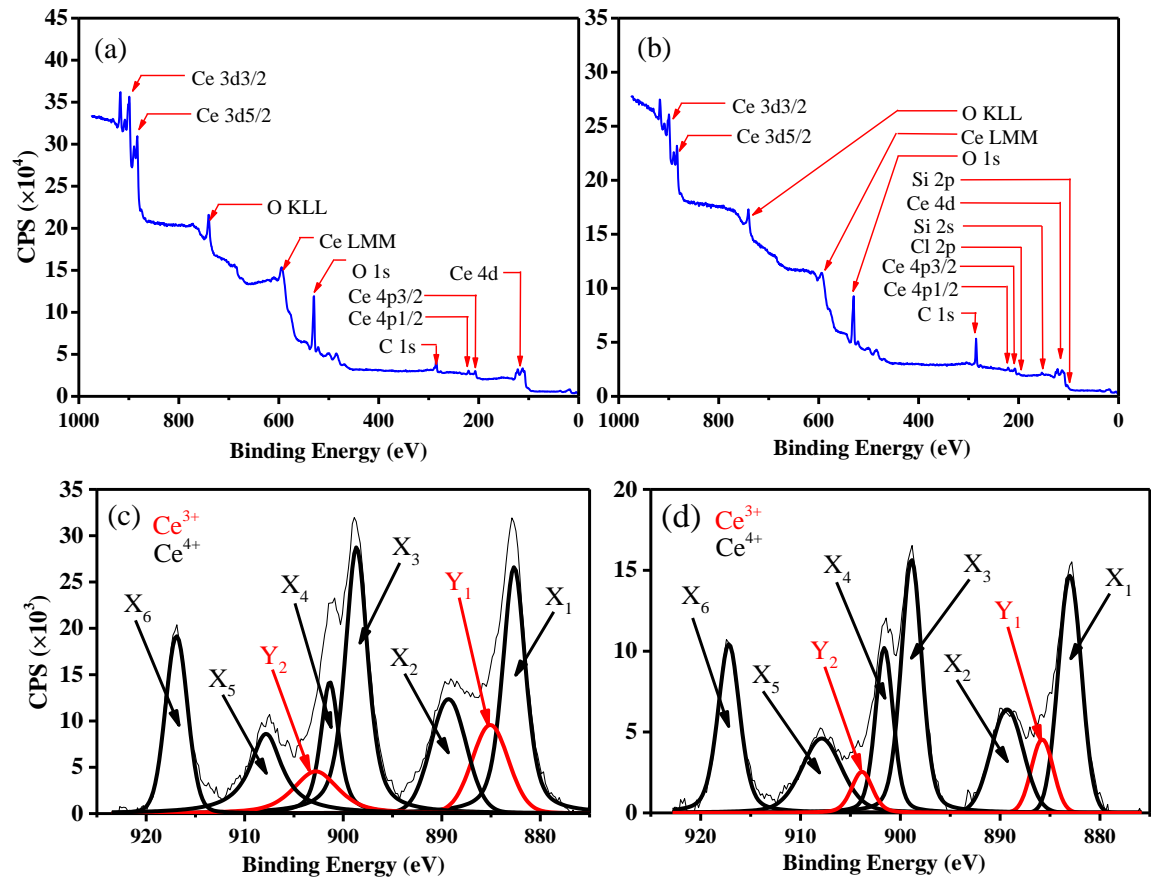


Figure 4.3. (a) and (b) display the surface XPS survey spectra of the cerium oxide coatings

before and after surface modification with TCOS, respectively; and high-resolution surface XPS spectra of Ce 3d of (c) bare CeO₂ and (d) modified CeO₂ surface.

Figure 4.4a and Figure 4.4d contrast the O 1s high-resolution XPS spectra of the unmodified and modified cerium oxide coatings. The high-resolution O 1s spectrum of the bare coating can be fitted by 4 peaks at 529.6, 531.0, 531.5 and 532.2 eV, which can be correlated to the O–Ce⁴⁺, O–Ce³⁺, O–C, and surface O–H bands.¹⁷²⁻¹⁷³ A peak centered at 532.9 eV is observed in modified cerium oxide coating XPS spectrum which is assigned to O–Si bands¹⁶⁸ forms through TCOS hydrolysis process. C 1s high-resolution XPS spectrums of the CeO₂ and modified CeO₂ surfaces is shown in Figure 4.4b and Figure 4.4e, respectively. The peaks located at 285.0 eV and 289.0 eV in XPS spectrum of CeO₂ sample are correlated to C–H bands of aliphatic hydrocarbon and C–O bands of carbonates, respectively;^{167, 174} which is attributed to atmospheric contaminations. A relative increase in C–H peak intensity was observed after surface modification that can be associated to TCOS hydrocarbon chain. The Si 2p high-resolution XPS spectra of untreated and treated CeO₂ coatings are exhibited in Figure 4.4c and Figure 4.4f, respectively. The peak at 100.2 eV was observed on TCOS treated surface, which was assigned to Si–O siloxane functional group bands;¹⁷⁵⁻¹⁷⁶ while, the Si 2p peak is not observed in unmodified cerium oxide surface. The surface chemistry of the TCOS treated CeO₂ surface obtained from FTIR and XPS analysis is schematically presented in Figure 4.4g.

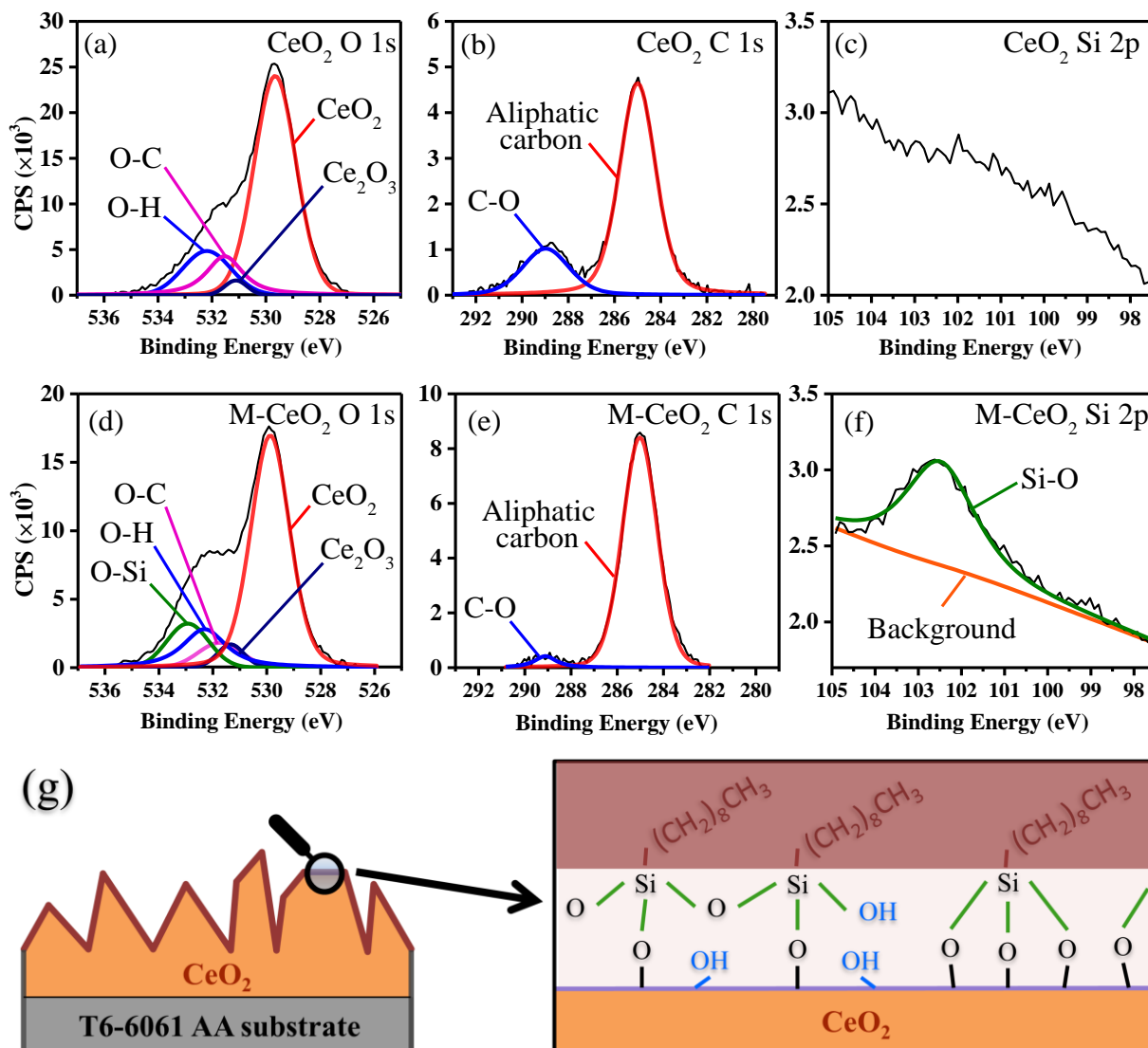


Figure 4.4. XPS spectra of (a) O 1s, (b) C 1s, and (c) Si 2p of the CeO_2 surface. XPS spectra of (d) O 1s, (e) C 1s, and (f) Si 2p CeO_2 surface after TCOS modification. (g) Schematic illustration of surface chemistry of modified cerium oxide coating.

4.4.2 Wettability and surface morphology control of CeO_2 coatings

The surface features and morphology of the CeOHCO_3 , and consequently CeO_2 coatings were manipulated in hydrothermal coating process by varying growth conditions. The effects of different processing variables, including sample positioning and hydrothermal deposition conditions (e.g. processing temperature, pressure, and

heating rate) on final coating morphology and roughness were explored in this investigation. Besides, the effect of surface features on ultimate surface wettability of the cerium oxide coated T6-6061 AA substrate were investigated (all of the water contact angles are ascribed to the TCOS modified coatings, unless otherwise stated). By varying the growth conditions, cerium oxide coatings with designed artificial surface microtextures, and consequently high level of superhydrophobicity were obtained.

4.4.3 Effect of substrate positioning

Figure 4.5a and Figure 4.5b present the schematics of horizontal and vertical samples positioned inside the autoclave, respectively. SEM images of the bare T6-6061 AA, top face, and bottom face of the coating deposited on horizontally located sample (under experiment #2 conditions) are shown in Figure 4.5c–d, respectively. During hydrothermal process, cerium hydroxycarbonate nuclei start to form homogeneously in the solution and heterogeneously over the aluminium substrate. The formed nuclei grow by temperature increment and deposit at the bottom of the autoclave and on the top face of horizontally placed sample. The accumulation of CeOHCO_3 particles on the substrates eliminates the coating evolution on the top surface, which results in non-uniform coating layer. The cerium hydroxycarbonate sediments did not show any adhesion to the surface and can easily be washed off from the top surface (Figure S4.6).

As it is shown in Figure 4.5e, the bottom face of the substrate was fully covered with uniform microstructural features, through direct growth of cerium hydroxycarbonate. On the other hand, the coating which was formed on top surface of the sample was not uniform and the structural CeOHCO_3 features did not cover whole surface. However, the EDS mapping of the top surface revealed the presence of cerium species on parts of the

surface, which were not fully covered by microtextured coating (Figure S4.7). Figure 4.5f and 5g show the SEM images of the two different places over vertically positioned sample. It was observed that the coating was not uniform on vertical sample and various surface morphologies were obtained on different locations. Microstructural features did not cover whole the surface as it is shown in Figure 4.5g.

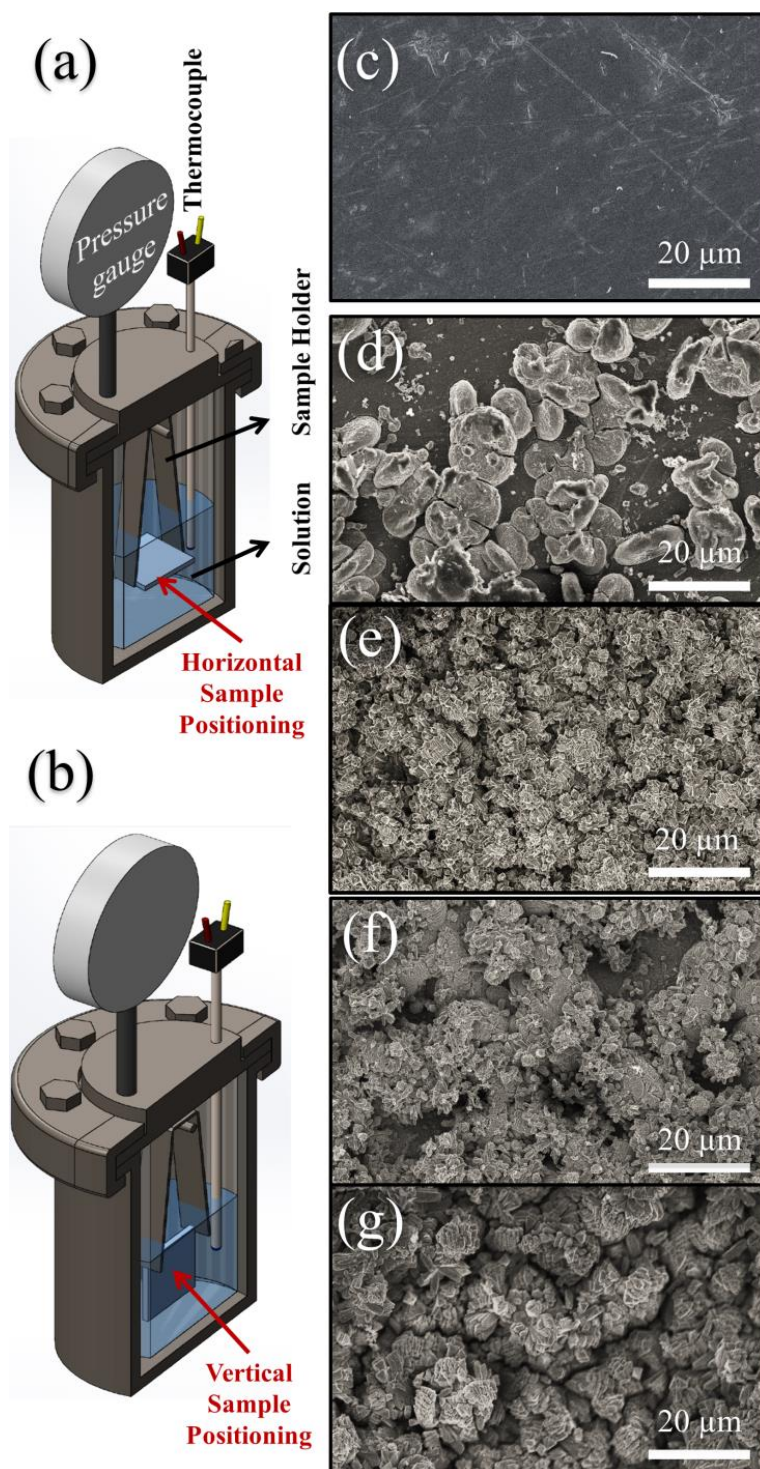


Figure 4.5. (a) and (b) the schematics of horizontal and vertical sample positioning inside autoclave, respectively. The SEM images of (c) as-washed T6-6061 AA , (d) top surface with horizontal positioning, and (e) bottom surface of horizontal sample, respectively. (f) and (g) shows the SEM images of various places over vertically positioned surface.

According to non-ambient XRD analysis, 250 °C was chosen as heating temperature through which a single phase of CeO₂ was the only phase present on the coating. The phase transformation from CeOHCO₃ to CeO₂ resulted in color change of the coatings from white to yellow (Figure S4.6c-e). Heat treatment did not cause any microstructural and/or morphological changes. However, it led to some crack formation in the layer that can be attributed to the phase change, as well as, the difference in thermal coefficients of expansion of the coating and substrate. Increasing heating temperature to 450 °C resulted in formation of cracks with larger width (Figure S4.8).

Figure 4.6a illustrates the bare AA surface and water droplet interaction, which has $70 \pm 1^\circ$ water contact angle and reveals the initial hydrophilic nature of the bare substrate. Figure 4.6b and 6c show the water droplet shape on bottom face of horizontally positioned cerium oxide coating before and after TCOS modification, respectively. As-prepared CeO₂ surface exhibited robust superhydrophilicity and the water droplet instantaneously spread out once it contacted with the surface. XPS and FTIR analysis (Figure 4.2, Figure 4.3 and Figure 4.4) revealed the deviation of oxygen to cerium ratio from the stoichiometric CeO₂ and the presence of OH bands on the surface coating layer, which increased the number of polar sites over surface and affinity of the surface to make hydrogen bonds with water molecules, and consequently introduced the hydrophilic properties to the surface. On the other hand, hierarchical and featured surface topography, in combination with microcracks, promoted the spreading of the water molecules due to capillary effect.

Highly superhydrophobic coating with a static WCA of ca. $170 \pm 2^\circ$ (Figure 4.6c) was obtained by further TCOS modification of coating, which was directly grown on the

bottom face of horizontally positioned sample (Sample 2). The XPS and FTIR results confirm that the low-surface-energy TCOS carbon chains have been assembled successfully on cerium oxide coatings through silanes reacting with surface OH bands. The outstanding superhydrophobic characteristic of the surface can be attributed to integrated effect of low-surface-energy and geometrical topography and morphology of the coating. The topography of the microfeatured cerium oxide surface, combined with surface microcracks can enhance the capability of air trapping and result in a surface with high level of water repellency.

Figure 4.6d compares the WCA of the T6-6061 AA, vertically positioned, and the top face and bottom face of horizontally positioned surfaces after TCOS treatment. The WCA of the AA surface were increased by about 37° after surface TCOS treatment. The WCA of the vertically positioned and top surface of the horizontally positioned surfaces were not consistent on different part of the coatings, which can be ascribed to their non-uniform coating structure. In contrast, the WCA of the coating formed on bottom face of the horizontally positioned sample was ca. $170 \pm 2^\circ$, which can be attributed to the uniform structure of the coatings grown on diverse substrate. Further effects of hydrothermal processing conditions on the coating formation, topography, and wettability of the cerium oxide coatings, which were specifically grown on the bottom face of the horizontally placed substrate, were investigated in following sections.

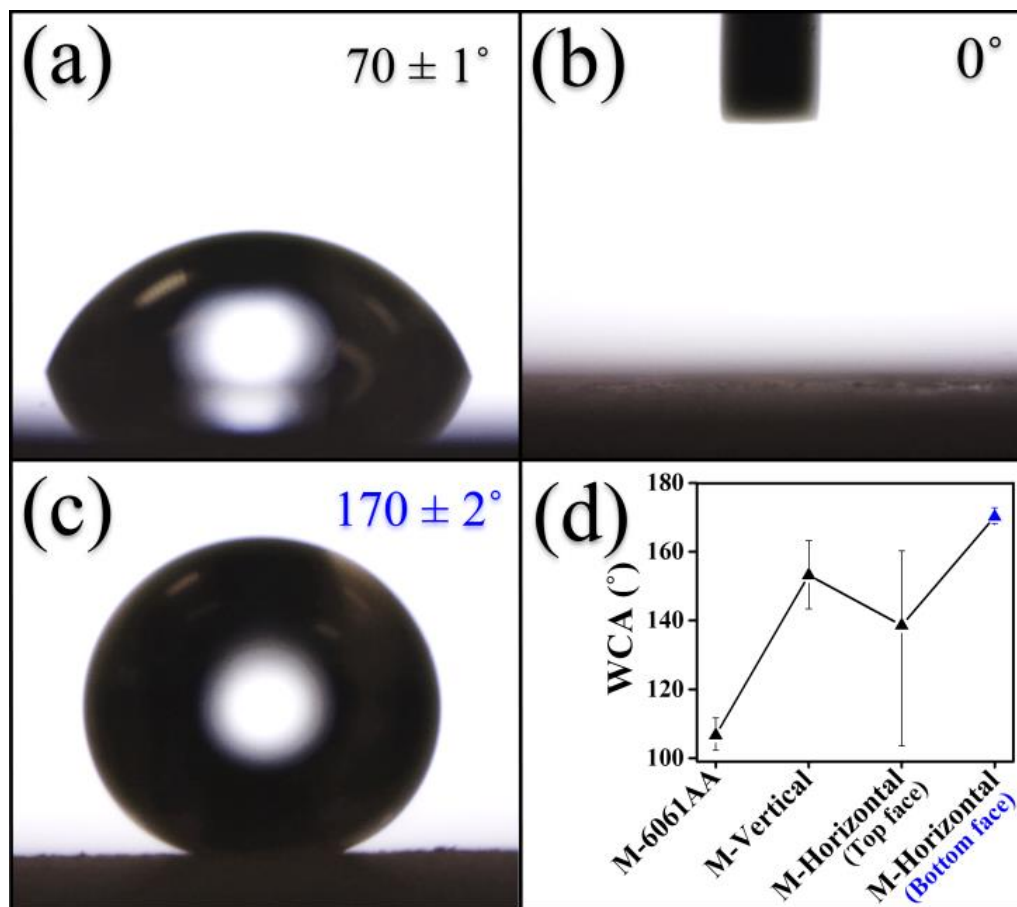


Figure 4.6. (a), (b), and (C) are the optical images of a water droplet on the bare T6-6061 AA surface, as-prepared CeO_2 coating, and TCOS modified CeO_2 Coating (Sample 2), respectively. (d) Comparisons of the contact angle of water droplet on various surfaces after TCOS modification.

4.4.4 Effects of solution amount (hydrothermal processing pressure)

Figure 4.7a–d shows the SEM images of the S1 to S4 coatings obtained at the bottom face of the horizontally placed substrates. The solution amount varying from 50 mL to 125 mL, with 25 mL intervals, while the solution concentration and other hydrothermal processing conditions kept constant. Considering that the autoclave capacity was constant, altering the solution amount resulted in changes in processing pressure. As it is shown in Table 4.2, the processing pressure was increased from approximately 60 psi to 200 psi by increasing the solution amount from 50 mL to 125 mL.

Figure 4.7e–h shows the higher magnification of the Figure 4.7a–d, respectively. It was observed that surface microtextures were altered by changing the processing pressure and finer surface structures were produced by raising the processing pressure. The S1 sample surface features consist of triangular prism structures covered by condense multi-faceted plates. The microfeatures were distributed fairly uniform all over the surface. However, they did not cover the whole surface. By increasing the reaction pressure to about 90 psi and 150 psi, the surface features became finer and cover the whole surface. The SEM images of cross section view of the S2 sample revealed that a micro-layer of coating was formed under the microtextured surface features and shielded the substrate. However, further increase in solution amount (S4 coating), and consequently pressure increase, resulted in non-uniform coating formation consists of very fine randomly oriented rod-like structures. Microfeatures did not cover the substrate perfectly on S4 coating.

Table 4.2. The surface roughness (Sa), static water contact angle, and rolling angle of bare T6-6061 AA, TCOS modified T6-6061 AA, and S1 to S4 coatings grown on the bottom face of horizontally placed T6-6061 AA.

Sample	Solution	Processing	Surface	Static	Rolling
Name	Amount (mL)	Pressure (psi)	Roughness (μm)	WCA ($^\circ$)	Angle ($^\circ$)
T6-6061 AA	N/A	N/A	0.04 ± 0.01	70 ± 1	> 20
M-T6- 6061 AA	N/A	N/A	0.05 ± 0.01	107 ± 2	> 20
S1	50	~60	1.25 ± 0.09	158 ± 3	8.4 ± 0.9
S2	75	~90	1.69 ± 0.05	170 ± 2	2.4 ± 0.2
S3	100	~150	1.40 ± 0.05	165 ± 2	4.7 ± 0.5
S4	125	~200	0.42 ± 0.13	147 ± 6	> 20

Figure 4.7i–l show the associated surfaces three dimensional profile of the sample S1 to S4 (Figure 4.7a–d), respectively. The processing pressure had an impact on the surface roughness and consequently the wettability of the coatings. All the coatings were superhydrophilic prior to TCOS surface treatment. The surface roughness, static WCA, and rolling angle of the coatings after TCOS modification are shown in Table 4.2 to clarify the relation of the surface roughness and the wettability of surfaces. The as-received T6-6061 AA substrate had surface roughness around $0.04 \pm 0.01 \mu\text{m}$ (Figure S4.9). The surface roughness was increased to around $1.25 \pm 0.09 \mu\text{m}$ for S1 sample. As it is shown in Figure 4.7j, the roughness further increased up to ca. $1.69 \pm 0.05 \mu\text{m}$ and $1.40 \pm 0.05 \mu\text{m}$ for the coatings formed at about 90 psi and 150 psi processing pressure, respectively. However, the surface roughness was extremely decreased down to ca. 0.42

$\pm 0.13 \mu\text{m}$ by further increase in processing pressure. As it is well studied that the rough surface is crucial to reach Cassie-Baxter state and develop superhydrophobic surfaces. However, the surface roughness is by no means the only parameter to determine the surface wettability. The hydrophobicity of the coatings was increased by increasing the surface roughness. As it was expected, the S2 sample that was processed in 75 mL solution with surface roughness of $1.69 \pm 0.05 \mu\text{m}$, were exhibited highest level of superhydrophobicity by static WCA of $170 \pm 2^\circ$ and rolling angle of less than 3° .

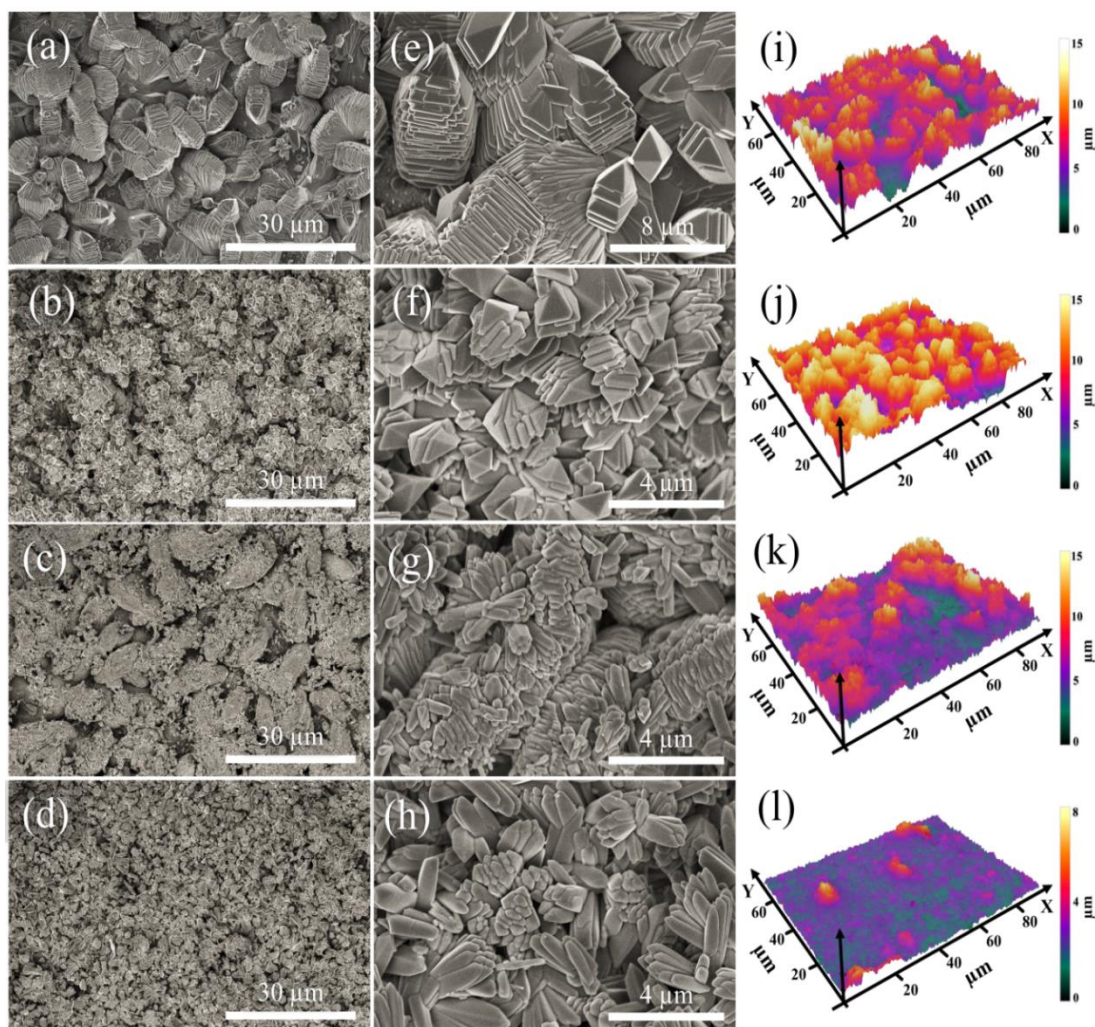


Figure 4.7. (a–d) Low magnification SEM images, (e–h) High magnification SEM images, and (i–l) 3D surface profile of the S1 to S4 coatings grown on the bottom face of horizontally placed T6-6061 AA, respectively.

4.4.5 Effect of reaction temperature

Hydrothermal processing temperature also had an impact on the surface morphology, roughness, and consequently wettability of the coatings. The effect of hydrothermal processing temperature on the coating formation and their surface microtexture was investigated over a temperature range of 130–170 °C while keeping the heating rate at 1 °C/min and other processing conditions constant (Table 4.3).

Figure 4.8a–d and Figure 4.8e–h show the low and high magnification SEM images of the S5 to S8 coatings, which were obtained on the diverse substrate at 130, 140, 160 and 170 °C processing temperature, respectively. The hydrothermal solution amount and heating rate were set to 75 mL and 1 °C/min for all coatings, respectively. It was observed from preliminary experiments that uniform coatings form above 130 °C. Figure 4.8a and 8d show the SEM images of the coating form at 130 °C at different magnifications. Although, it can be observed that uniform coatings were developed all over the surface, the microstructural features did not formed completely at 130 °C (Figure 4.8d). Figure 4.8b and 8e shows the SEM images of S6 coating obtained at 140 °C at different magnifications. The results show that the surface microfeatures completely formed at 140 °C. The surface SEM images of the coatings produced at 150 °C (Figure 4.7b and 7f), 160 °C (Figure 4.8), and 170 °C (Figure 4.8c and 8f) revealed that the shape of the surface microtexture were not considerably changed by further processing temperature increments up to 170 °C. However, the width of the surface prism structures slightly increased by temperature increment.

Table 4.3. The surface roughness (Sa), static water contact angle, and rolling angle of S2, S5, S6, S7, S8, and S9 coatings grown on the bottom face of horizontally placed T6-6061 AA.

Sample Name	Solution amount (mL)	Processing Temperature (°C)	Surface Roughness (μm)	Static WCA (°)	Rolling Angle (°)
S5	75	130	0.65 ± 0.04	158 ± 1	5.4 ± 0.3
S6	75	140	0.96 ± 0.06	161 ± 2	3.4 ± 0.2
S2	75	150	1.69 ± 0.03	170 ± 2	2.4 ± 0.2
S7	75	160	1.46 ± 0.03	167 ± 2	3.1 ± 0.2
S8	75	170	1.15 ± 0.02	164 ± 2	3.7 ± 0.3

For further investigation into the effect of processing temperature on coating surface microtexture, the coating process were performed at 170 °C with 50, 100 and 125 mL solution amount. The low and high magnification SEM images of the coatings evolved on diverse substrate at 170 °C with 50, 100 and 125 mL solution amount are shown in Figure S4.10a–c and Figure S4.10d–f, respectively. It was observed that the S1 coating surface microstructures, which were composed of tightly assembled and aligned plates, were grown to larger bundles by temperature increase. However, the shape of the microstructures was not considerably changed by temperature increase up to 170 °C. The surface structure of the coatings that formed in 100 mL and 125 mL of solution also showed insignificant changes by temperature increment. However, using 125 mL solution amount did not result in uniform coating formation at 170 °C.

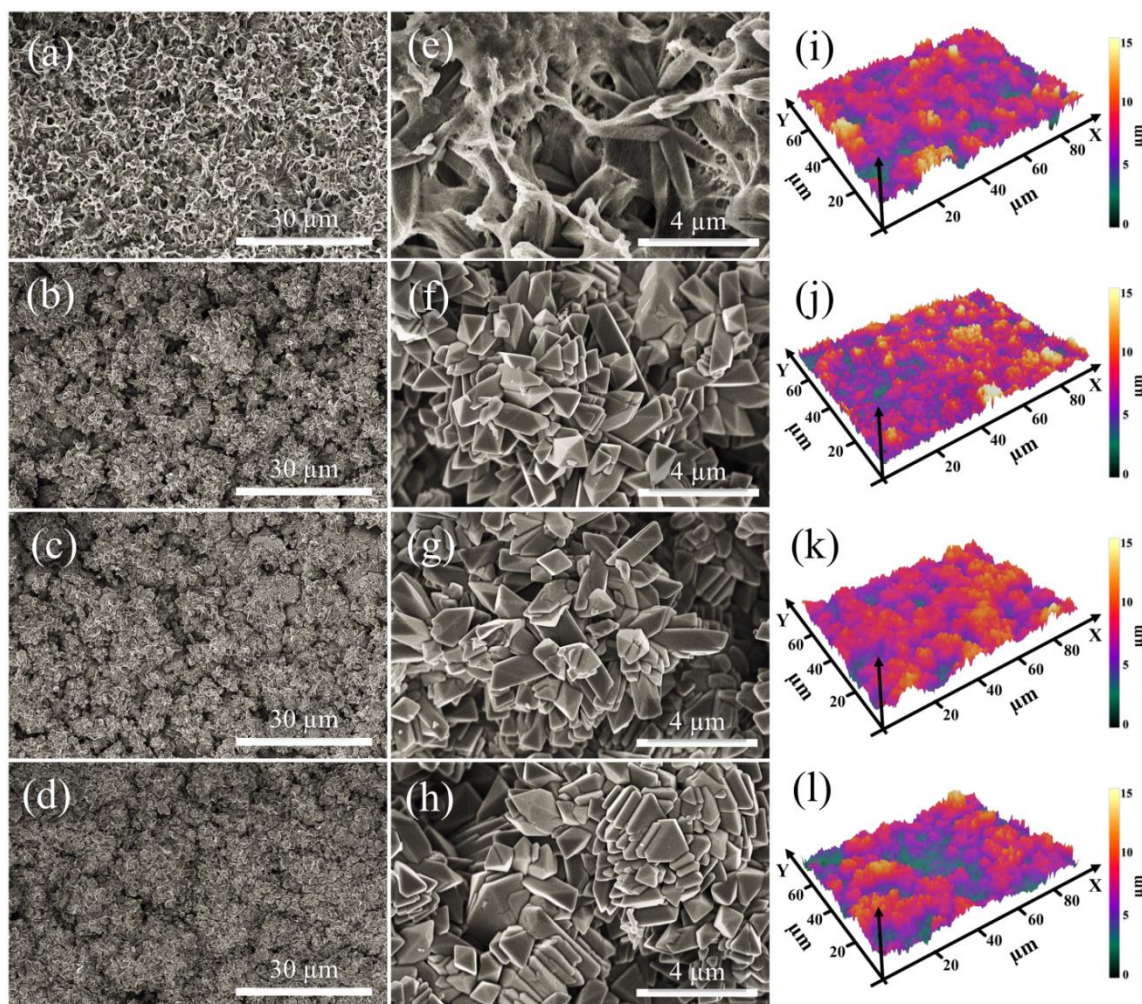


Figure 4.8. (a–d) Low magnification SEM images, (e–h) High magnification SEM images, and (i–l) 3D surface profile of the S5 to S8 coatings grown on the bottom face of horizontally placed T6-6061 AA, respectively.

Figure 4.8i–l show the surface 3D profile of S5 to S8 samples, respectively. The surface roughness, Static WCA, and rolling angle of the TCOS treated coatings are shown in Table 4.3. Although just a negligible surface microstructural change was observed for the coatings by altering the hydrothermal processing temperature, their surface roughness was considerably changed. As it is shown in Table 4.3, the surface roughness of the coatings was increased from ca. $0.65 \pm 0.04 \mu\text{m}$ up to ca. 1.69 ± 0.03

μm by increasing the processing temperature from 130 °C to 150 °C, which can be attributed to the completion of the coating formation from precursors. On the other hand, it was observed that the surface roughness of the coatings was decreased down to about $1.15 \pm 0.02 \mu\text{m}$ by further increase in temperature up to 170 °C. The reduction in surface roughness of the coating by further temperature increment can be attributed to slight increase in the width of the prism shaped microfeatures that can affect the aspect ratio of the surface features. It was also previously reported that the hydrothermal reaction temperature affects the aspect ratio of the synthesized particles (e.g. nanorods become shorter with increasing the temperature).

The static water contact angle and rolling angle of the coatings obtained at various temperatures from 130 °C to 170 °C are shown in Table 4.3. The results showed that all of the coatings were superhydrophobic as they have static WCA more than 150° and the rolling angle less than 10°. As it was expected, the hydrophobicity of the surfaces with higher roughness was noticeably higher than the ones with lower surface roughness. However, surface roughness is not the only factor affecting the wettability of the surfaces.

4.4.6 Effect of hydrothermal heating rate

Heating rate is another hydrothermal processing condition that affects the final coating's formation, microtexture, and consequently wettability. The hydrothermal conditions of the S2 coating, which had the highest level of superhydrophobicity among above samples, were chosen as reference conditions for investigating the heating rate effect (Table 4.4). Figure 4.9a–b and Figure 4.9c–d show the low and high magnification SEM images of the S9 and S10 coatings, respectively. The S9 and S10 coatings were

grown on diverse substrate at 2 °C/min and 0.5 °C/min, respectively; while the other processing conditions were set as the S2 coating conditions.

As it is shown in Figure 4.9a and 9c, increasing the heating rate to 2 °C/min resulted in formation of coating, which was consist of fine prism structures in combination with bundles of compacted and oriented plates, which distributed all over the surface. On the other hand, the coating obtained at heating rate about 0.5 °C/min was mostly composed of randomly ordered prisms and compact plate bundles (Figure 4.9b and 9d). However, the coating had not formed uniformly over the surface.

Table 4.4. The surface roughness (Sa), static water contact angle, and rolling angle of S2, S9 and S10 coatings grown on the bottom face of horizontally placed T6-6061 AA.

Sample	Solution	Processing	Heating	Surface	Static	Rolling
Name	amount (mL)	Temperature (°C)	rate (°C/min)	Roughness (μm)	WCA (°)	Angle (°)
S9	75	150	2	1.43 ± 0.04	167 ± 2	5.1 ± 0.3
S2	75	150	1	1.69 ± 0.03	170 ± 2	2.4 ± 0.2
S10	75	150	0.5	2.53 ± 0.35	159 ± 6	8.7 ± 1.1

Figure 4.9e and Figure 4.9f show the surface 3D profiles of S9 and S10 samples, respectively. The surface roughness of the S9 coating was about 1.43 ± 0.04 μm and showed high degree of superhydrophobicity with static WCA of ca. $167 \pm 2^\circ$ and rolling angle less than 5° . On the other hand, decreasing the heating rate down to 0.5 °C/min resulted in an increase in coating surface roughness up to ca. 2.53 ± 0.35 μm. As it was previously mentioned, the surface roughness is not the only factor that affects the surface wettability. Although S10 coating displayed higher surface roughness than S2 and S10

samples, it has superhydrophobicity with a contact angle of ca. $159 \pm 6^\circ$ and rolling angle less than 10° .

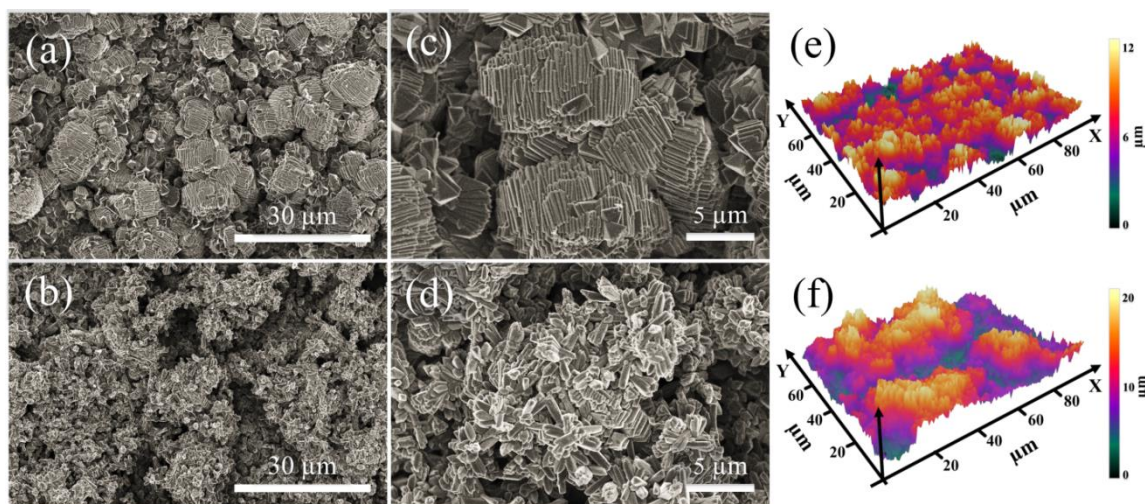


Figure 4.9. (a) and (b) Low magnification SEM images, (c) and (d) High magnification SEM images, and (e) and (f) 3D surface profile of the S9 to S10 coatings grown on the bottom face of horizontally placed T6-6061 AA, respectively.

4.4.7 Mechanical durability and chemical stability of superhydrophobic coating

S2 coating shows the highest level of superhydrophobicity by WCA of ca. $170 \pm 2^\circ$ and rolling angle of ca. $2.4 \pm 0.2^\circ$. Herein, different properties, such as, durability and stability of the non-wetting S2 coating were also investigated. The water droplet impaction process of the superhydrophobic surface is shown in Figure 4.10a. The droplet was thoroughly bounced of the surface and left the surface dry (see Supporting Information video 1). Figure 4.10b displays the high-speed camera images of the rolling water droplet on the $2.4 \pm 0.2^\circ$ tilted S2 coating. The water droplet exhibited extreme mobility over the surface and simply rolled of the surface at remarkably low tilting angles (see Supporting Information video 2).

Furthermore, the self-cleaning property of the superhydrophobic surface was also investigated by recording the rolling water droplet interaction with surface dust

contaminations. Grinded red calcium carbonate chalk dust was used as surface pollutant. The digital images of the S2 superhydrophobic coating self-cleaning process are shown in Figure 4.10c. The chalk dust was stuck to rolling water droplet and removed from the surface; and consequently, the superhydrophobic surfaces left clean and dry (see Supporting Information Video 3).

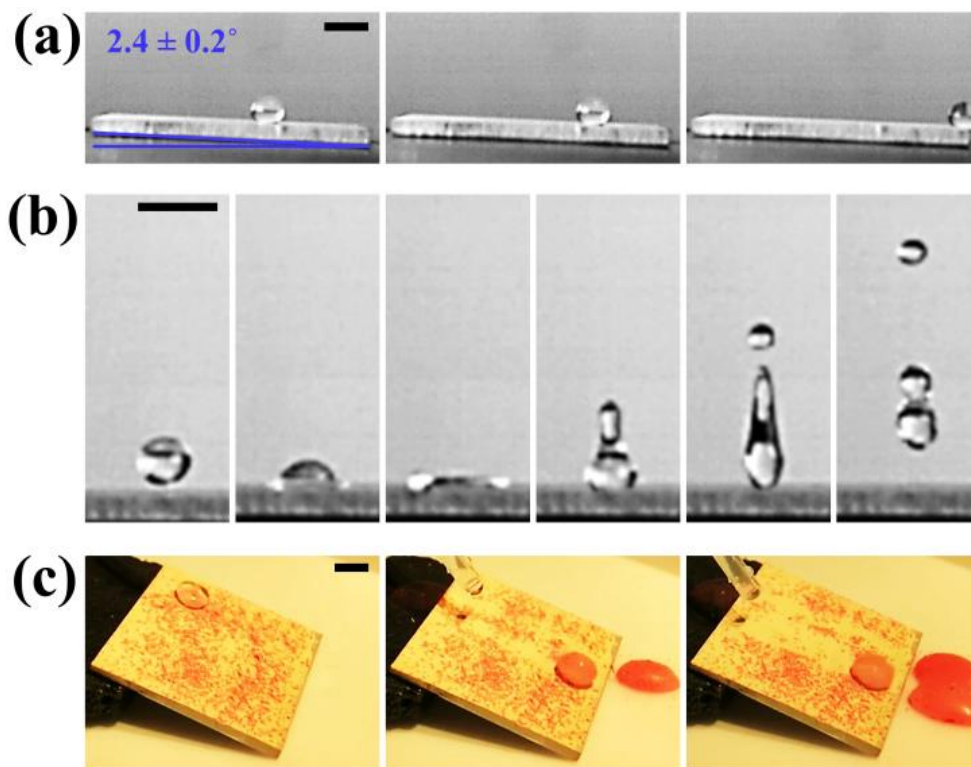


Figure 4.10. (a) water droplet rolling down the superhydrophobic S2 coating. (b) High-speed photography images of a water droplet bouncing of the S2 coating (impact velocity $\sim 0.9 \text{ ms}^{-1}$). (c) Self-cleaning behavior of the superhydrophobic S2 coating. Scale bar $\sim 4.0 \text{ mm}$.

Practical application of non-wetting surfaces is determined by their mechanical durability and chemical stability, which has known as most challenging issues for industrial implication of superhydrophobic surfaces. The mechanical wear resistance of the superhydrophobic properties of the S2 coating was investigated upon dragging the

surface over SiC abrasive paper (grid #800) for 1.0 m under applied pressures up to 4.90 kPa. As it is shown in Figure 4.11a, the superhydrophobic properties of the coatings decreased by increasing an applied pressure, as its WCA and rolling angle decreased and increased, respectively. The SEM images of the coatings after dragging for 1.0 m over abrasive paper under 3.92 kPa and 4.90 kPa applied pressures are presented in Figure S4.11. The superhydrophobic coating exhibited high level of abrasion resistance by retaining its superhydrophobicity and its surface microfeatures did not show remarkable changes upon 3.92 kPa applied pressure. However, the superhydrophobic properties of the S2 coating were degraded and the surface features were abraded under 4.90 kPa applied pressure.

The stability of the superhydrophobic coating was evaluated by storing the samples under ambient condition (Figure 4.11b). The coating's hydrophobicity was not affected by storing for 100 days, as evidenced by a WCA and a rolling angle about $168 \pm 3^\circ$ and $3 \pm 0.3^\circ$, respectively. Figure 4.11c shows the contact angle of the buffer solution and the coating within pH range from 2 to 12. The contact and rolling angles of the acidic buffer (pH = 2) with surface were about $156 \pm 3^\circ$ and $7.6 \pm 1.2^\circ$, respectively; while the coating had ca. $161 \pm 3^\circ$ contact angle and ca. $5.9 \pm 1.5^\circ$ rolling angle in interaction with basic solution (pH = 12). The results show that the superhydrophobic coating retains its properties whether in interaction with acidic or alkaline solutions, but some degradation can be observed at extreme pH conditions, likely due to catalyzed hydrolysis of the silanes.

The chemical stability of the superhydrophobic coatings in corrosive media is decisive for their practical applications such as marine industry, which was investigated by

immersing the sample into a 3.5 wt % NaCl solution, mimicking sea water. Figure 4.11d shows the WCA and Rolling angle evolution of the S2 coating upon immersion in the 3.5 wt % NaCl solution for 48 h. The WCA and Rolling angle of the coating slightly decreased down to ca. $161 \pm 2^\circ$ and increased up to ca. $6 \pm 0.9^\circ$, respectively. The results revealed that the superhydrophobicity of the coating was highly stable and retained its non-wetting properties even after 48 h of exposure to NaCl corrosive media.

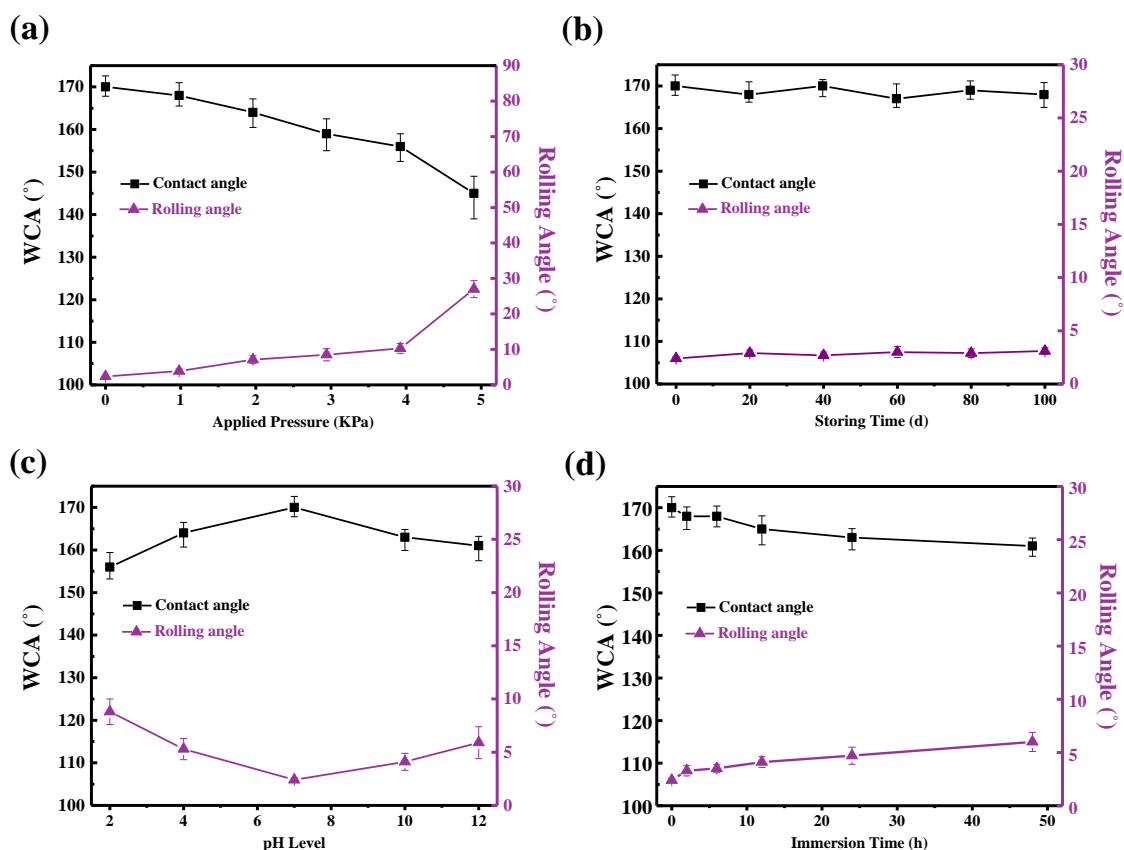


Figure 4.11. Development of water contact angle and Rolling angle of the superhydrophobic S2 coating upon (a) dragging for 1.0 m length under varying applied pressure, (b) storing under ambient condition, (c) different pH values between 2 to 12, and (d) immersion time in 3.5 wt % NaCl aqueous solution.

4.4.8 Corrosion protection

The corrosion protection of the coated and bare T6-6061 AA substrates was investigated through potentiodynamic polarization measurements. The corrosion potential (E_{corr}), pitting potential (E_{pit}), corrosion current density (J_{corr}) and corrosion rate of the surfaces are the most important parameters that can be extracted from the polarization curves. The corrosion potential ascribes to the thermodynamic tendency of a metal surface to oxidize and higher E_{corr} value represents lower corrosion tendency. On the other hand, the corrosion rate of the metallic surfaces is identical to its corrosion current density; while the amount of metal desolation is strictly proportional to the generated electricity.

The corrosion rate is usually expressed as degradation of a specific area of exposed material during a limited time when the degradation happens uniformly over the surface. However, in case of aluminium and its alloys, localized corrosion such as pitting corrosion, happens due to their face centered cubic (FCC) crystalline structure. The dislocations easily move along the FCC closed pack planes $\{111\}$ and directions (110) and develop a network of dislocations, which makes it more vulnerable to be corroded. The corroding species penetrate through the body of material along the defect pass ways. Therefore, penetration rate should be considered as corrosion rate terminology in case of localized corrosion.

Figure 4.12a shows the Tafel plots of the bare, as well as cerium oxide coated (under S2 hydrothermal processing condition), T6-6061 AA substrates before and after TCOS surface treatment. Table 4.5 expresses the corrosion potential, corrosion current density, and penetration rate of the various samples, which were derived from Tafel extrapolation. The corrosion potential of the AA substrates slightly moves to more negative values (~ -

0.05 V) after cerium oxide coating. However, it can be observed that the CeO_2 coating improved the corrosion resistance of the bare T6-6061 AA by decreasing the corrosion current density, and consequently penetration rate of bare AA. TCOS surface modification was made a small shift in both bare and cerium oxide coated corrosion potentials (< 0.01 V). The penetration rate of the bare T6-6061 AA substrate also decreased for about 2.4 times after surface TCOS treatment, which can be attributed to the waxy characteristic of the TCOS, which slightly decrease the cathodic reaction rate and current.

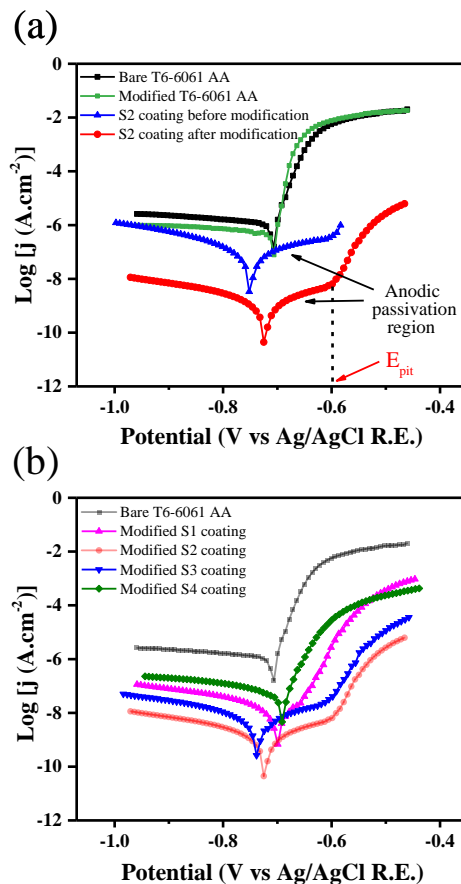


Figure 4.12. The potentiodynamic polarization curves (Tafel plots) of the (a) bare and cerium oxide coated (S2 hydrothermal condition) T6-6061 AA, before and after surface modification; (b) bare and the superhydrophobic S1 to S4 coated T6-6061 AA.

As it was expected, the superhydrophobic cerium oxide coating (S2 sample) exhibited extensive corrosion protection for T6-6061 AA substrate. The corrosion current density of superhydrophobic S2 coating was about 0.13 % of the bare AA substrate and the penetration rate was more than 750 times less than the bare substrate. The high level of corrosion protection acquired by superhydrophobic CeO₂ coating can be ascribed to the synergetic effects of protective cerium oxide layer and non-wetting surface properties, which restricts the interaction of water molecules with the surface. Besides, the cerium oxide layer developed a protective passive layer that blocks the anodic current and shifts the pitting potential to more positive values. The passivation effect was also seen for cerium hydroxycarbonate coated AA as it is presented in Supporting Information Figure S4.12a.

Table 4.5. Corrosion potential (E_{corr}), corrosion current density (j_{corr}), and penetration (corrosion) rate of the T6-6061 AA substrate before and after various surface coating and treatment.

Sample Name	E_{corr} (mV)	j_{corr} ($\text{A}\cdot\text{cm}^{-2}$)	Penetration rate ($\text{mm}\cdot\text{y}^{-1}$)
Bare AA ^a	-0.705	1.21×10^{-6}	1.32×10^{-2}
TCOS-modified AA	-0.686	5.06×10^{-7}	5.51×10^{-3}
Ce(OH)CO ₃ coated AA (S2 hydrothermal condition)	-0.765	2.24×10^{-7}	2.44×10^{-3}
CeO ₂ coated AA (S2 hydrothermal condition)	-0.752	7.32×10^{-8}	7.97×10^{-4}
S1 SHC ^b AA	-0.699	1.58×10^{-8}	1.72×10^{-4}
S2 SHC AA	-0.718	1.59×10^{-9}	1.74×10^{-5}
S3 SHC AA	-0.731	3.50×10^{-9}	3.81×10^{-5}
S4 SHC AA	-0.691	5.34×10^{-8}	5.81×10^{-4}
S5 SHC AA	-0.703	3.93×10^{-8}	4.27×10^{-4}
S6 SHC AA	-0.729	5.44×10^{-9}	5.93×10^{-5}
S7 SHC AA	-0.720	1.97×10^{-9}	2.14×10^{-5}
S8 SHC AA	-0.711	2.91×10^{-9}	3.16×10^{-5}
S9 SHC AA	-0.709	5.68×10^{-9}	6.18×10^{-5}
S10 SHC AA	-0.741	9.35×10^{-9}	1.02×10^{-4}

^a AA: T6-6061 aluminium alloy

^b SHC: Superhydrophobic coated

Figure 4.12b compares the Tafel plots of the superhydrophobic S1 to S4 coatings obtained at different hydrothermal pressures, and consequently had different surface microtextures and superhydrophobicity. The Tafel plots of S2 and S3 samples show relatively larger passive regions, which resulted in much higher pitting potential. In

contrast, the S1 sample shows a small passive region and S4 sample did not exhibit any passivation characteristics by exhibiting the polarization pattern close to bare T6-6061 AA substrate. These changes in passivation properties of different coatings can be attributed to the quality of coating to cover the entire surface; while the aluminium surfaces corrode in form of pits and highly susceptible to localized corrosion. As it is shown in Figure 4.7, the S3 and S4 coatings provided a full coverage over AA substrates; while the S1 and S2 coating condition did not resulted in full surface coverage. The same passivation behavior was also observed in all other coatings Tafel plots as it is shown in Figure S4.12. On the other hand, it can be seen that the S2 sample shows better corrosion resistance than S3 sample, which can be associated to its higher water repellency. It was generally observed that the surfaces with higher level of hydrophobicity (higher WCA) showed better corrosion protection (Figure S4.12).

It can be concluded that the S2 coated sample which had well-defined microtextured surface, not only possessed the highest level of water repellency among the samples (WCA ca. $170 \pm 2^\circ$), but it also exhibited significant corrosion protection for T6-6061 AA substrate by decreasing the corrosion current density by about three order of magnitude.

4.5 Conclusions

In summary, an effective template- and surfactant-free hydrothermal approach was employed for developing CeO_2 coating with surface hierarchically microtextures on T6-6061 multipurpose aluminium alloy. By controlling the deposition conditions such as sample positioning, hydrothermal pressure and temperature, coatings with various surface architecture and morphologies were obtained. A robust superhydrophobic coating with a

contact angle of $170 \pm 2^\circ$ and rolling angle of $2.4 \pm 0.2^\circ$ was successfully fabricated on the aluminium alloy. The outstanding non-wetting property of the coatings were acquired by combined effects of its facial microtexture and surface assembly of trichloro(octyl)silane as low-surface-energy compound. The superhydrophobic surface was exhibited remarkable mechanical and chemical durability, self-cleaning ability, storability, and excellent corrosion protection for the aluminium alloy substrate. The significant corrosion protective performance of the coatings was derived from synergic effects of cerium oxide protective layer and its high level of superhydrophobicity. The coating also retained its non-wetting characteristic in both acidic and alkaline conditions. The facile and reproducible hydrothermal deposition approach and surface treatment can be utilized for developing robust superhydrophobic and corrosion protective layer on other metal and metal alloys for a variety of industrial applications.

4.6 Supporting Information

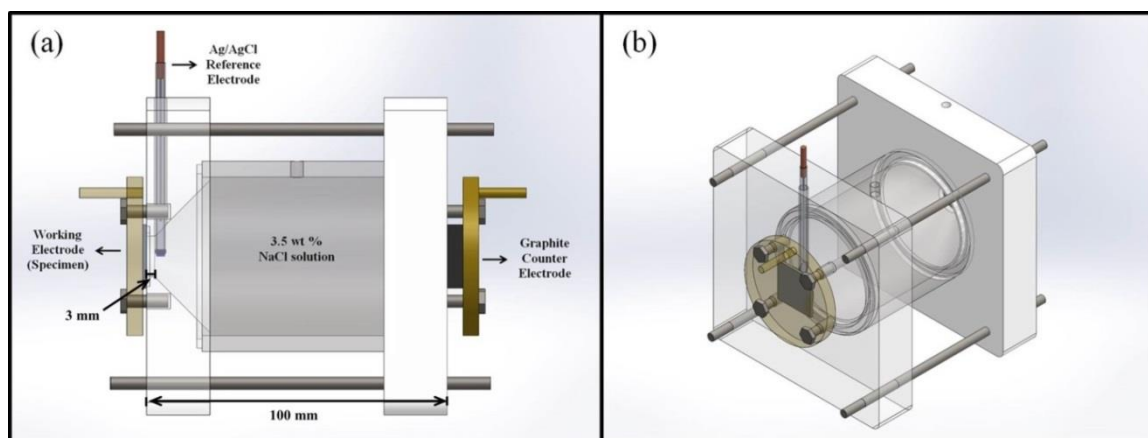


Figure S4.1. Schematic of the corrosion cell, (a) front view and (b) isometric view.

4.6.1 Ag/AgCl reference electrode preparation

The silver-silver chloride reference electrode (Ag/AgCl/NaCl (saturated in water)) consists of a silver wire coated with silver chloride (AgCl) and immersed into a saturated

NaCl solution. The compartment of the electrode is glass tubing, a cap on top, and a Vycor® frit which is attached to the glass tubing using Teflon heat-shrink tubing,. Vycor® frit is a porous glass which serves as an electrical and ionic conductivity bridge (or pathway) between the filling solution inside the reference electrode and the bulk of the solution in the cell (Figure S4.2).

First, Teflon heat shrinkable tubing was cut in a proper size and carefully fitted over a clean glass tube. Then, a Vycor® frit was inserted into the Teflon heat shrinkable tubing. After that, the Teflon tubing was shrined using a heat gun. Next, the glass tube body was carefully filled with an electrode filling solution (no air bubbles should be trapped in the glass tube). The electrode filling solution depends on the medium utilized in the experiment. We used saturated NaCl in aqueous medium as the filling solution for our electrode.

The AgCl coating was prepared by electro-oxidation of the silver wire at a constant potential of 1.5 V for 5 minute in an aqueous solution containing 0.1 M KCl and 0.1 M HCl. The Ag/AgCl wire was then thoroughly rinsed with distilled water and was placed in the glass tube filled with the saturated NaCl solution. The Ag/AgCl electrode was then stored in a beaker containing saturated NaCl solution. The potential of the Ag/AgCl/NaCl reference electrode was tested versus a standard hydrogen electrode (SHE), before use.

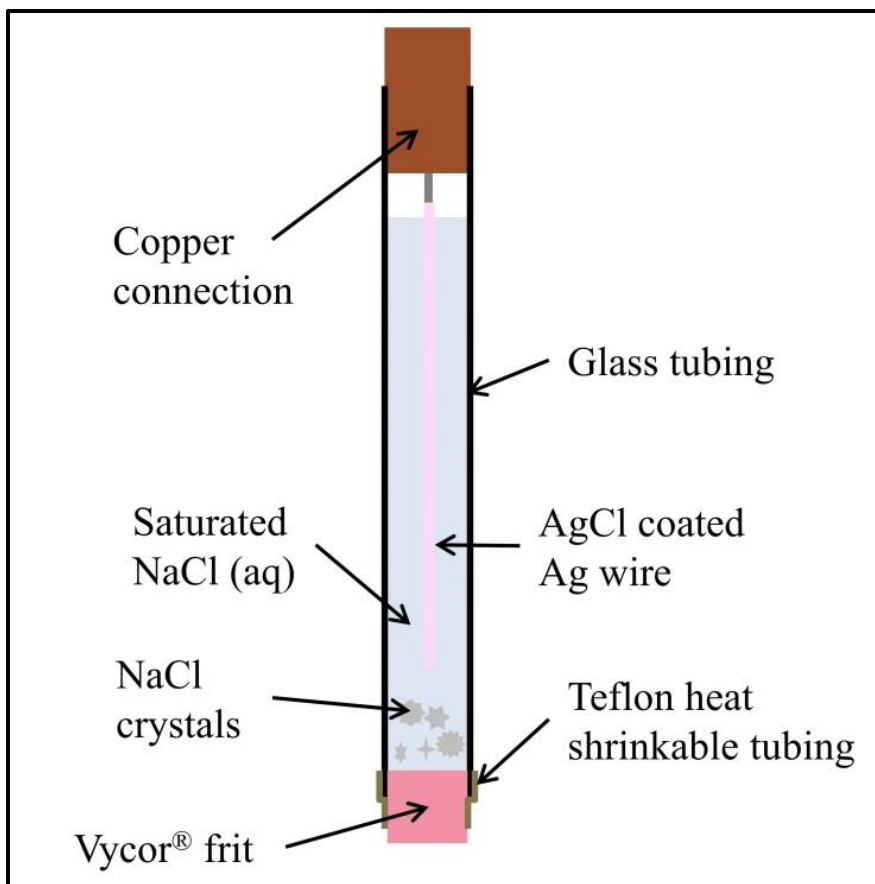


Figure S4.2. Schematic of Ag/AgCl reference electrode.

4.6.2 Crystallographic characterization

The crystalline phase analysis of the coatings was carried out by a PANalytical Empyrean X-ray diffractometer, operating at 45 kV and 40 mA. The scanning rate and size were set to $0.53^\circ/\text{s}$ and 0.0263° , respectively. A 10 mm fixed beam mask, a 0.04 rad Solar slit, a $1/2^\circ$ Anti-scatter slit, and a $1/2^\circ$ fixed Divergence slit were used for incident-beam. A 0.04 rad large solar slit with the PIXcel 3D-Medipix3 1×1 detector with an active angle 2θ of 3.347° were utilized for diffracted beam. The XRD pattern fitting are performed by PANalytical HighScore Plus software (V 4.1.0.19887). The software was equipped with PDF-4+ database.

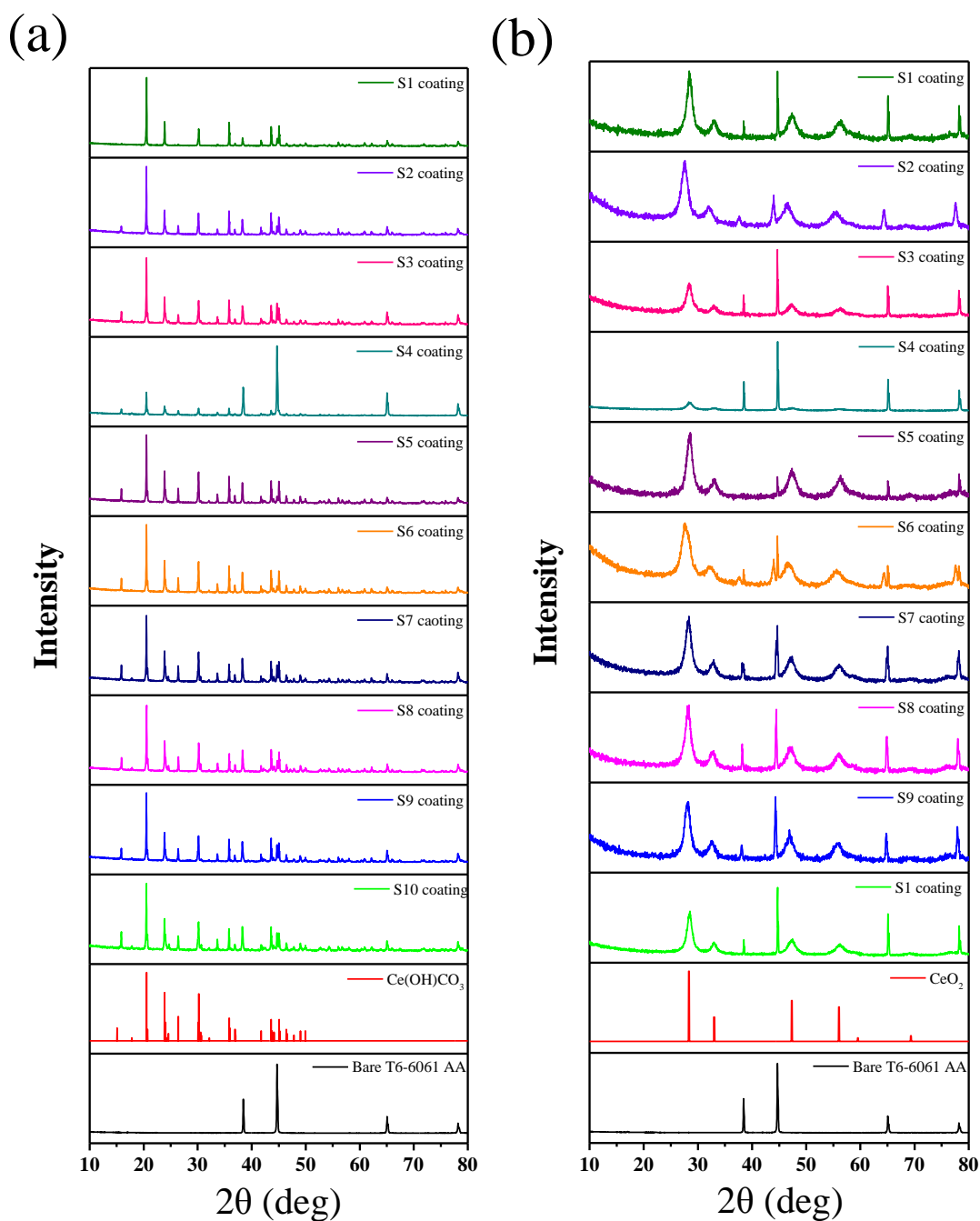


Figure S4.3. XRD patterns of S1 to S10 coatings (a) as-hydrothermally deposited and (b) after heat treatment at 250 °C.

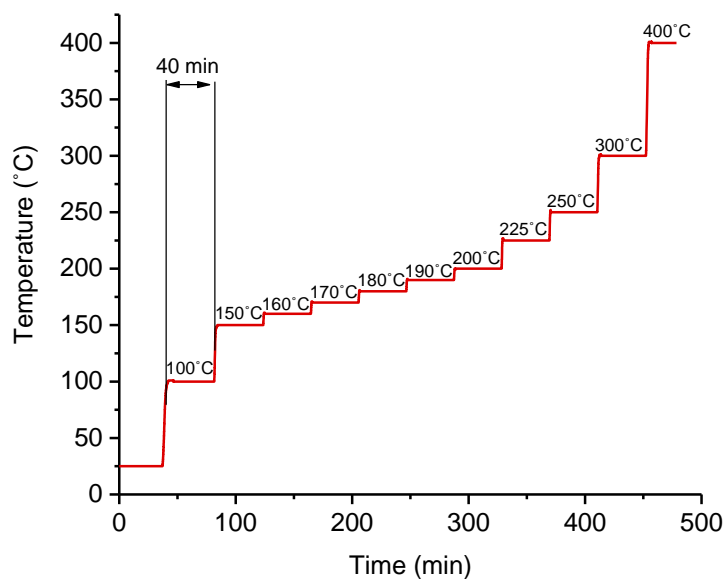


Figure S4.4. Non-ambient XRD heating profile.

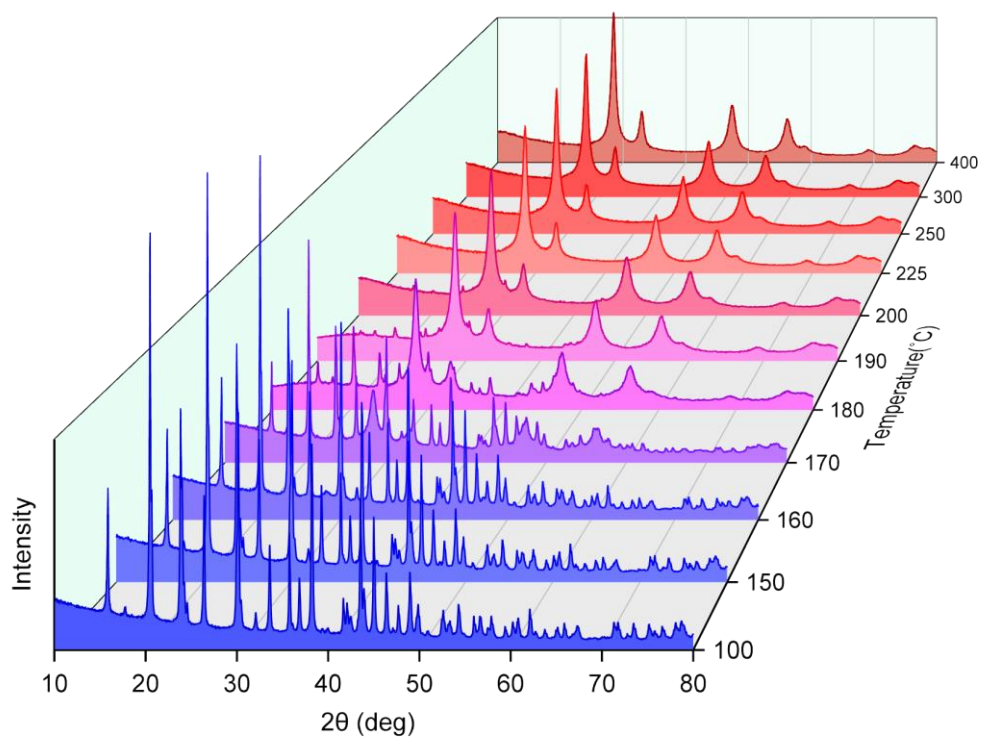


Figure S4.5. The non-ambient XRD characteristic peaks of as-deposited particles associated to experiment #2 processing condition at different temperatures in range of 100 °C to 400 °C.

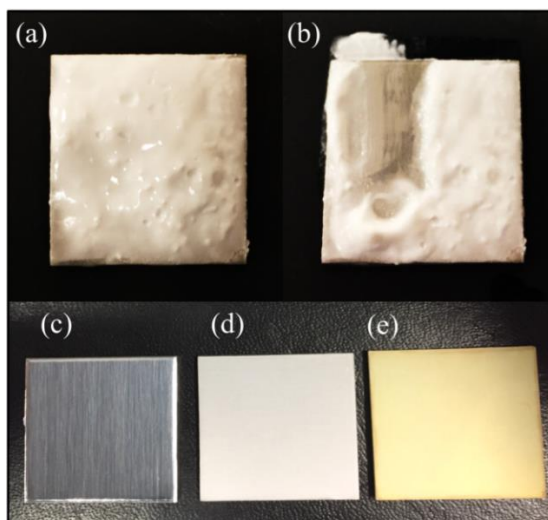


Figure S4.6. Digital photographs of (a) and (b) deposited CeOHCO_3 on top face of horizontally placed sample. (c) Bare T6-6061 AA, (d) Ce(OH)CO_3 , and (e) CeO_2 coatings.

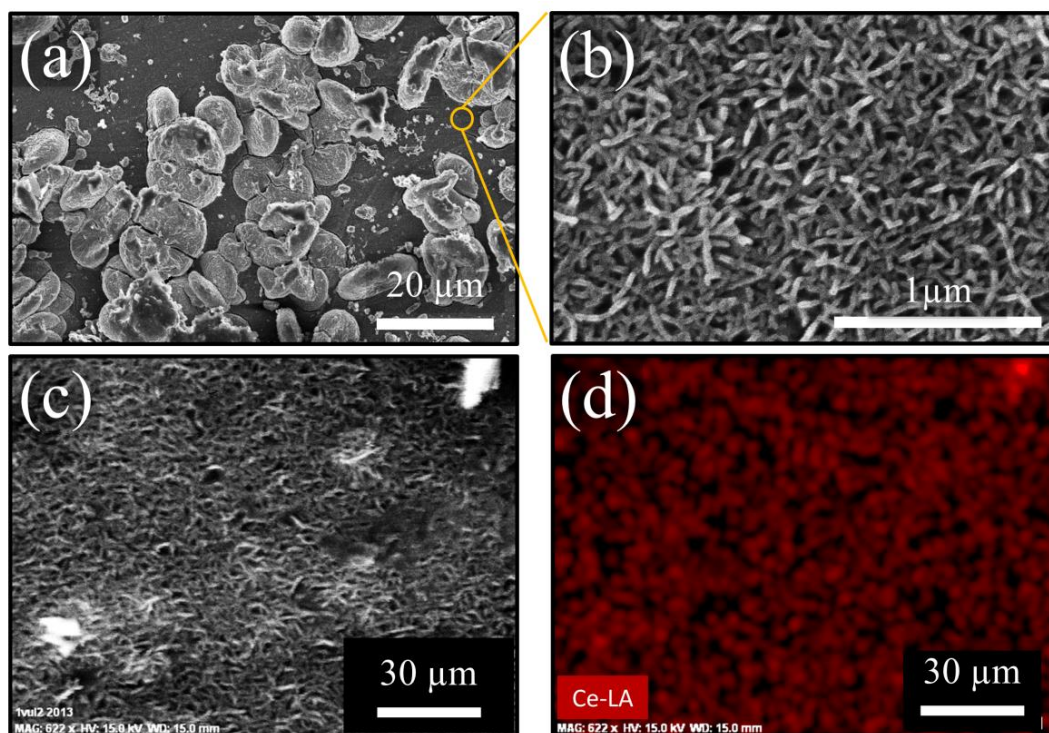


Figure S4.7. (a) and (b) The SEM image of the coating formed on top face of horizontally placed sample at different magnifications. (c) and (d) EDS Ce mapping of a place on top face of horizontally placed sample, which not covered with microstructural cerium oxide.

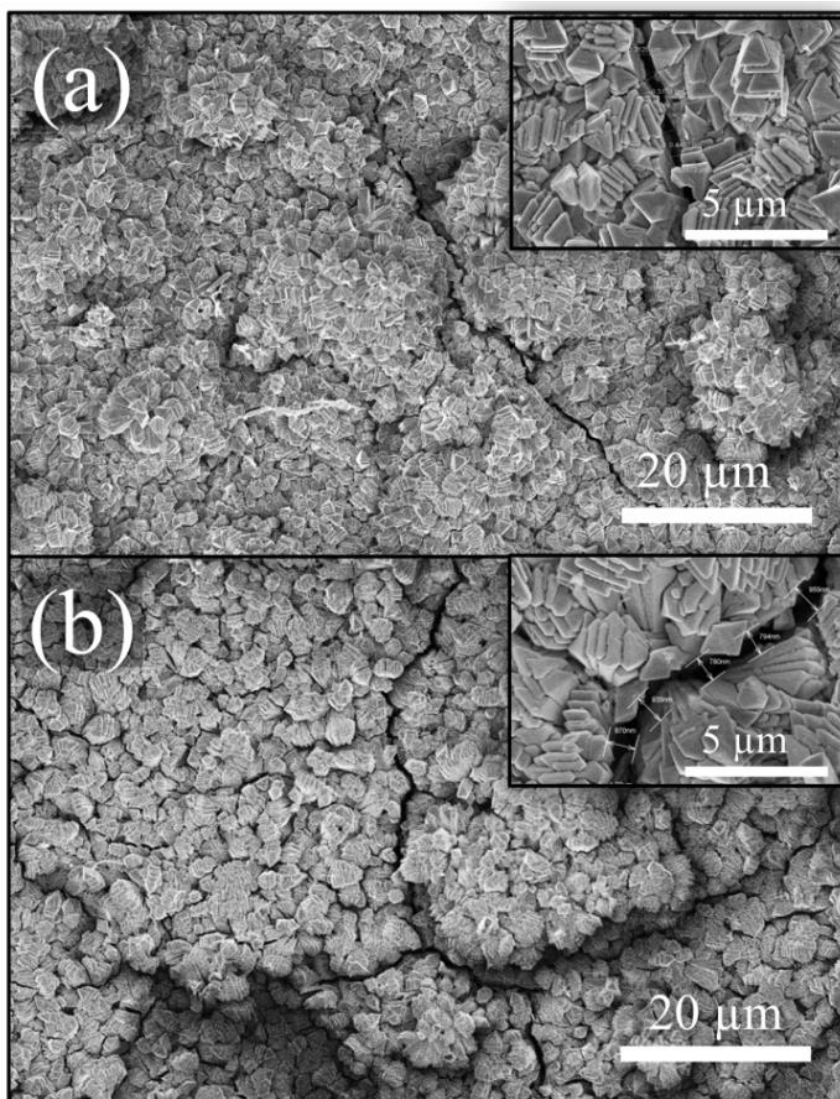


Figure S4.8. The SEM images of crack formation on S2 sample through heat treatment at (a) 250 °C and (b) 450 °C. The insets show a closer look of the cracks.

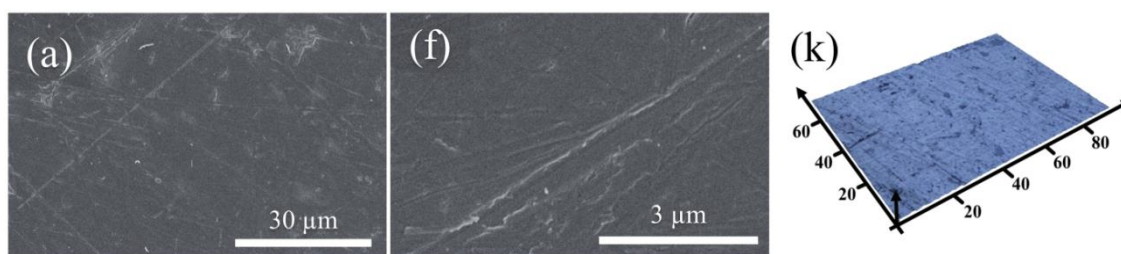


Figure S4.9. (a) Low magnification SEM image, (b) high magnification SEM image, and (c) surface 3D profile of as received T6-6061 AA.

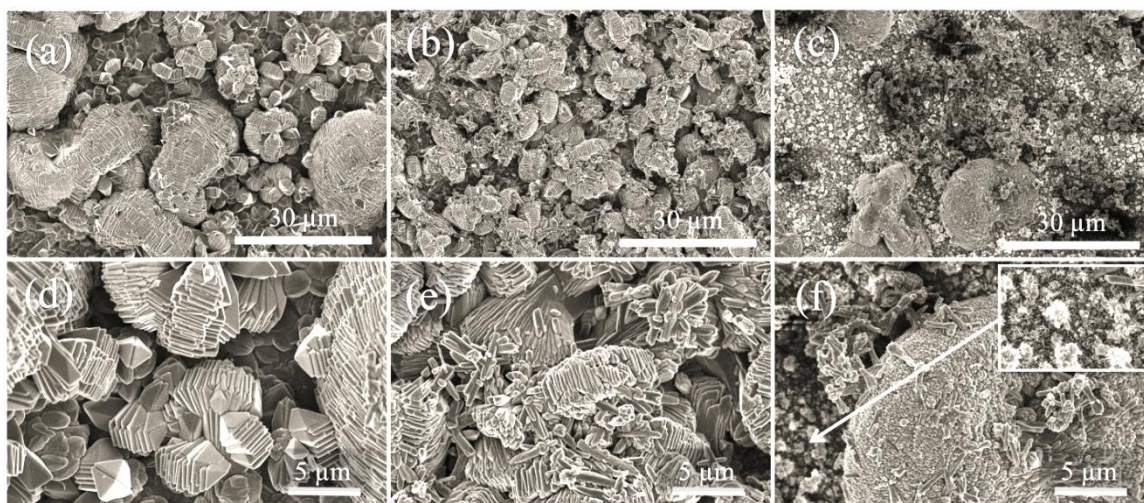


Figure S4.10. (a–c) SEM images of coatings formed at 170 °C on the bottom face of horizontally placed samples using 50, 100 and 125 mL of solution, respectively. (d–f) High magnification SEM images of (a–c), respectively. The inset shows the closer look of pointed area.

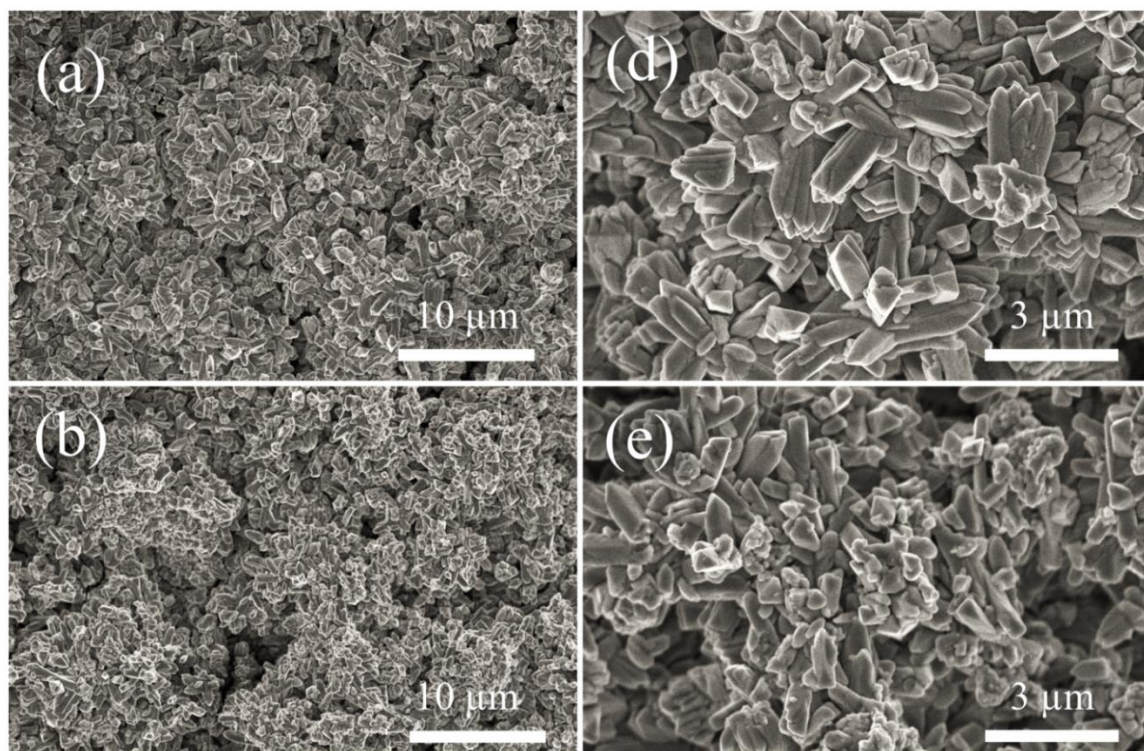


Figure S4.11. The SEM images of the S2 coating after dragging for 1.0 m over abrasive paper under (a) 3.92 KPa and (b) 4.90 KPa applied pressures. (c) and (d) the high magnification images of the (a) and (b), respectively.

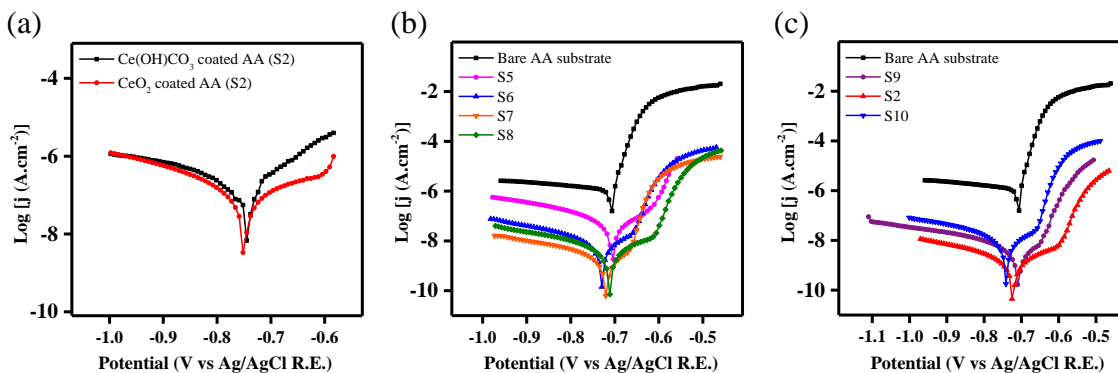


Figure S4.12. The Potentiodynamic polarization curves (Tafel plots) of (a) cerium hydroxylcarbonate and Cerium oxide coated T6-6061 AA; (b) bare and S5 to S8 coated T6-6061 AA; (c) bare, S2, S9 and S10 coated T6-6061 AA.

4.7 Author contributions

A.E. conceived the research. F.v.V. and M.B.G.J. supervised the research. A.E. fabricated the textured coatings, performed durability tests and carried out XRD, XPS, ATR-FTIR, SEM, surface wettability and 3D surface profiling characterizations. M.A. and A.E. prepared the reference electrode and conducted electrochemical corrosion measurements. V.A., M.A. and A.E. designed the corrosion cell. V.A. and A.E. manufactured the corrosion cell, performed self-cleaning tests and prepared the supplementary videos. A.E. wrote the manuscript. F.v.V., M.B.G.J. and A.E. contributed in revising the manuscript.

4.8 Acknowledgment

The authors acknowledge financial support of Natural Sciences and Engineering Research Council (NSERC) of Canada and Korea Institute of Machinery and Materials (KIMM) for the work of this paper. We thank Dr. P. Oshkai and M. Rahimpour from fluid mechanic research lab at University of Victoria for droplet impact high speed camera video recording. We thank Dr. A. Brolo for Lab access to perform

electrochemical corrosion measurement. We also thank M. Pelaschi and V. Moradi for consultation and commenting on the manuscript.

4.9 Graphical abstract

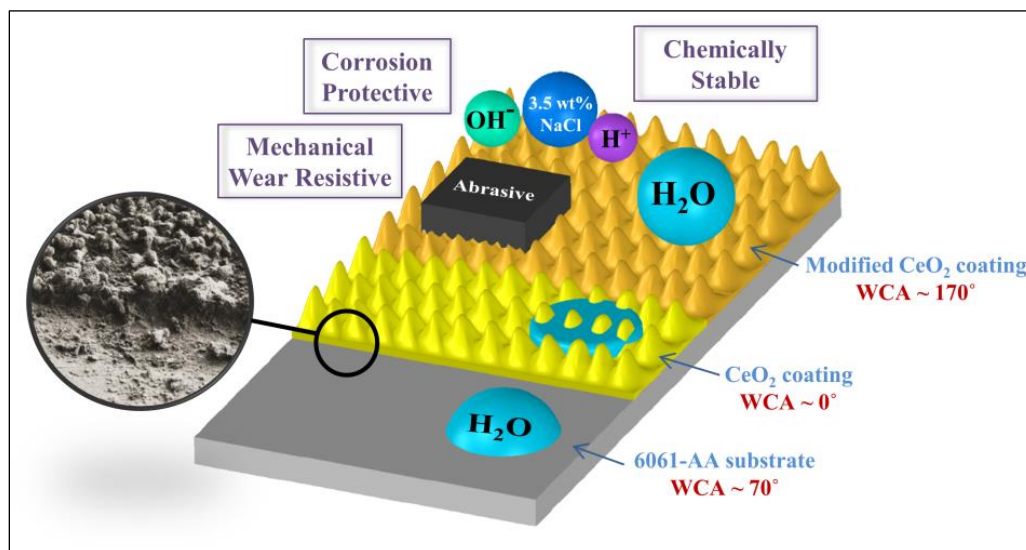


Figure 4.13. Graphical abstract of the article paper entitled “Hydrothermal Deposition of Robust Cerium Oxide Based Superhydrophobic and Corrosion Resistant Coatings on Aluminium Alloy Substrates”. The inset shows the SEM image of the cross-section view, showing a thickness of roughly 4 to 6 μm .

Chapter 5 Conclusions and Future Work

5.1 Conclusions

This dissertation presents experimental research supported by analysis for developing two different methods to create highly superhydrophobic surfaces on aluminium alloy substrates. Several challenges, mainly related to the wear resistance and chemical stability of the superhydrophobic surfaces, needed to be addressed for practical application of superhydrophobic surfaces. The motivation of this research work was to fabricate a robust superhydrophobic surface, in terms of wettability, mechanical wear-resistivity and chemical stability to serve as corrosion protective layer on aluminium alloys substrates for offshore and marine industries.

Chapter 3 presents the first method to create physically and thermally stable superhydrophobic aluminium alloy surfaces. A rough surface is formed over aluminium alloy substrate through chemical surface etching with acidic and basic solutions, follows by a surface modification with various chlorosilanes.

Chapter 4 presents the second method in which a cerium oxide coating with well-defined surface microtexture is hydrothermally deposited on aluminium alloy substrate. The superhydrophobicity of the coatings obtains by further surface modification of the coatings. The superhydrophobic cerium oxide coating exhibits remarkable wear-resistance, chemical stability and corrosion protection.

The key significant contributions of this dissertation are summarized as follows:

- 1. Direct surface acid/base etching to create desired micro-roughness on aluminium alloy for creating superhydrophobic surfaces**

A facile, practical and inexpensive chemical etching by alkaline sodium hydroxide solution, followed by a solution of acetic acid and hydrochloric acid surface treatment are used to create desired surface micro-roughness on aluminium alloys. The effect of acid solution etching time on final surface morphology and roughness of aluminium alloys substrates is also studied.

2. Investigating the impact of chlorosilane with various aliphatic chain length on resultant surface hydrophobicity

The effect of the concentration and hydrocarbon length of chlorosilanes as a low-surface-energy modifier on wettability of the etched aluminium surfaces is investigated. The modified aluminium alloy surface exhibits remarkable water-repellency with a water contact angle of about $165 \pm 2^\circ$ and a rolling angle of less than 3° , which is attributed to the combined effects of surface micro-roughness and modification with low-surface-energy modifier. The aluminium alloy surfaces preserve their superhydrophobicity up to about 375°C .

3. Promoting a controlled hydrothermal deposition process to create cerium oxide coating with various surface microtextures

A facile and highly controllable fabrication technique, including a hydrothermal deposition and further surface assembly of low-surface-energy compound, is utilized to fabricate corrosion resistance superhydrophobic coatings. The effects of sample positioning (vertical and horizontal), as well as, hydrothermal processing temperature, pressure, and heating rate on surface microfeature and roughness of the coatings are elaborately investigated. The chemical composition and surface

chemistry of the cerium oxide coatings is also studied before and after surface modification.

4. Investigating the effects of various cerium oxide coatings surface microtextures on superhydrophobic coatings wettability, and corrosion protection

Various hydrothermal processes result in cerium oxide coatings with different surface microtextures and surface roughness. The effect of coatings' morphology on wettability and corrosion protection of the aluminium alloy substrate is evaluated by contact angle measurements and potentiodynamic electrochemical measurements, respectively. A cerium oxide based coating with remarkable superhydrophobicity showing water contact angle of $170 \pm 2^\circ$ and rolling angle of $2.4 \pm 0.2^\circ$ is acquired by this method. The cerium oxide based superhydrophobic coating shows excellent corrosion resistance by decreasing the corrosion rate for approximately three orders of magnitude.

5. Evaluating the robustness of the superhydrophobic coatings

Durability of the superhydrophobic surfaces, in term of abrasion resistance and chemical and thermal stability, is an outstanding challenge for their industrial applications. The durability of the superhydrophobic aluminium alloy surface developed by direct surface etching is evaluated with regards to thermal and physical stability. The superhydrophobic aluminium alloy surface retain their non-wetting properties through heating up to 375°C , putting in ultrasonic water bath for 30 min, and immersing in water for 100 h.

On the other hand, the durability of the cerium oxide based superhydrophobic surfaces is examined regarding mechanical wear resistance and chemical stability. The surfaces preserve their non-wetting characterizations after abrasion against #800 abrasive paper for 1.0 m dragging under pressures 3.92 kPa. The coatings exhibit remarkable chemical stability in acidic and alkaline mediums over pH range of 2–13 and immersing in corrosive 3.5 % NaCl aqueous solution for 50 h. The coatings also provide an excellent corrosion protection for aluminium alloy substrate.

5.2 Future Work

Although the current approaches for developing robust superhydrophobic surfaces looks promising, the following studies and modification could be done as an extension to current research work.

- The superhydrophobic cerium oxide based coating can be implemented on different metallic substrates as corrosion protective coating.
- The effects of various hydrothermal variables, including solution concentration, urea to cerium precursor ratio, and additive on coating formation and surface morphology can be investigated.
- For further understanding the effect of surface microtexture on wetting properties of the cerium oxide based superhydrophobic coatings, the interaction of water droplet and the coatings can be modeled.
- The effect of aluminium alloy surface pretreatment and/or adding additional under layer prior to hydrothermal deposition on resultant corrosion protection can be widely investigated.

Chapter 6 Bibliography

1. *Corrosion Mechanisms in Theory and Practice*. 3rd ed.; CRC Press: **2011**; p 941.
2. Landolt, D. *Corrosion and Surface Chemistry of Metals*. CRC Press: **2007**; p 400.
3. Stansbury, E. E.; Buchanan, R. A. *Fundamentals of Electrochemical Corrosion*. ASM International: **2000**; p 487.
4. Barthlott, W.; Neinhuis, C.; Verlot, H.; Schott, C. L. Purity of the Sacred Lotus , or Escape from Contamination in Biological Surfaces. *Planta* **1997**, *202*, 1-8.
5. Pourbaix, M. Applications of Electrochemistry in Corrosion Science and in Practice. *Corros. Sci.* **1974**, *14*, 25-82.
6. Wessling, B. Passivation of Metals by Coating with Polyaniline: Corrosion Potential Shift and Morphological Changes. *Adv. Mater.* **1994**, *6*, 226-228.
7. Tang, J.; Han, Z.; Zuo, Y.; Tang, Y. A Corrosion Resistant Cerium Oxide Based Coating on Aluminum Alloy 2024 Prepared by Brush Plating. *Appl. Surf. Sci.* **2011**, *257*, 2806-2812.
8. Wang, C.; Jiang, F.; Wang, F. The Characterization and Corrosion Resistance of Cerium Chemical Conversion Coatings for 304 Stainless Steel. *Corros. Sci.* **2004**, *46*, 75-89.
9. He, T.; Wang, Y.; Zhang, Y.; Iv, Q.; Xu, T.; Liu, T. Super-Hydrophobic Surface Treatment as Corrosion Protection for Aluminum in Seawater. *Corros. Sci.* **2009**, *51*, 1757-1761.
10. Liu, C.; Su, F.; Liang, J. Facile Fabrication of a Robust and Corrosion Resistant Superhydrophobic Aluminum Alloy Surface by a Novel Method. *RSC Adv.* **2014**, *4*, 55556-55564.
11. Wong, T.-S.; Sun, T.; Feng, L.; Aizenberg, J. Interfacial Materials with Special Wettability. *MRS Bull.* **2013**, *38*, 366-371.
12. Cassie, A. B. D.; S, B. Wettability of Porous Surfaces. *Transactions of the Faraday Society* **1944**, 546-551.
13. Patankar, N. A. Mimicking the Lotus Effect: Influence of Double Roughness Structures and Slender Pillars. *Langmuir* **2004**, *20*, 8209-8213.
14. Li, W.; Kang, Z. Fabrication of Corrosion Resistant Superhydrophobic Surface with Self-Cleaning Property on Magnesium Alloy and its Mechanical Stability. *Surf. Coat. Technol.* **2014**, *253*, 205-213.
15. Subhash Latthe, S. Recent Progress in Preparation of Superhydrophobic Surfaces: A Review. *J. Surf. Eng. Adv. Technol.* **2012**, *2*, 76-94.

16. Kendig, M. W.; Davenport, A. J.; Isaacs, H. S. The Mechanism of Corrosion Inhibition by Chromate Conversion Coatings from X-Ray Absorption Near Edge Spectroscopy (Xanes). *Corros. Sci.* **1993**, *34*, 41-49.
17. Lunder, O.; Walmsley, J. C.; Mack, P.; Nisancioglu, K. Formation and Characterisation of a Chromate Conversion Coating on AA6060 Aluminium. *Corros. Sci.* **2005**, *47*, 1604-1624.
18. Holland, S. L.; Avery, S. V. Chromate Toxicity and the Role of Sulfur. *Metallomics* **2011**, *3*, 1119-1123.
19. Kuzenkov, Y. A.; Oleinik, S. V.; Karimova, S. A.; Pavlovskaya, T. G. Chromate-free Conversion Coatings on 1370 Aluminum Alloy. *Prot. Met. Phys. Chem. Surfaces* **2012**, *48*, 784-789.
20. Liu, C.-n.; Wiesener, M.; Giner, I.; Grundmeier, G. Structure and Corrosion Resistance of Cerium-Oxide Films on AZ31 as Deposited by High-Power Ultrasound Supported Conversion Chemistry. *Front. Mater.* **2015**, *2*, 1-10.
21. Conde, a.; Arenas, M. a.; de Frutos, a.; de Damborenea, J. Effective Corrosion Protection of 8090 Alloy by Cerium Conversion Coatings. *Electrochim. Acta* **2008**, *53*, 7760-7768.
22. Nazeri, A.; Trzaskoma-Paulette, P. P.; Bauer, D. Synthesis and Properties of Cerium and Titanium Oxide Thin Coatings for Corrosion Protection of 304 Stainless Steel. *J. Sol-Gel Sci. Technol.* **1997**, *10*, 317-331.
23. Rudd, A. L.; Breslin, C. B.; Mansfeld, F. The Corrosion Protection Afforded by Rare Earth Conversion Coatings Applied to Magnesium. *Corros. Sci.* **2000**, *42*, 275-288.
24. Cui, X.; Yang, Y.; Liu, E.; Jin, G.; Zhong, J.; Li, Q. Corrosion Behaviors in Physiological Solution of Cerium Conversion Coatings on AZ31 Magnesium Alloy. *Appl. Surf. Sci.* **2011**, *257*, 9703-9709.
25. Zheng, S.; Li, C.; Fu, Q.; Li, M.; Hu, W.; Wang, Q.; Du, M.; Liu, X.; Chen, Z. Fabrication of Self-Cleaning Superhydrophobic Surface on Aluminum Alloys with Excellent Corrosion Resistance. *Surf. Coat. Technol.* **2015**, *276*, 341-348.
26. Esmaeilirad, A.; Rukosuyev, M. V.; Jun, M. B. G.; van Veggel, F. C. J. M. A Cost-Effective Method to Create Physically and Thermally Stable and Storable Super-Hydrophobic Aluminum Alloy Surfaces. *Surf. Coat. Technol.* **2016**, *285*, 227-234.
27. Castano, C. E.; O'Keefe, M. J.; Fahrenholtz, W. G. Cerium-Based Oxide Coatings. *Curr. Opin. Solid State Mater. Sci.* **2015**, *19*, 69-76.
28. Schem, M.; Schmidt, T.; Gerwahn, J.; Wittmar, M.; Veith, M.; Thompson, G. E.; Molchan, I. S.; Hashimoto, T.; Skeldon, P.; Phani, a. R.; Santucci, S.; Zheludkevich, M. L. CeO₂-Filled Sol-Gel Coatings for Corrosion Protection of AA2024-T3 Aluminium Alloy. *Corros. Sci.* **2009**, *51*, 2304-2315.
29. Golden, T. D.; Wang, A. Q. Anodic Electrodeposition of Cerium Oxide Thin Films. *J. Electrochem. Soc.* **2003**, *150*, 616-621.

30. Suh, S.; Guan, J.; Mîinea, L. A.; Lehn, J.-S. M.; Hoffman, D. M. Chemical Vapor Deposition of Cerium Oxide Films from a Cerium Alkoxide Precursor. *Chem. Mater.* **2004**, *16*, 1667-1673.
31. Zhang, K.; Wu, J.; Chu, P.; Ge, Y.; Zhao, R.; Li, X. A Novel CVD Method for Rapid Fabrication of Superhydrophobic Surface on Aluminum Alloy Coated Nanostructured Cerium-Oxide and Its Corrosion Resistance. *Int. J. Electrochem. Sci.* **2015**, *10*, 6257-6272.
32. Yu, R.; Yan, L.; Zheng, P.; Chen, J.; Xing, X. Controlled Synthesis of CeO₂ Flower-Like and Well-Aligned Nanorod Hierarchical Architectures by a Phosphate-Assisted Hydrothermal Route. *J. Phys. Chem. C* **2008**, *112*, 19896-19900.
33. Hirano, M.; Kato, E. Hydrothermal Synthesis of Cerium(IV) Oxide. *J. Am. Ceram. Soc.* **2005**, *79*, 777-780.
34. Cho, Y. J.; Jang, H.; Lee, K.-S.; Kim, D. R. Direct Growth of Cerium Oxide Nanorods on Diverse Substrates for Superhydrophobicity and Corrosion Resistance. *Appl. Surf. Sci.* **2015**, *340*, 96-101.
35. Li, L.; Huang, T.; Lei, J.; He, J.; Qu, L.; Huang, P.; Zhou, W.; Li, N.; Pan, F. Robust Biomimetic-Structural Superhydrophobic Surface on Aluminum Alloy. *ACS Appl. Mater. Interfaces* **2015**, *7*, 1449-1457.
36. Lee, S. H.; Saito, Y.; Sakai, T.; Utsunomiya, H. Microstructures and Mechanical Properties of 6061 Aluminum Alloy Processed by Accumulative Roll-Bonding. *Mater. Sci. Eng., A* **2002**, *325*, 228-235.
37. Ouyang, J.; Yarrapareddy, E.; Kovacevic, R. Microstructural Evolution in the Friction Stir Welded 6061 Aluminum Alloy (T6-Temper Condition) to Copper. *J. Mater. Process. Technol.* **2006**, *172*, 110-122.
38. Gao, X.; Jiang, L. Biophysics: Water-repellent legs of water striders. *Nature* **2004**, *432*, 36-37.
39. Hu, D. L.; Bush, J. W. M. Meniscus-climbing insects. *Nature* **2005**, *437*, 733-7366.
40. Feng, L.; Li, S.; Li, Y.; Li, H.; Zhang, L.; Zhai, J.; Song, Y.; Liu, B.; Jiang, L.; Zhu, D. Super-Hydrophobic Surfaces: From Natural to Artificial. *Adv. Mater.* **2002**, *14*, 1857-1860.
41. Gao, X.; Yan, X.; Yao, X.; Xu, L.; Zhang, K.; Zhang, J.; Yang, B.; Jiang, L. The Dry-Style Antifogging Properties of Mosquito Compound Eyes and Artificial Analogues Prepared by Soft Lithography. *Adv. Mater.* **2007**, *19*, 2213-2217.
42. Liu, H.; Szunerits, S.; Xu, W.; Boukherroub, R. Preparation of Superhydrophobic Coatings on Zinc as Effective Corrosion Barriers. *ACS Appl. Mater. Interfaces* **2009**, *1*, 1150-1153.
43. Aljallis, E.; Sarshar, M. A.; Datla, R.; Sikka, V.; Jones, A.; Choi, C.-H. Experimental Study of Skin Friction Drag Reduction on Superhydrophobic Flat Plates in High Reynolds Number Boundary Layer Flow. *Phys. Fluids* **2013**, *25*, 025103.

44. Miljkovic, N.; Enright, R.; Wang, E. N. Effect of Droplet Morphology on Growth Dynamics and Heat Transfer during Condensation on Superhydrophobic Nanostructured Surfaces. *ACS Nano* **2012**, *6*, 1776-1785.
45. Ruan, M.; Li, W.; Wang, B.; Deng, B.; Ma, F.; Yu, Z. Preparation and Anti-Icing Behavior of Superhydrophobic Surfaces on Aluminum Alloy Substrates. *Langmuir* **2013**, *29*, 8482-8491.
46. Nakajima, A.; Hashimoto, K.; Watanabe, T.; Takai, K.; Yamauchi, G.; Fujishima, A. Transparent Superhydrophobic Thin Films with Self-Cleaning Properties. *Langmuir* **2000**, *16*, 7044-7047.
47. Fürstner, R.; Barthlott, W.; Neinhuis, C.; Walzel, P. Wetting and Self-Cleaning Properties of Artificial Superhydrophobic Surfaces. *Langmuir* **2005**, *21*, 956-961.
48. Anderson, W. Wettability Literature Survey- Part 2: Wettability Measurement. *J. Petrol. Technol.* **1986**, *38*, 1246-1262.
49. Kwok, D. Y.; Neumann, A. W. Contact Angle Measurement and Contact Angle Interpretation. *Adv. Colloid Interface Sci.* **1999**, *81*, 167-249.
50. Joanny, J. F.; de Gennes, P. G. A Model for Contact Angle Hysteresis. *J. Chem. Phys.* **1984**, *81*, 552-562.
51. Thompson, P. A.; Robbins, M. O. Simulations of Contact-Line Motion: Slip and the Dynamic Contact Angle. *Phys. Rev. Lett.* **1989**, *63*, 766-769.
52. Tian, Y.; Jiang, L. Wetting, Intrinsically Robust Hydrophobicity. *Nat. Mater.* **2013**, *12*, 291-292.
53. Genzer, J.; Efimenko, K. Recent Developments in Superhydrophobic Surfaces and Their Relevance to Marine Fouling: A Review. *Biofouling* **2006**, *22*, 339-360.
54. Antonini, C.; Innocenti, M.; Horn, T.; Marengo, M.; Amirfazli, A. Understanding the Effect of Superhydrophobic Coatings on Energy Reduction in Anti-Icing Systems. *Cold. Reg. Sci. Technol.* **2011**, *67*, 58-67.
55. Wenzel, R. N. Resistance of Solid Surfaces to Wetting by Water. *Ind. Eng. Chem. Res.* **1936**, *28*, 988-994.
56. Patankar, N. A. On the Modeling of Hydrophobic Contact Angles on Rough Surfaces. *Langmuir* **2003**, *19*, 1249-1253.
57. R.R.L. De Oliveira; D.A.C. Albuquerque; T.G.S. Cruz; Yamaji, F. M.; Leite, a. F. L. *Atomic Force Microscopy - Imaging, Measuring and Manipulating Surfaces at the Atomic Scale*. InTech: **2012**; p 268.
58. Lafuma, A.; Quéré, D. Superhydrophobic States. *Nat. Mater.* **2003**, *2*, 457-460.
59. Koishi, T.; Yasuoka, K.; Fujikawa, S.; Ebisuzaki, T.; Zeng, X. C. Coexistence and Transition between Cassie and Wenzel State on Pillared Hydrophobic Surface. *Proc. Natl. Acad. Sci. U S A* **2009**, *106*, 8435-8440.

60. Feng, L.; Zhang, H.; Wang, Z.; Liu, Y. Superhydrophobic Aluminum Alloy Surface: Fabrication, Structure, and Corrosion Resistance. *Colloids Surf., A* **2014**, *441*, 319-325.
61. Giovambattista, N.; Debenedetti, P. G.; Rossky, P. J. Effect of Surface Polarity on Water Contact Angle and Interfacial Hydration Structure. *J. Phys. Chem. B* **2007**, *111*, 9581-9587.
62. Guo, Z.; Liang, J.; Fang, J.; Guo, B.; Liu, W. A Novel Approach to the Robust Ti6Al4V-Based Superhydrophobic Surface with Crater-like Structure. *Adv. Eng. Mater.* **2007**, *9*, 316-321.
63. Liu, Y.; Tang, J.; Wang, R.; Lu, H.; Li, L.; Kong, Y.; Qi, K.; Xin, J. H. Artificial Lotus Leaf Structures from Assembling Carbon Nanotubes and their Applications in Hydrophobic Textiles. *J. Mater. Chem.* **2007**, *17*, 1071-1078.
64. Minko, S.; Müller, M.; Motornov, M.; Nitschke, M.; Grundke, K.; Stamm, M. Two-Level Structured Self-Adaptive Surfaces with Reversibly Tunable Properties. *J. Am. Chem. Soc.* **2003**, *125*, 3896-3900.
65. Olde Riekerink, M. B.; Terlingen, J. G. A.; Engbers, G. H. M.; Feijen, J. Selective Etching of Semicrystalline Polymers: CF₄ Gas Plasma Treatment of Poly(ethylene). *Langmuir* **1999**, *15*, 4847-4856.
66. Fadeeva, E.; Truong, V. K.; Stiesch, M.; Chichkov, B. N.; Crawford, R. J.; Wang, J.; Ivanova, E. P. Bacterial Retention on Superhydrophobic Titanium Surfaces Fabricated by Femtosecond Laser Ablation. *Langmuir* **2011**, *27*, 3012-3019.
67. Wang, Y.; Liu, X. W.; Zhang, H. F.; Zhou, Z. P. Fabrication of Superhydrophobic Surfaces on Aluminum Alloy Substrates by RF-Sputtered Polytetrafluoroethylene Coatings. *AIP Adv.* **2014**, *4*, 031323.
68. Saleema, N.; Sarkar, D. K.; Paynter, R. W.; Chen, X. G. Superhydrophobic Aluminum Alloy Surfaces by a Novel One-Step Process. *ACS Appl. Mater. Interfaces* **2010**, *2*, 2500-2502.
69. Saleema, N.; Sarkar, D. K.; Gallant, D.; Paynter, R. W.; Chen, X. G. Chemical Nature of Superhydrophobic Aluminum Alloy Surfaces Produced via a One-Step Process Using Fluoroalkyl-Silane in a Base Medium. *ACS Appl. Mater. Interfaces* **2011**, *3*, 4775-4781.
70. Hosono, E.; Fujihara, S.; Honma, I.; Zhou, H. Superhydrophobic Perpendicular Nanopin Film by the Bottom-up Process. *J. Am. Chem. Soc.* **2005**, *127*, 13458-13459.
71. Yu, J.; Qin, L.; Hao, Y.; Kuang, S.; Bai, X.; Chong, Y.-M.; Zhang, W.; Wang, E. Vertically Aligned Boron Nitride Nanosheets: Chemical Vapor Synthesis, Ultraviolet Light Emission, and Superhydrophobicity. *ACS Nano* **2010**, *4*, 414-422.
72. Tu, C.-W.; Tsai, C.-H.; Wang, C.-F.; Kuo, S.-W.; Chang, F.-C. Fabrication of Superhydrophobic and Superoleophilic Polystyrene Surfaces by a Facile One-Step Method. *Macromol. Rapid Commun.* **2007**, *28*, 2262-2266.

73. Zhao, N.; Shi, F.; Wang, Z.; Zhang, X. Combining Layer-by-Layer Assembly with Electrodeposition of Silver Aggregates for Fabricating Superhydrophobic Surfaces. *Langmuir* **2005**, *21*, 4713-4716.
74. Tadanaga, K.; Katata, N.; Minami, T. Formation Process of Super-Water-Repellent Al₂O₃ Coating Films with High Transparency by the Sol-Gel Method. *J. Am. Ceram. Soc.* **2005**, *80*, 3213-3216.
75. Rao, A. V.; Latthe, S. S.; Kappenstein, C.; Ganesan, V.; Rath, M. C.; Sawant, S. N. Wetting Behavior of High Energy Electron Irradiated Porous Superhydrophobic Silica Films. *Appl. Surf. Sci.* **2011**, *257*, 3027-3032.
76. Nakajima, A.; Abe, K.; Hashimoto, K.; Watanabe, T. Preparation of Hard Super-Hydrophobic Films with Visible Light Transmission. *Thin Solid Films* **2000**, *376*, 140-143.
77. Liang, J.; Hu, Y.; Wu, Y.; Chen, H. Fabrication and Corrosion Resistance of Superhydrophobic Hydroxide Zinc Carbonate Film on Aluminum Substrates. *J. Nanomater.* **2013**, *2013*, 1-6.
78. Mahadik, S. a.; Fernando, P. D.; Hegade, N. D.; Wagh, P. B.; Gupta, S. C. Durability and Restoring of Superhydrophobic Properties in Silica-Based Coatings. *J. Colloid Interface Sci.* **2013**, *405*, 262-268.
79. Campos, R.; Guenther, A. J.; Haddad, T. S.; Mabry, J. M. Fluoroalkyl-Functionalized Silica Particles: Synthesis, Characterization, and Wetting Characteristics. *Langmuir* **2011**, *27*, 10206-10215.
80. Latthe, S. S.; Imai, H.; Ganesan, V.; Rao, A. V. Superhydrophobic Silica Films by Sol-Gel Co-Precursor Method. *Appl. Surf. Sci.* **2009**, *256*, 217-222.
81. Aytug, T.; Simpson, J. T.; Lupini, A. R.; Trejo, R. M.; Jellison, G. E.; Ivanov, I. N.; Pennycook, S. J.; Hillesheim, D. a.; Winter, K. O.; Christen, D. K.; Hunter, S. R.; Haynes, J. A. Optically Transparent, Mechanically Durable, Nanostructured Superhydrophobic Surfaces Enabled by Spinodally Phase-Separated Glass Thin Films. *Nanotechnology* **2013**, *24*, 315602.
82. Ishizaki, T.; Masuda, Y.; Sakamoto, M. Corrosion Resistance and Durability of Superhydrophobic Surface Formed on Magnesium Alloy Coated with Nanostructured Cerium Oxide Film and Fluoroalkylsilane Molecules in Corrosive NaCl Aqueous Solution. *Langmuir* **2011**, *27*, 4780-4788.
83. Boinovich, L.; Emelyanenko, A. M.; Pashinin, A. S. Analysis of Long-Term Durability of Superhydrophobic Properties under Continuous Contact with Water. *ACS Appl. Mater. Interfaces* **2010**, *2*, 1754-1758.
84. Verho, T.; Bower, C.; Andrew, P.; Franssila, S.; Ikkala, O.; Ras, R. H. a. Mechanically Durable Superhydrophobic Surfaces. *Adv. Mater.* **2011**, *23*, 673-678.
85. Patsalas, P.; Logothetidis, S.; Sygellou, L.; Kennou, S. Structure-Dependent Electronic Properties of Nanocrystalline Cerium Oxide Films. *Phys. Rev. B* **2003**, *68*, 035104.

86. Zhang, F.; Chan, S.-W.; Spanier, J. E.; Apak, E.; Jin, Q.; Robinson, R. D.; Herman, I. P. Cerium Oxide Nanoparticles: Size-Selective Formation and Structure Analysis. *Appl. Phys. Lett.* **2002**, *80*, 127-127.
87. Imanaka, N.; Masui, T.; Hirai, H.; Adachi, G.-y. Amorphous Cerium–Titanium Solid Solution Phosphate as a Novel Family of Band Gap Tunable Sunscreen Materials. *Chem. Mater.* **2003**, *15*, 2289-2291.
88. Hass, G.; Ramsey, J. B.; Thun, R. Optical Properties and Structure of Cerium Dioxide Films. *J. Opt. Soc. Am.* **1958**, *48*, 324-327.
89. Creaser, D. A.; Harrison, P. G.; Morris, M. A.; Wolfindale, B. A. X-ray Photoelectron Spectroscopic Study of the Oxidation and Reduction of a Cerium(III) Oxide/Cerium Foil Substrate. *Catal. Lett.* **1994**, *23*, 13-24.
90. Hay, P. J.; Martin, R. L.; Uddin, J.; Scuseria, G. E. Theoretical Study of CeO_2 and Ce_2O_3 Using a Screened Hybrid Density Functional. *J. Chem. Phys.* **2006**, *125*, 34712.
91. Yabe, S. Cerium Oxide for Sunscreen Cosmetics. *J. Solid State Chem.* **2003**, *171*, 7-11.
92. Cao, X. Q.; Vassen, R.; Stoever, D. Ceramic Materials for Thermal Barrier Coatings. *J. Eur. Ceram. Soc.* **2004**, *24*, 1-10.
93. Preston, D. J.; Miljkovic, N.; Sack, J.; Enright, R.; Queeney, J.; Wang, E. N. Effect of Hydrocarbon Adsorption on the Wettability of Rare Earth Oxide Ceramics. *Appl. Phys. Lett.* **2014**, *105*, 011601.
94. Suda, S. Nanocomposite Glass Abrasives. *J. Ceram. Soc. Jpn.* **2014**, *122*, 244-249.
95. Corma, A.; Atienzar, P.; García, H.; Chane-Ching, J.-Y. Hierarchically Mesoporous Doped CeO_2 with Potential for Solar-Cell Use. *Nat. Mater.* **2004**, *3*, 394-397.
96. Lawrence, N. J.; Brewer, J. R.; Wang, L.; Wu, T.-S.; Wells-Kingsbury, J.; Ihrig, M. M.; Wang, G.; Soo, Y.-L.; Mei, W.-N.; Cheung, C. L. Defect Engineering in Cubic Cerium Oxide Nanostructures for Catalytic Oxidation. *Nano Lett.* **2011**, *11*, 2666-2671.
97. Harvey, T. G. Cerium-based Conversion Coatings on Aluminium Alloys: A Process Review. *Corros. Eng. Sci. Tech.* **2013**, *48*, 248-269.
98. Ganduglia-Pirovano, M. V.; Hofmann, A.; Sauer, J. Oxygen Vacancies in Transition Metal and Rare Earth Oxides: Current State of Understanding and Remaining Challenges. *Surf. Sci. Rep.* **2007**, *62*, 219-270.
99. Fernández-García, M.; Martínez-Arias, A.; Hanson, J. C.; Rodríguez, J. A. Nanostructured oxides in Chemistry: Characterization and Properties. *Chem. Rev.* **2004**, *104*, 4063-4104.
100. Azimi, G.; Dhiman, R.; Kwon, H.-M.; Paxson, A. T.; Varanasi, K. K. Hydrophobicity of Rare-Earth Oxide Ceramics. *Nat. Mater.* **2013**, *12*, 315-320.

101. Kendig, M.; Jeanjaquet, S.; Addison, R.; Waldrop, J. Role of Hexavalent Chromium in the Inhibition of Corrosion of Aluminum Alloys. *Surf. Coat. Technol.* **2001**, *140*, 58-66.
102. Zhang, H.; Yao, G.; Wang, S.; Liu, Y.; Luo, H. A Chrome-Free Conversion Coating for Magnesium–Lithium Alloy by a Phosphate–Permanganate Solution. *Surf. Coat. Technol.* **2008**, *202*, 1825-1830.
103. Thanneeru, R.; Patil, S.; Deshpande, S.; Seal, S. Effect of Trivalent Rare Earth Dopants in Nanocrystalline Ceria Coatings for High-Temperature Oxidation Resistance. *Acta Mater.* **2007**, *55*, 3457-3466.
104. Khan, S.; Azimi, G.; Yildiz, B.; Varanasi, K. K.; Khan, S.; Azimi, G.; Yildiz, B.; Varanasi, K. K. Role of Surface Oxygen-to-Metal Ratio on the Wettability of Rare-Earth Oxides. *Appl. Phys. Lett.* **2015**, *106*, 061601.
105. Meléndez-Ceballos, A.; Albin, V.; Fernández-Valverde, S. M.; Ringuedé, A.; Cassir, M. Electrochemical Properties of Atomic Layer Deposition Processed CeO₂ as a Protective Layer for the Molten Carbonate Fuel Cell Cathode. *Electrochim. Acta* **2014**, *140*, 174-181.
106. Mansilla, C. Structure, Microstructure and Optical Properties of Cerium Oxide Thin Films Prepared by Electron Beam Evaporation Assisted with Ion Beams. *Solid State Sci.* **2009**, *11*, 1456-1464.
107. Ji, Z.; Wang, X.; Zhang, H.; Lin, S.; Meng, H.; Sun, B.; George, S.; Xia, T.; Nel, A. E.; Zink, J. I. Designed Synthesis of CeO₂ Nanorods and Nanowires for Studying Toxicological Effects of High Aspect Ratio Nanomaterials. *ACS Nano* **2012**, *6*, 5366-5380.
108. Joo, J.; Chow, B. Y.; Prakash, M.; Boyden, E. S.; Jacobson, J. M. Face-selective Electrostatic Control of Hydrothermal Zinc Oxide Nanowire Synthesis. *Nat. Mater.* **2011**, *10*, 596-601.
109. Laberty-Robert, C.; Long, J. W.; Lucas, E. M.; Pettigrew, K. A.; Stroud, R. M.; Doescher, M. S.; Rolison, D. R. Sol–Gel-Derived Ceria Nanoarchitectures: Synthesis, Characterization, and Electrical Properties. *Chem. Mater.* **2006**, *18*, 50-58.
110. Kumar, A.; Babu, S.; Karakoti, A. S.; Schulte, A.; Seal, S. Luminescence Properties of Europium-Doped Cerium Oxide Nanoparticles: Role of Vacancy and Oxidation States. *Langmuir* **2009**, *25*, 10998-11007.
111. Wu, Q.; Zhang, F.; Xiao, P.; Tao, H.; Wang, X.; Hu, Z.; Lü, Y. Great Influence of Anions for Controllable Synthesis of CeO₂ Nanostructures: From Nanorods to Nanocubes. *J. Phys. Chem. C* **2008**, *112*, 17076-17080.
112. Mai, H.-X.; Sun, L.-D.; Zhang, Y.-W.; Si, R.; Feng, W.; Zhang, H.-P.; Liu, H.-C.; Yan, C.-H. Shape-Selective Synthesis and Oxygen Storage Behavior of Ceria Nanopolyhedra, Nanorods, and Nanocubes. *J. Phys. Chem. B* **2005**, *109*, 24380-24385.

113. Pan, C.; Zhang, D.; Shi, L.; Fang, J. Template-Free Synthesis, Controlled Conversion, and CO Oxidation Properties of CeO₂ Nanorods, Nanotubes, Nanowires, and Nanocubes. *Eur. J. Inorg. Chem.* **2008**, 2008, 2429-2436.
114. Liu, C.; Su, F.; Liang, J.; Huang, P. Facile Fabrication of Superhydrophobic Cerium Coating with Micro-Nano Flower-Like Structure and Excellent Corrosion Resistance. *Surf. Coat. Technol.* **2014**, 258, 580-586.
115. Liang, J.; Hu, Y.; Fan, Y.; Chen, H. Formation of Superhydrophobic Cerium Oxide Surfaces on Aluminum Substrate and its Corrosion Resistance Properties. *Surf. Interface Anal.* **2013**, 45, 1211-1216.
116. Xue, M.; Peng, N.; Ou, J.; Wang, F.; Li, X.; Li, W. Hierarchically Nanostructured CeO₂ Films with Superhydrophilicity and Corrosion Resistance by Coupling of Surface Topography and Oxygen Vacancies. *Mater. Chem. Phys.* **2015**, 160, 406-412.
117. Szklarska-Smialowska, Z. Insight into the Pitting Corrosion Behaviour of Aluminium Alloys. *Corros. Sci.* **1992**, 33, 1193-1202.
118. Shi, Z.; Liu, M.; Atrens, A. Measurement of the Corrosion Rate of Magnesium Alloys Using Tafel Extrapolation. *Corros. Sci.* **2010**, 52, 579-588.
119. McCafferty, E. Validation of Corrosion Rates Measured by the Tafel Extrapolation Method. *Corros. Sci.* **2005**, 47, 3202-3215.
120. Barthlott, W.; Neinhuis, C. Purity of the Sacred Lotus, or Escape from Contamination in Biological Surfaces. *Planta* **1997**, 202, 1-8.
121. Wenzel, R. N. Resistance of Solid Surfaces. *Ind. Eng. Chem. Res.* **1936**, 28, 988-994.
122. Shang, H. M.; Wang, Y.; Limmer, S. J.; Chou, T. P.; Takahashi, K.; Cao, G. Z. Optically Transparent Superhydrophobic Silica-Based Films. *Thin Solid Films* **2005**, 472, 37-43.
123. Yang, J.; Zhang, Z.; Xu, X.; Men, X.; Zhu, X.; Zhou, X. Superoleophobic Textured Aluminum Surfaces. *New J. Chem.* **2011**, 35, 2422-2422.
124. Chen, W.; Fadeev, A. Y.; Hsieh, M. C.; Didem, O.; Youngblood, J.; McCarthy, T. J. Ultrahydrophobic and Ultralyophobic Surfaces: Some Comments and Examples. *Langmuir* **1999**, 3395-3399.
125. Wang, F.; Li, C.; Lv, Y.; Lv, F.; Du, Y. Ice Accretion on Superhydrophobic Aluminum Surfaces under Low-Temperature Conditions. *Cold. Reg. Sci. Technol.* **2010**, 62, 29-33.
126. Huang, Q.; Lin, L.; Yang, Y.; Hu, R.; Vogler, E. A.; Lin, C. Role of Trapped Air in the Formation of Cell-and-Protein Micropatterns on Superhydrophobic/Superhydrophilic Microtemplated Surfaces. *Biomaterials* **2012**, 33, 8213-20.

127. Wang, F.; Lv, F.; Liu, Y.; Li, C.; Lv, Y. Ice Adhesion on Different Microstructure Superhydrophobic Aluminum Surfaces. *J. Adhes. Sci. Technol.* **2013**, *27*, 58-67.
128. Jung, S.; Dorrestijn, M.; Raps, D.; Das, A.; Megaridis, C. M.; Poulikakos, D. Are Superhydrophobic Surfaces Best for Icephobicity? *Langmuir* **2011**, *27*, 3059-3066.
129. Samaha, M. A.; Tafreshi, H. V.; Gad-el-Hak, M. Superhydrophobic Surfaces: From the Lotus Leaf to the Submarine. *C. R. Acad. Sci.* **2012**, *340*, 18-34.
130. Wang, H.; Dai, D.; Wu, X. Fabrication of Superhydrophobic Surfaces on Aluminum. *Appl. Surf. Sci.* **2008**, *254*, 5599-5601.
131. Yang, Z.; Wu, Y.-Z.; Ye, Y.-F.; Gong, M.-G.; Xu, X.-L. A Simple Way to Fabricate an Aluminum Sheet with Superhydrophobic and Self-Cleaning Properties. *Chin. Phys. B* **2012**, *21*, 126801.
132. Liang, J.; Hu, Y.; Wu, Y.; Chen, H. Facile Formation of Superhydrophobic Silica-Based Surface on Aluminum Substrate with Tetraethylorthosilicate and Vinyltriethoxysilane as Co-Precursor and its Corrosion Resistant Performance in Corrosive NaCl Aqueous Solution. *Surf. Coat. Technol.* **2014**, *240*, 145-153.
133. Liu, W.; Luo, Y.; Sun, L.; Wu, R.; Jiang, H.; Liu, Y. Fabrication of the Superhydrophobic Surface on Aluminum Alloy by Anodizing and Polymeric coating. *Appl. Surf. Sci.* **2013**, *264*, 872-878.
134. Chen, Z.; Guo, Y.; Fang, S. A Facile Approach to Fabricate Superhydrophobic Aluminum Surface. *Surf. Interface Anal.* **2009**, *42*, 1-6.
135. Leyden, D. E.; Shreedhara, R. S.; Atwater, J. B.; Blitz, J. P. Studies of Alkoxysilane Hydrolysis and Condensation by Fourier-Transform Infrared Spectroscopy with a Cylindrical Internal-Reflection Cell. *Anal. Chim. Acta* **1987**, *200*, 459-468.
136. Yang, J.; Pi, P.; Wen, X.; Zheng, D.; Xu, M.; Cheng, J.; Yang, Z. A Novel Method to Fabricate Superhydrophobic Surfaces Based on Well-Defined Mulberry-Like Particles and Self-Assembly of Polydimethylsiloxane. *Appl. Surf. Sci.* **2009**, *255*, 3507-3512.
137. Wang, R.; Liu, H.; Wang, F. Facile Preparation of Raspberry-Like Superhydrophobic Polystyrene Particles via Seeded Dispersion Polymerization. *Langmuir* **2013**, *29*, 11440-11448.
138. Wang, F.; Yu, S.; Ou, J.; Xue, M.; Li, W. Mechanically Durable Superhydrophobic Surfaces Prepared by Abrading. *J. Appl. Phys.* **2013**, *114*, 124902.
139. Kota, A. K.; Choi, W.; Tuteja, A. Superomniphobic Surfaces: Design and Durability. *MRS Bull.* **2013**, *38*, 383-390.
140. Jenner, E.; Barbier, C.; D'Urso, B. Durability of Hydrophobic Coatings for Superhydrophobic Aluminum Oxide. *Appl. Surf. Sci.* **2013**, *282*, 73-76.

141. Höhne, S.; Blank, C.; Mensch, A.; Thieme, M.; Frenzel, R.; Worch, H.; Müller, M.; Simon, F. Superhydrophobic Alumina Surfaces Based on Polymer-Stabilized Oxide Layers. *Macromol. Chem. Phys.* **2009**, *210*, 1263-1271.
142. Vargel, C. *Corrosion of Aluminium*. 2nd ed.; Elsevier Science: **2004**.
143. Pedferri, P. Cathodic Protection and Cathodic Prevention. *Constr. Build. Mater.* **1996**, *10*, 391-402.
144. Bouchama, L.; Azzouz, N.; Boukmouche, N.; Chopart, J. P.; Daltin, A. L.; Bouznit, Y. Enhancing Aluminum Corrosion Resistance by Two-Step Anodizing Process. *Surf. Coat. Technol.* **2013**, *235*, 676-684.
145. O'Brien, P.; Kortenkamp, A. The Chemistry Underlying Chromate Toxicity. *Transition Met. Chem.* **1995**, *20*, 636-642.
146. Damborenea, J. J. D.; Davó, B. Use of Rare Earth Salts as Electrochemical Corrosion Inhibitors for an Al–Li–Cu (8090) Alloy in 3.56 % NaCl. *Electrochim. Acta* **2004**, *49*, 4957-4965.
147. Kaneko, K.; Inoke, K.; Freitag, B.; Hungria, A. B.; Midgley, P. A.; Hansen, T. W.; Zhang, J.; Ohara, S.; Adschiri, T. Structural and Morphological Characterization of Cerium Oxide Nanocrystals Prepared by Hydrothermal Synthesis. *Nano Lett.* **2007**, *7*, 421-425.
148. Turekian, K. K.; Wedepohl, K. H. Distribution of the Elements in Some Major Units of the Earth's Crust. *Geol. Soc. Am. Bull.* **1961**, *72*, 175-192.
149. Su, F.; Yao, K. Facile Fabrication of Superhydrophobic Surface with Excellent Mechanical Abrasion and Corrosion Resistance on Copper Substrate by a Novel Method. *ACS Appl. Mater. Interfaces* **2014**, *6*, 8762-8770.
150. Oh, I.-k.; Kim, K.; Lee, Z.; Ko, K. Y.; Lee, C.-w.; Lee, S. J.; Myung, J. M.; Lansalot-matras, C.; Noh, W.; Dussarrat, C.; Kim, H.; Lee, H.-b.-r. Hydrophobicity of Rare Earth Oxides Grown by Atomic Layer Deposition. *Chem. Mater.* **2015**, *27*, 148-156.
151. Molinari, M.; Parker, S. C.; Sayle, D. C.; Islam, M. S. Water Adsorption and Its Effect on the Stability of Low Index Stoichiometric and Reduced Surfaces of Ceria. *J. Phys. Chem. C* **2012**, *116*, 7073-7082.
152. Fernández-Torre, D.; Kośmider, K.; Carrasco, J.; Ganduglia-Pirovano, M. V.; Pérez, R. Insight into the Adsorption of Water on the Clean CeO₂ (111) Surface with Van Der Waals and Hybrid Density Functionals. *J. Phys. Chem. C* **2012**, *116*, 13584-13593.
153. Carchini, G.; Garcia-Melchor, M.; Łodziana, Z.; López, N. Understanding and Tuning the Intrinsic Hydrophobicity of Rare- Earth Oxides: A DFT+U Study. *ACS Appl. Mater. Interfaces* **2016**, *8*, 152-160.
154. Ou, J.; Hu, W.; Xue, M.; Wang, F.; Li, W. Superhydrophobic Surfaces on Light Alloy Substrates Fabricated by a Versatile Process and Their Corrosion Protection. *ACS Appl. Mater. Interfaces* **2013**, *5*, 3101-3107.

155. Wang, Z.; Ye, W.; Luo, X.; Wang, Z. Heat-Resistant Crack-Free Superhydrophobic Polydivinylbenzene Colloidal Films. *Langmuir* **2016**, *32*, 3079-3084.
156. Tian, X.; Verho, T.; Ras, R. H. A. Moving Superhydrophobic Surfaces Toward Real-world Applications. *Science* **2016**, *352*, 142-143.
157. Tiseanu, C.; Parvulescu, V. I.; Boutonnet, M.; Cojocaru, B.; Primus, P. A.; Teodorescu, C. M.; Solans, C.; Sanchez Dominguez, M. Surface versus Volume Effects in Luminescent Ceria Nanocrystals Synthesized by an Oil-in-Water Microemulsion Method. *PCCP* **2011**, *13*, 17135-17145.
158. Li, L.; Zhang, Y.; Lei, J.; He, J.; Lv, R.; Li, N.; Pan, F. A Facile Approach to Fabricate Superhydrophobic Zn Surface and Its Effect on Corrosion Resistance. *Corros. Sci.* **2014**, *85*, 174-182.
159. Lin, K.-s.; Chowdhury, S. Synthesis , Characterization , and Application of 1-D Cerium Oxide Nanomaterials: A Review. *Int. J. Mol. Sci.* **2010**, *11*, 3226-3251.
160. Farahmandjou, M.; Zarinkamar, M. Synthesis of Nano-sized Ceria (CeO₂) Particles via a Cerium Hydroxycarbonate Precursor and the Effect of Reaction Temperature on Particle Morphology. *JUFGNSM* **2015**, *48*, 5-10.
161. Rui-Juan, Q.; Ying-Jie, Z.; Guo-Feng, C.; Yue-Hong, H. Sonochemical Synthesis of Single-Crystalline CeOHCO₃ Rods and Their Thermal Conversion to CeO₂ Rods. *Nanotechnology* **2005**, *16*, 2502.
162. Guo, Z.; Du, F.; Li, G.; Cui, Z. Synthesis and Characterization of Single-Crystal Ce(OH)CO₃ and CeO₂ Triangular Microplates. *Inorg. Chem.* **2006**, *45*, 4167-4169.
163. Lia, Q.; Hana, Z.; Shaoa, M.; Liub, X.; Qiana, Y. Preparation of Cerium Hydroxycarbonate by a Surfactant-Assisted Route. *J. Phys. Chem. Solids* **2003**, *64*, 295-297.
164. Wang, H.-C.; Lu, C.-H. Synthesis of Cerium Hydroxycarbonate Powders via a Hydrothermal Technique. *Mater. Res. Bull.* **2002**, *37*, 783-792.
165. Chan, S. G. K. a. K. L. A. ATR-FTIR Spectroscopic Imaging: Recent Advances and Applications to Biological Systems. *RSC Adv.* **2013**, *138*, 1940-1951.
166. Babitha, K. K.; Sreedevi, A.; Priyanka, K. P.; Sabu, B.; Varghese, T. Structural Characterization and Optical Studies of CeO₂ Nanoparticles Synthesized by Chemical Precipitation. *IJPAP* **2015**, *53*, 596-603.
167. Paz, Y.; Trakhtenberg, S.; Naaman, R. Reaction between O(3P) and Organized Organic Thin Films. *J. Phys. Chem.* **1994**, *98*, 13517-13523.
168. Lee, C. Y.; Le, Q. V.; Kim, C.; Kim, S. Y. Use of Silane-Functionalized Graphene Oxide in Organic Photovoltaic Cells and Organic Light-Emitting Diodes. *PCCP* **2015**, *17*, 9369-9374.

169. Burroughs, P.; Hamnett, A.; Orchard, A. F.; Thornton, G. Satellite Structure in the X-ray Photoelectron Spectra of some Binary and Mixed Oxides of Lanthanum and Cerium. *J. Chem. Soc., Dalton Trans.* **1976**, 17, 1686-1698.
170. Paparazzo, E. On the Curve-Fitting of XPS Ce(3d) Spectra of Cerium Oxides. *Mater. Res. Bull.* **2011**, 46, 323-326.
171. Moulder, J. F.; Stickle, W. F.; Sobol, P. E.; Bomben, K. D. *Handbook of X-ray Photoelectron Spectroscopy*. Physical Electronics: **1995**; p 261.
172. Tan, Y.; Zhang, S.; Liang, K. Photocurrent Response and Semiconductor Characteristics of Ce-Ce₂O₃-CeO₂-Modified TiO₂ Nanotube Arrays. *Nanoscale Res. Lett.* **2014**, 9, 67-73.
173. Flege, J. I.; Kaemena, B.; Höcker, J.; Bertram, F.; Wollschläger, J.; Schmidt, T.; Falta, J. Ultrathin, Epitaxial Cerium Dioxide on Silicon. *Appl. Phys. Lett.* **2014**, 104, 131604.
174. Nakayama, Y.; Takahagi, T.; Soeda, F.; Ishitani, A. XPS Study of Oriented Organic Molecules. *J. Colloid Interface Sci.* **1989**, 131, 153-160.
175. Alam, A. U.; Howlader, M. M. R.; Deen, M. J. Oxygen Plasma and Humidity Dependent Surface Analysis of Silicon, Silicon Dioxide and Glass for Direct Wafer Bonding. *ECS J. Solid State Sci. Technol.* **2013**, 2, 515-523.
176. Khung, Y. L.; Ngalim, S. H.; Scaccabarozi, A.; Narducci, D. Formation of Stable Si-O-C Submonolayers on Hydrogen-Terminated Silicon (111) under Low-Temperature Conditions. *Beilstein J. Nanotechnol.* **2015**, 6, 19-26.